The Dependence of Radio-Mode Feedback on Baryonic and Halo Mass

by

Robert Main

A thesis
presented to the University of Waterloo
in fulfillment of the
thesis requirement for the degree of
Master of Science
in
Physics

Waterloo, Ontario, Canada, 2014

Author's Declaration

I hereby declare that I am the sole author of this thesis. This is a true copy of the thesis, including any required final revisions, as accepted by my examiners.

I understand that my thesis may be made electronically available to the public.

Abstract

Supermassive black holes launch powerful radio-synchrotron jets into the hot atmospheres of galaxy clusters, creating bubbles of displaced gas and driving shock fronts. These jets output a tremendous amount of energy, preventing rapid cooling of the X-ray atmospheres, and suppressing star formation in massive galaxies. In this thesis I investigate the link between feedback from active galactic nuclei (AGN) and the large-scale properties of galaxy clusters.

I begin by analysing the cluster scaling relations in systems experiencing radio-mode feedback. The sample comprises of 50 systems with X-ray cavities, including the 23 systems from the HIghest FLUx Galaxy Cluster Sample (HIFLUGCS) with X-ray cavities and central cooing times less than 1 Gyr. Using archival Chandra data, I derive mass profiles of both the total mass and gas mass for each cluster. I then determine the bolometric luminosity, temperature, halo mass, and gas mass within a self-similar radius. K-band magnitudes from the Two Micron All-Sky Survey (2MASS) are used to calculate the stellar mass of the brightest cluster galaxy (BCG). I fit the relationships between mass, temperature, and luminosity in our sample, compare them to the theoretical self-similar scalings, and to previous studies using the full cluster population. I also investigate the relationships between the mass in stars, gas, and dark matter. I attempt to answer if AGN feedback is responsible for the decrease in integrated star formation efficiency with mass, and if it is able to displace the missing gas in clusters.

I then investigate how mechanical AGN power scales with cluster properties. I find a strong correlation between AGN power and halo mass, and find the relationship between AGN power and cluster luminosity is consistent with linear. I compare the relationship between AGN power and halo mass to an analytic model used in simulations, and I measure the accretion rate of AGN outbursts across our sample in an attempt to explain the differences between them. I address possible biases in the measured relationship between AGN power and halo mass, including spurious correlations caused by redshift, and bias caused by degeneracy between measurements of halo mass and AGN power. I look at the spread of cavity angular sizes with redshift, finding no redshift-dependent bias on measuring AGN power from X-ray cavities. I use radio luminosity as a proxy for AGN power that is not degenerate with halo mass, and again find that the mechanical power of AGN correlates strongly with cluster mass.

Finally, I look at the effect of AGN heating in the full HIFLUGCS sample, which contains 64 systems. The luminosity of central radio sources is used as a proxy for mechanical AGN power, and the systems are sorted by the central cooling time of the intracluster

medium (ICM). A clear separation is found in the relationship between AGN power and mass based on central cooling time, and I discuss this in the context of a feedback cycle. I find no separation in the relationship between halo mass and BCG stellar mass with central cooling time, indicating that cooling flows are balanced over long timescales. I calculate the energy per particle injected from individual AGN outbursts and discuss in context of the energy required to break self-similarity in clusters and groups.

Acknowledgements

I owe a great deal of gratitude to my supervisor Prof. Brian McNamara for giving me this opportunity, and providing considerable advice and guidance over the course of this project. I also owe a large amount of thanks to Helen Russell for amazing patience in helping me develop my sea legs (space legs?), providing scripts I adapted to this project, and for a large amount general help and guidance along the way. I would like to thank Paul Nulsen for helpful input on my draft, and for providing the code used in a large amount of this analysis. Thanks also to Adrian Vantyghem, who was the sounding board for my ideas. Finally, I would like to thank Hillary Roulston, my family, and my friends for all of their support.

Table of Contents

List of Tables

List of Figures

Chapter 1

Introduction

1.1 Introduction to Galaxy Clusters

The study of galaxy clusters began in the late 1700s, when Messier and Herschel discovered the tendency of "nebulae" to appear concentrated on the sky. These nebulae were not conclusively determined to be extragalactic sources until the 1920s, when Edwin Hubble used observations of cepheid variable stars to show that they were too distant to be within the Milky Way (Hubble, 1926). This discovery meant that nebulae were individual galaxies, and made way for the study of galaxies as physical systems.

The first estimates of galaxy cluster masses were first made in the 1930s in the Coma and Virgo clusters, using the virial theorem with measurements of the velocities of cluster galaxies (Zwicky, 1933, 1937; Smith, 1936). The inferred masses were found to be much larger than the mass of all of the stars, providing the first evidence for dark matter. A large component of this missing matter was discovered to be in the form of hot, low-density plasma spread smoothly throughout the full volume a galaxy cluster, seen as extended X-ray emission (Giacconi et al., 1972; Gursky & Schwartz, 1977). This hot atmosphere is referred to as the intracluster medium (ICM), and typically has temperatures in the range of $10^7 - 10^8$ Kelvin, and X-rays luminosities in the range of $L_x \sim 10^{43} - 10^{45}$ erg s^{-1} (Sarazin, 1988).

Galaxy clusters are comprised of hundreds to thousands of galaxies, spanning $\sim 1 - 3$ Mpc. X-ray emission in galaxy clusters is seen as extended emission not localised to the locations of galaxies, and is often peaked near a central giant elliptical galaxy referred to as the brightest cluster galaxy (BCG). These galaxies typically lie near the minimum of

the cluster potential, and are close to the systemic velocity of the galaxy cluster. BCGs have stellar masses upwards of $10^{12} M_{\odot}$, and dominate the central dynamics.

Measurements of the ICM allowed for an independent measure of the gravitational mass of galaxy clusters, and reinforced the need for a dark component of mass (Bahcall & Sarazin, 1977; Fabricant, Lecar & Gorenstein, 1980). Only $\sim 20\%$ of the mass in galaxy clusters is found to be in the form of baryons, split between the ICM ($\sim 90\%$) and stars ($\sim 10\%$) (eg: Lin, Mohr & Stanford 2003). The remaining $\sim 80\%$ of the mass is in the form of dark matter, the composition of which is unknown. Galaxy clusters range in mass from 10^{14} $M_{\odot}$ to several 10^{15} $M_{\odot}$, and are the most massive gravitationally bound systems in the Universe. The massive gravitational potential of galaxy clusters means that they are essentially "closed box" systems, retaining all of the matter they accrete. Beyond the inner regions of clusters, the hot atmospheres have cooling timescales longer than the Hubble time. As such, the ICM contains the full thermal history of the galaxy cluster, including the effects of heating from AGN and stellar evolution.

1.2 Intracluster Medium

1.2.1 Thermal Bremsstrahlung

In the 1970s, iron line emission was detected in the X-ray spectra of the Perseus, Coma, and Virgo galaxy clusters (Mitchell et al., 1976; Serlemitsos et al., 1977). This discovery revealed thermal bremsstrahlung as the main emission mechanism for X-rays in galaxy clusters. At temperatures lower than $T \sim 3 \times 10^7$ K, the luminosity from line emission is significant as well (Peterson & Fabian, 2006).

The luminosity of bremsstrahlung as a function of frequency ν per unit volume is given as:

$$\epsilon_{\nu}^{ff} = \frac{dW}{dV dt d\nu} = \frac{2^5 \pi e^6}{3 m_e c^3} \left(\frac{2\pi}{3 m_e k} \right)^{1/2} Z^2 n_e n_i g_{ff}(Z, T_g, \nu) T^{-1/2} \exp(-h\nu/kT), \tag{1.1}$$

where m_e is the electron mass, n_e ans n_i are the electron and ion density, and Z is the charge of the ion (Rybicki & Lightman, 2008). $g_{ff}(Z, T_g, \nu)$ is the Gaunt factor which corrects for quantum mechanical effects, is close to unity and has a weak frequency dependence. Integrating the emissivity over frequency, the total luminosity per unit volume is:

$$\frac{dP}{dV} \approx 10^{-27} T^{1/2} n_e n_H \tag{1.2}$$

Knowing the functional form of the emission, X-ray spectra can be used to determine the temperature, density, and metallicity of the ICM. The temperature of the ICM can be determined from the exponential cutoff of the X-ray spectrum at high energies. For a fixed temperature, the density of the gas is determined simply by the normalization of the spectrum, given by the emission measure:

$$EM = \int n_e n_i dV. \tag{1.3}$$

The metallicity is primarily constrained by the intensity of the Fe-K line complex at $\sim$ 6.7keV, and the Fe-L complex at $\sim 1 - 2$keV.

1.2.2 Hydrostatic Atmospheres - Mass Determinations

As clusters of galaxies form hierarchically, the baryonic atmospheres are heated by gravitational infall. The ICM forms a hydrostatic atmosphere, where the density and temperature distributions are governed by the underlying gravitational potential. The equation of hydrostatic equilibrium is:

$$\frac{1}{\rho_g}\nabla p = \nabla\phi, \tag{1.4}$$

where ρ_g is the gas density, ϕ is the gravitational potential, and p is the pressure of the ICM. Under the assumption of spherical symmetry, the enclosed mass as a function of radius is described as

$$M(r) = \frac{-kTr}{G\mu m_H}\left(\frac{d\,\log\,n_e}{d\,\log\,r} + \frac{d\,\log\,T}{d\,\log\,r}\right), \tag{1.5}$$

where $\mu \approx 0.6$ is the mean molecular weight of the particles in the ICM, and m_H is the mass of hydrogen (Sarazin, 1988). Thus, mass profiles of galaxy clusters can be determined in principle by measuring the radial profiles of temperature and density. Deviations from hydrostatic equilibrium result is mass estimates in relaxed clusters that are $\sim 10 - 20\%$ low at typically measured radii (R_{2500}, R_{500}) (Nagai, Kravtsov & Vikhlinin, 2007; Mahdavi et al., 2013). Masses are difficult to measure accurately in cluster outskirts, as the effects of non-thermal pressure and gas clumping (Simionescu et al., 2011) are likely significant.

In practice, X-ray spectra are extracted from discrete radial bins used to measure the temperature and density. The main limitation is the need for sufficient X-ray counts to measure the temperature precisely (Vikhlinin et al., 2005). Density profiles can be reconstructed by the surface brightness profile of the cluster, and are limited by the spatial

resolution of the instrument. Temperatures and densities are measured in cylindrical shells on the sky, and need to be "deprojected" to determine the true radial profiles (Kriss, Cioffi & Canizares, 1983; Russell, Sanders & Fabian, 2008). Deprojection introduces systematic errors in the measured profiles, often producing temperature profiles oscillating around the mean value (eg: Fabian et al. 2006). Additional constraints are often used to derive physical results for mass profiles, either by modelling the temperature and density profiles (Vikhlinin et al., 2006; Reiprich & Böhringer, 2002), or modelling the gravitational potential (Mahdavi et al., 2008). A model independent approach can be applied, but requires high-quality data covering well beyond the region of interest to produce reliable results (Nulsen, Powell & Vikhlinin, 2010).

1.3 Scaling Relations

If the formation of galaxy clusters is governed entirely by gravity, galaxy clusters would be self-similar (Kaiser, 1986). This leads to specific relations between the mass, temperature, and luminosity of galaxy clusters within a scaled radius. The mean density within a scaled radius is constant, such that:

$$M_\Delta / R_\Delta^3 = \text{constant}, \tag{1.6}$$

where R_Δ is the radius where the enclosed density is Δ times the critical density of the Universe. The emission is dominated by thermal bremsstrahlung, such that the luminosity within a radius R is:

$$L \propto \rho_g^2 T^{1/2} R_\Delta^3. \tag{1.7}$$

Hydrostatic equilibrium along with the virial theorem implies that $T \propto M/R$. Additionally, if the effects of gravity and shock heating are included, then the gas component should also be self-similar (Navarro, Frenk & White, 1995), implying $M \propto M_g$. Combining these equations gives expected scalings of cluster properties as:

$$L \propto T^2, M \propto T^{\frac{3}{2}}. \tag{1.8}$$

Observations find a relation between luminosity and temperature of $L \propto T^3$, much steeper than the self-similar predictions (eg: Markevitch 1998; Mahdavi et al. 2013). This suggests that non-gravitational processes have a significant effect in clusters. Radiative cooling in the cores of clusters is in part responsible for the steepening of the $L - T$ relation, as it shows less scatter and is closer to self-similar expectation when the cores of clusters are excised (Markevitch, 1998; Maughan et al., 2008). However, core-excised $L-T$ relations are still typically steeper than the self-similar expectation, with the effect most

prominent in poor clusters and groups. The observed steepening of the $L-T$ relation is most commonly attributed to "pre-heating", which is the injection of additional entropy into cluster gas before virialization (Kaiser, 1991; Evrard & Henry, 1991).

The $M-T$ relation is usually found to be close to the self-similar expectation of $M \propto T^{\frac{3}{2}}$ in clusters (Vikhlinin et al., 2006), while the relation steepens to $M \propto T^{1.6-1.7}$ when galaxy groups are included (Arnaud, Pointecouteau & Pratt, 2005; Sun et al., 2009). Additionally, the $M-T$ relation shows scatter of $\approx 15\%$, considerably lower than the scatter in the $L-T$ relation. The temperature is determined almost entirely by the depth of the potential well, and is fairly insensitive to the effects of heating and cooling.

1.4 Mass Partitioning

As the X-ray luminosity is proportional to the gas density squared, the steepening of the $L-T$ relation is strongly linked to the gas content in galaxy clusters (Pratt et al., 2009). The gas fraction in galaxy clusters, defined as $f_g = M_g/M_{\rm tot}$, increases with increasing halo mass (Lin, Mohr & Stanford, 2003; Vikhlinin et al., 2006; Gonzalez et al., 2013). Additionally, the ICM is less centrally peaked than the total mass distribution in clusters. This results in gas fraction profiles that increase with radius, moving closer to the cosmic baryon fraction at large radii (Vikhlinin et al., 2006; Sun et al., 2009).

Star formation is inefficient in galaxy clusters, as the majority of baryonic mass is contained in the ICM. The integrated star formation efficiency is highest in halo masses $\sim 10^{12} M_{\odot}$, and decreases strongly with increasing halo mass (Behroozi, Wechsler & Conroy, 2013; Gonzalez et al., 2013). This trend is dominated by central galaxies, and the integrated star formation efficiency of satellites appears to be roughly constant with halo mass (Kravtsov, Vikhlinin & Meshscheryakov, 2014). There must then be a mechanism which preferentially suppresses star formation in central galaxies, which is somehow related to the total halo mass. Several proposed mechanisms include quenching of star formation due to the shock heating of the ICM (Dekel & Birnboim, 2006), heating from AGN (McNamara & Nulsen, 2007), and heating from AGB stars (Conroy, van Dokkum & Kravtsov, 2014).

1.5 Cooling Flows

The density of hot gas in galaxy clusters is often sharply centrally peaked. The X-ray luminosity scales as density squared, leading to a large loss of energy of the ICM in X-rays.

The timescale to radiate away the thermal energy of the ICM can drop well below the age of the cluster. This should create a "cooling flow", where gas slowly flows inwards to maintain the central pressure as energy is radiated away (see Fabian 1994 for a review). In the absence of heating, a cooling-flow would provide a steady flow of cool gas onto the central galaxy, fueling star formation and resulting in vast amounts of molecular gas.

This simple cooling flow model disagrees with observations, in what is known as the "cooling flow problem". Star formation is seen at the centres of cooling flows, but not at the rate of $100-1000 M_{\odot}$/yr implied by the cooling flow model, and sub-millimeter observations find significantly lower quantities of molecular gas than expected (Edge, 2001; Salomé & Combes, 2003). Additionally, X-ray spectroscopy of cooling flows find no evidence of emission lines that would indicate gas cooling below $\sim 1/3$ of the virial temperature (Peterson & Fabian, 2006). These observations form convincing evidence that cooling flows are being suppressed. The effects of thermal conduction can offset cooling, but not to the extent needed to match observations (Voigt & Fabian, 2004). Additionally, suppression of cooling flows by thermal conduction is unstable, as it needs careful fine-tuning of parameters to balance radiative losses. The leading mechanism for suppressing cooling flows is feedback from active galactic nuclei (AGN), which will be discussed in the next section.

1.6 AGN Feedback

Outbursts from active galactic nuclei have been found to have a significant effect on the hot atmospheres of galaxy clusters, galaxy groups, and giant elliptical galaxies (see McNamara & Nulsen 2007, 2012; Fabian 2012 for reviews). Radio jets from central super-massive black holes (SMBHs) deposit large amounts of energy mechanically into their host galaxies over tens to thousands of kpc by inflating bubbles (eg: Bîrzan et al. 2004; Dunn, Fabian & Taylor 2005; Allen et al. 2006; Dong, Rasmussen & Mulchaey 2010; Cavagnolo et al. 2010; O'Sullivan et al. 2011) and driving shocks into the ICM (eg: Nulsen et al. 2005; Forman et al. 2007; Blanton et al. 2011; Randall et al. 2011). These bubbles, or cavities, are detected as surface brightness depressions in high resolution X-ray images, and give a direct measure of the energy output of the AGN outburst.

Time intervals of radio-AGN feedback are tied to the central cooling time of the ICM (Rafferty, McNamara & Nulsen, 2008), implying that AGN outbursts operate in a feedback cycle. Multiple generations of outbursts have been observed in over a dozen deeply exposed systems, showing an on-off cycle which is typically shorter than the central cooling time (Vantyghem et al., 2014). The mechanical energy output of AGN scales roughly linearly

with the luminosity of the cooling region, and is sufficient on average to offset radiative losses of the ICM (Rafferty et al., 2006; Nulsen et al., 2009; Hlavacek-Larrondo et al., 2012)

Previous studies in complete samples have found cavities in $\sim 60-70\%$ of cool-core systems (Dunn & Fabian, 2006; Bîrzan et al., 2012). The true fraction is likely higher, as bubbles can be missed in existing images due to shallow data or jet orientation along our line of sight (Bîrzan et al., 2012). Shock fronts are more difficult to detect in X-ray images, but they are usually seen in systems with deeply exposed images. This suggests that AGN feedback is prevalent in cooling flow systems. Cool cores have been observed as early as $z \sim 1$ (McDonald et al., 2013), which suggests that radio-mode feedback has been operating in clusters for the majority of the lifetime of the universe. Radio AGN have also been found to drive outflows of both the hot ICM (Simionescu et al., 2008; Kirkpatrick, McNamara & Cavagnolo, 2011) and cold molecular gas out of central galaxies (Russell et al., 2014; McNamara et al., 2014), enriching cluster atmospheres and removing a substantial fraction of the gas which could form stars in BCGs.

The effects of mechanical feedback appear to be crucial in shaping the properties in cluster cores, but the extent to which it can affect the global scale properties of host systems is poorly understood. Mittal et al. (2009) found that the central radio luminosity correlates with the bolometric X-ray luminosity in strong cool-core clusters, demonstrating that centrally located AGN are correlated to global large scale properties of the ICM. AGN feedback is now generally included in cosmological simulations of galaxy formation to account for the observed cut-off at high luminosities in the galaxy luminosity function (Croton et al., 2006; Bower et al., 2006). It is then possible that the effects of AGN heating are suppressing star formation in BCGs, and shaping the relationship between stellar mass fraction and halo mass above $M \sim 10^{12} M_{\odot}$. This trend is dominated by central galaxies (Kravtsov, Vikhlinin & Meshscheryakov, 2014), and radio-AGN preferentially occur in BCGs (Best et al., 2007), making it a promising mechanism to reproduce the relationship. Simulations have also found that it is possible to reproduce observed scaling relations with AGN feedback (McCarthy et al., 2010; Short et al., 2010), but it may be difficult to break self-similarity without breaking the cool-core structure in galaxy clusters (Gaspari et al., 2014).

1.7 Objectives of this Thesis

In this thesis, we investigate the role of radio-mode feedback in shaping cluster properties. We aim to determine how AGN feedback scales with cluster properties, and determine the best indicator of AGN power. We also aim to answer if AGN activity is responsible for

the breaking of self-similarity in galaxy clusters, or if it causing the decrease in integrated star formation efficiency in large halos. As AGN activity is sometimes observed in systems without strong cooling flows, we aim to investigate the difference in how AGN heating operates in systems with and without strong ICM cooling.

To do this, we analyse the systems in the HIghest FLUx Galaxy Cluster Sample (HIFLUGCS) (Reiprich & Böhringer, 2002), a complete flux-limited sample of clusters. From archival Chandra data, we derive total mass and gas mass profiles in 45 systems with X-ray cavities, and we measure stellar masses of our BCGs using K-band magnitudes from the Two Micron All-Sky Survey[1] (2MASS, Skrutskie et al. 2006). We measure the scaling relations in systems experiencing feedback, and compare them to the scaling relations of the global cluster population. We aim to answer if the integrated effects of AGN heating are energetically sufficient to shape the observed scaling relations. We measure the relationships and scatter between mechanical AGN power and large-scale cluster properties. Finally, we investigate how AGN power and star formation efficiency scale with mass when separated into systems with long and short cooling timescales of the ICM.

In Appendix B, we describe some of the science that will be done with the upcoming Astro-H satellite. We detail planned observing strategies, and spectral simulations of the Virgo cluster that we contributed to the early science phase of the mission. In this thesis, we assume a cosmology with $\Omega_M = 0.3$, $\Omega_\Lambda = 0.7$, $\mathrm{H}_o = 70$ km s^{-1} Mpc^{-1}. All errors are quoted at the 1σ level, unless stated otherwise.

[1] http://www.ipac.caltech.edu/2mass/

Chapter 2

Sample and Data Reduction

2.1 Sample

We aim to investigate the effects of radio-mode feedback in the HIghest FLUx Galaxy Cluster Sample (HIFLUGCS), a complete flux limited X-ray sample of 64 systems at galactic latitude $|b| > 20^o$ with X-ray flux $f_x > 2.0 \times 10^{-11}$ erg s^{-1} cm^{-2} in the 0.1-2.4keV band (Reiprich & Böhringer, 2002). All of the clusters in HIFLUGCS have been observed with Chandra, and 26 of these systems have observed X-ray cavities (Bîrzan et al. 2012). Additionally, all 64 clusters in HIFLUGCS have detections or upper limits of 1.4 GHz radio emission of central radio sources. We use the 23 X-ray cavity systems with central cooling times $t_c < 1$ Gyr to investigate the scaling relations of AGN mechanical power with cluster properties, since the AGN power in these systems is correlated to the cluster-scale properties of the ICM (Mittal et al. 2009, section 4.6). We refer to this subset as our primary sample throughout. We use the 1.4 GHz emission to investigate AGN heating in the full HIFLUGCS sample in section 4.6. Values used for the HIFLUGCS systems not in our primary sample are taken from the literature, and are referenced throughout.

For some parts of this analysis, we include an additional 27 cavity systems where we were able to determine hydrostatic masses to extend the dynamic range of our sample. We refer to this as the extended sample throughout. This extended sample includes the systems in Rafferty et al. (2006) which are not in HIFLUGCS, and the clusters from the Massive Cluster Survey (MACS, Ebeling, Edge & Henry 2001) with clear cavities from Hlavacek-Larrondo et al. (2012). We additionally include the giant elliptical galaxies NGC5813 and NGC5846. Table 2.2 lists our sample and cleaned Chandra exposure times of all observations used.

2.2 Data Reduction

All observations were reprocessed with CIAO 4.6 using CALDB 4.5.9. Events were corrected for the time-dependent gain and charge transfer inefficiency and then filtered to remove those with bad grades. The improved background screening it enables was applied to all observations taken in VFAINT mode. Background light curves were extracted from the level 2 event files, and were filtered for flares using the LC_CLEAN[1] routine of M. Markevitch. Blank-sky backgrounds were extracted for each observation, processed identically to the events files, and reprojected to the sky position of the corresponding events files. The blank-sky backgrounds were normalized to match the 9.5-12.0 keV flux in the data set. All observations used, and final cleaned exposure times are detailed in Table 2.2.

[1] http://cxc.cfa.harvard.edu/contrib/maxim/acisbg/

Table 2.1: Target list and properties of our systems

System	z	Exposure[a] (ks)	N_H[b] (10^{22}cm^{-2})	m_K	M_K	r_e[c] (kpc)	BCG Stellar Mass (10^{11} $M_\odot$)	M_{BH} (10^9 $M_\odot$)
2A0335+096	0.035	82.3	0.224	9.81±0.05	-26.18±0.05	44.3	5.07 ± 0.24	$1.2^{+2.7}_{-0.7}$
A85	0.055	37.4	0.039*	10.09±0.04	-26.72±0.04	50.8	6.92 ± 0.28	$2.0^{+4.2}_{-1.1}$
A133	0.057	109.4	0.0153	10.51±0.06	-26.35±0.06	28.9	6.34 ± 0.33	$1.4^{+3.1}_{-0.8}$
A262	0.016	108.6	0.089*	8.75±0.03	-25.66±0.03	28.9	2.61 ± 0.06	$0.8^{+1.7}_{-0.4}$
A478	0.088	135.2	0.281*	11.31±0.07	-26.68±0.07	67.8	8.07 ± 0.48	$1.9^{+4.1}_{-1.0}$
A496	0.033	52.4	0.04	9.81±0.02	-26.26±0.04	41.9	4.55 ± 0.17	$1.3^{+2.9}_{-0.7}$
A1795	0.063	391.5	0.041*	10.60±0.08	-26.47±0.08	69.7	5.32 ± 0.40	$1.6^{+3.4}_{-0.9}$
A2029	0.077	74.7	0.033	10.11±0.05	-27.42±0.05	72.2	13.2 ± 0.6	$3.6^{+7.7}_{-1.9}$
A2052	0.036	486.8	0.027	9.55±0.06	-26.33±0.06	51.2	4.85 ± 0.25	$1.4^{+3.0}_{-0.8}$
A2199	0.030	119.6	0.039*	9.17±0.03	-26.36±0.03	38.9	5.83 ± 0.18	$1.5^{+3.1}_{-0.8}$
A2204	0.152	69.7	0.061	12.24±0.19	-26.73±0.19	81.8	8.4 ± 1.4	$2.0^{+4.3}_{-1.1}$
A2597	0.085	108.5	0.0246	9.66±0.04	-25.63±0.04	40.6	3.08 ± 0.30	$0.8^{+1.7}_{-0.4}$
A4059	0.048	84.9	0.012	9.82±0.05	-26.67±0.05	58.4	8.03 ± 0.38	$1.9^{+4.1}_{-1.0}$
Centaurus	0.011	179.2	0.0854	7.14±0.02	-26.33±0.02	36.0	4.84 ± 0.11	$1.4^{+3.0}_{-0.8}$
Hydra A	0.055	152.6	0.0425	10.90±0.06	-25.91±0.06	33.8	3.43 ± 0.20	$1.0^{+2.1}_{-0.5}$
MKW3S	0.045	48.3	0.0286	10.85±0.06	-25.54±0.06	32.8	2.91 ± 0.16	$0.7^{+1.5}_{-0.4}$
NGC507	0.017	37.8	0.06	8.30±0.02	-25.94±0.02	28.4	3.92 ± 0.08	$1.0^{+2.2}_{-0.5}$
NGC1399	0.0048	145.2	0.0138	6.31±0.03	-25.26±0.03	22.0	2.21 ± 0.06	$0.6^{+1.2}_{-0.3}$
NGC1550	0.012	89.0	0.12*	8.77±0.03	-24.89±0.03	15.6	1.55 ± 0.04	$0.4^{+0.9}_{-0.2}$
NGC4636	0.0031	133.4	0.0185	6.42±0.04	-24.20±0.04	20.8	0.80 ± 0.03	$0.4^{+0.8}_{-0.2}$
NGC5044	0.0093	82.5	0.051	7.71±0.02	-25.31±0.02	16.3	2.25 ± 0.04	$0.6^{+1.2}_{-0.3}$
PKS1404-267	0.022	83.5	0.0431	9.57±0.03	-25.28±0.03	22.8	1.84 ± 0.06	$0.6^{+1.2}_{-0.3}$
Sersic159/03	0.058	90.3	0.039*	10.59±0.10	-26.33±0.10	73.4	4.82 ± 0.43	$1.4^{+3.0}_{-0.8}$
3C388	0.0917	32.2	0.0562	11.67±0.06	-26.24±0.06	41.0	-	$1.3^{+2.8}_{-0.7}$
3C401	0.201	30.8	0.0535	-	-	-	-	-
4C55.16	0.241	64.5	0.0449	13.84±0.13	-26.09±0.13	45.7	-	$1.2^{+2.5}_{-0.6}$
A1835	0.253	177.0	0.02	12.67±0.14	-27.37±0.14	70.8	-	$3.4^{+7.4}_{-1.8}$
Cygnus A	0.056	182.1	0.28*	10.28±0.06	-26.70±0.06	52.4	-	$1.9^{+4.1}_{-1.0}$
HCG62	0.0137	115.5	0.0355	8.63±0.03	-25.36±0.03	24.5	-	$0.6^{+1.3}_{-0.3}$
Hercules A	0.154	95.0	0.06	12.55±0.11	-24.46±0.09	56.1	-	$1.6^{+3.4}_{-0.8}$
MACSJ0159.8-0849	0.405	64.4	0.020	-	-	-	-	-
MACSJ0242.5-0253	0.314	8.0	0.029	-	-	-	-	-
MACSJ0429.6-0253	0.399	19.3	0.043	-	-	-	-	-

MACSJ0547.0-3904	0.319	19.2	0.037	-	-	-	-	-
MACSJ0913.7+4056	0.442	69.3	0.016	-	-	-	-	-
MACSJ1411.3+5212	0.464	74.1	0.0138	-	-	-	-	-
MACSJ1423.8+2404	0.543	105.5	0.022	-	-	-	-	-
MACSJ1532.8+3021	0.345	84.5	0.0248	-	-	-	-	-
MACSJ1720.2+3536	0.391	53.7	0.036	-	-	-	-	-
MACSJ1931.8-2634	0.352	91.0	0.08	-	-	-	-	-
MACSJ2046.0-3430	0.423	44.1	0.047	-	-	-	-	-
MACSJ2140.2-2339	0.313	33.2	0.036	-	-	-	-	-
MS0735.6+7421	0.216	447.2	0.031	13.32±0.17	-26.37±0.17	59.1	-	$1.5^{+3.1}_{-0.8}$
NGC5813	0.0065	-	-	7.41±0.03	-24.83±0.03	21.8	-	$0.4^{+0.8}_{-0.2}$
NGC5846	0.0057	-	-	6.94±0.02	-25.02±0.02	14.5	-	$0.5^{+1.0}_{-0.2}$
Perseus	0.018	449.5	0.133	8.13±0.04	-26.33±0.04	49.4	-	$1.4^{+3.0}_{-0.8}$
PKS0745-191	0.103	116.0	0.415	11.49±0.09	-26.82±0.09	52.0	-	$2.2^{+4.6}_{-1.1}$
RBS797	0.354	38.3	0.0256	-	-	-	-	-
Zw2701	0.215	95.8	0.007	13.42±0.17	-26.25±0.17	36.0	-	$1.3^{+2.8}_{-0.7}$
Zw3146	0.291	34.0	0.0224	13.88±0.28	-26.46±0.28	65.5	-	$1.6^{+3.4}_{-0.8}$

The horizontal line before 3C388 separates the Primary and Extended samples. Notes: [a]Summed exposure times of all observations after flare cleaning. [b]N values marked with an * were found to be significantly different than the galactic value from Kalberla et al. (2005). [c]The extrapolation radius of the 2MASS K-band light profile.

Chapter 3

Analysis

3.1 X-ray Analysis

3.1.1 Mass Profiles: Spectral Extraction

Spectra were extracted from concentric circular annuli centred on the cluster centre. For systems with central surface brightness cusps, the centre was taken to be the position of the brightest pixel. For systems with no obvious central surface brightness peak, the cluster centre was taken to be the centroid of the X-ray emission. The inner regions of each cluster were excluded beyond the X-ray cavities. Point sources were detected using the WAVDETECT (Freeman et al., 2002) wavelet algorithm in CIAO, along with an image of the point spread function (PSF) to account for the degradation of the off-axis PSF. These point sources were confirmed by eye, and masked out of further analysis. Any known extended sources, or cluster substructure associated with mergers was masked out of further analysis as well. The masked regions typically accounted for only a few percent of the total area.

Annuli were created to have a minimum of ∼3000 counts, so that the temperature could be measured accurately in deprojection. Fewer source counts were required for low-temperature systems as emission lines make their temperature easier to determine. For systems with a very high number of source counts, we are limited by computational considerations rather than source counts. For these systems, the number of counts per annulus is chosen such that there are no more than ∼10-12 annuli per system. Spectra were extracted from these annuli in CIAO, and were grouped to have at least 30 counts per channel. Weighted redistribution matrix files (RMFs) were extracted using the *mkacisrmf*, and weighted auxiliary response files (ARFs) were created using *mkwarf*. Spectra for

observations on the same chip were summed together for observations of similar time period, and were kept separate otherwise. The ARFs and RMFs for the summed spectra were weighted according to the relative number of counts in each spectrum.

For each region, area is lost to masked point sources, chip gaps, etc. To calculate the fraction of area lost, normalized exposure maps were created for each observation, ignoring the effects of quantum efficiency and effective area. The exposure map was summed in each region, then divided by the area in pixels of the annulus used. This number will be the fraction of the area covered by each region compared to the ideal case. This number is added as the AREASCAL keyword to the spectra and background spectra. This is done to keep the relative normalization of the spectra accurate, since it plays a critical role in deprojection.

To check for residual soft background emission, spectra were extracted from regions without any cluster emission. These spectra were then compared with the blank-sky backgrounds for consistency. In the case that the soft background was inconsistent with the blank-sky background, the residual emission was modelled by one or two soft thermal models with $Z/Z_{\odot}$=1, z=0 as described in Vikhlinin et al. (2005). The normalization was allowed to be negative to account for an over-subtraction of the soft backgrounds. In systems where the cluster emission is non-negligible over the entire detector, the additional soft background component is fit simultaneously with the cluster emission in the outermost annulus. The model for the soft background emission was scaled by the area of each annulus and added as a CORRFILE to each spectrum. An example of a spectrum with and without the soft background correction is shown in Figure 3.1.

3.1.2 Mass Profiles: Hydrostatic Method

To calculate hydrostatic masses of these objects, spectra were analysed in XSPEC using the CLMASS mixing model (Described in detail in Nulsen, Powell & Vikhlinin 2010). This method assumes that the cluster is spherically symmetric, and that the X-ray emitting cluster gas is in hydrostatic equilibrium. The effects of non-thermal pressure at R_{2500} are estimated to bias mass measurements low on the order of $10\% - 20\%$ (Nagai, Kravtsov & Vikhlinin, 2007; Nelson, Lau & Nagai, 2014), but have also been found to be consistent with zero (Vikhlinin et al., 2009; Mahdavi et al., 2013). We use the additional assumption that the underlying gravitational potential follows the NFW profile (Navarro, Frenk & White, 1997)

$$\rho(r) = \frac{\rho_0}{r/r_s(1 + r/r_s)^2}, \tag{3.1}$$

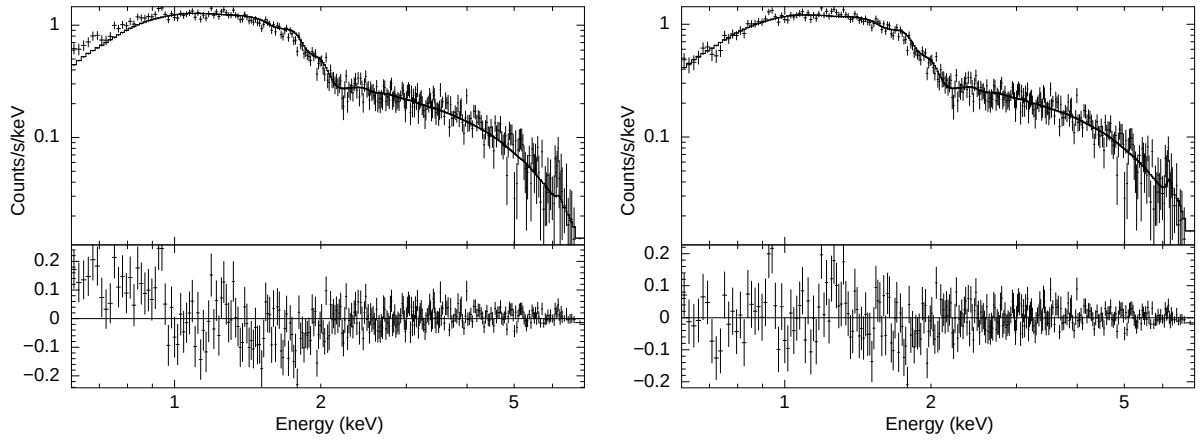

Figure 3.1: *Left:* Example spectrum and best fitting model from an outer region without the soft background correction applied, with best fit temperature of 6.2 keV. *Right:* The same spectrum after soft background correction, with best fit temperature of 7.9 keV. The top panel shows the data and model, and the bottom panel shows the residuals.

where ρ_0 is a characteristic density, and r_s is the scale radius. The NFW profile has been found to be an accurate description of cluster mass profiles, including systems with significant feedback (Pointecouteau, Arnaud & Pratt, 2005; Vikhlinin et al., 2006; Schmidt & Allen, 2007; Gitti et al., 2007). The full radial information of the temperature, gas density, and gravitating density are then given by r_s, $A = 4\pi G\rho_0 r_s^2$, and a temperature for each annulus. This has the advantage that the confidence ranges of r_s and A can be determined directly from the spectra.

In conjunction with the CLMASS model, each region was fit in the energy range 0.6-7.0 keV by a PHABS(APEC) model in XSPEC version 12.8.0 (Arnaud, 1996), using APEC version 2.0.2 (Foster et al., 2012). The spectra were fit using χ^2 minimization. The values of Anders & Grevesse (1989) were used for the solar abundances. The hydrogen column density (N_H) values were fixed to the galactic values of Kalberla et al. (2005), except in systems where the best fit value was found to be significantly different. The N_H values used are listed in Table 2.2. Abundances were generally left free in the spectral fits, but were tied between adjacent annuli if there were insufficient counts to be well determined. This was only needed in the outer regions of clusters, where there are not strong metallicity gradients (De Grandi & Molendi, 2001).

Galaxy cluster masses are typically measured out to a radius R_Δ, defined as the radius

in which the enclosed mass is Δ times the critical density at the cluster redshift. Then,

$$M_{\Delta} = \frac{4\pi R_{\Delta}^3}{3} \Delta \rho_c, \tag{3.2}$$

where $\rho_c = 3H^2/8\pi G$, $H = H_o E(z)$, and $E(z) = (\Omega_M(1+z)^3 + \Omega_\Lambda)^{1/2}$ in a flat Λ-CDM cosmology. We determine masses out to R_{2500}, as the Chandra data extend beyond it for the majority of our sample, and M_{2500} is then used as a proxy for cluster mass. The values of M_{2500} and R_{2500} are determined from the best fit NFW profile by numerically solving equation 3.2. In some nearby systems, extrapolation of the NFW profile was needed to reach R_{2500}. In these systems, the errors on M_{2500} are likely underestimated. All calculated values of M_{2500} are given in Table 3.4, and the systems where extrapolation to R_{2500} was needed are noted. The reduced χ^2 values of our spectral fits of our sample range from 0.89 to 1.32 with a mean value of 1.09. The Perseus cluster is an outlier with a reduced χ^2 value of 3.11. Perseus has exceptionally high quality data due both to being the brightest X-ray cluster in the sky and having deep exposures, and needs a multi-temperature model with multiple element abundances left free to adequately fit its spectra adequately (eg: (Sanders et al., 2004)). Our derived mass profiles are shown together with the gas mass profiles in Appendix A.

To test our method, we compare our mass measurements with other Chandra based hydrostatic measurements from the literature. We determine M_{2500} for the sample of clusters analysed in Vikhlinin et al. (2006), except for Abell 2390 which was unconstrained. We also compare our M_{2500} values to those of Allen et al. (2008) and Sun et al. (2009) in the systems that overlap with our sample. We convert the literature mass measurements to our cosmology, and show a comparison of our measurements in Figure 3.2. We find that our method results in consistent mass measurements within R_{2500}, and no apparent mass dependent bias on our measurements is observed.

3.1.3 Gas Mass

The gas density profiles were derived from the same set of spectra as our total masses, but with the central bin included. The spectra were fit in the 0.6-7.0 keV range with using a PROJCT(PHABS*APEC) model in XSPEC, to obtain deprojected gas density profiles. The density profiles were then integrated in a piecewise manner from the centre of the cluster to obtain the radial gas mass distribution. From the gas mass profile, we derived M_g and f_g within R_{2500} (shown in Table 3.4). In systems where the data do not reach R_{2500}, M_g was extrapolated to R_{2500}. The outer bin in deprojections often has artificially high emissivity,

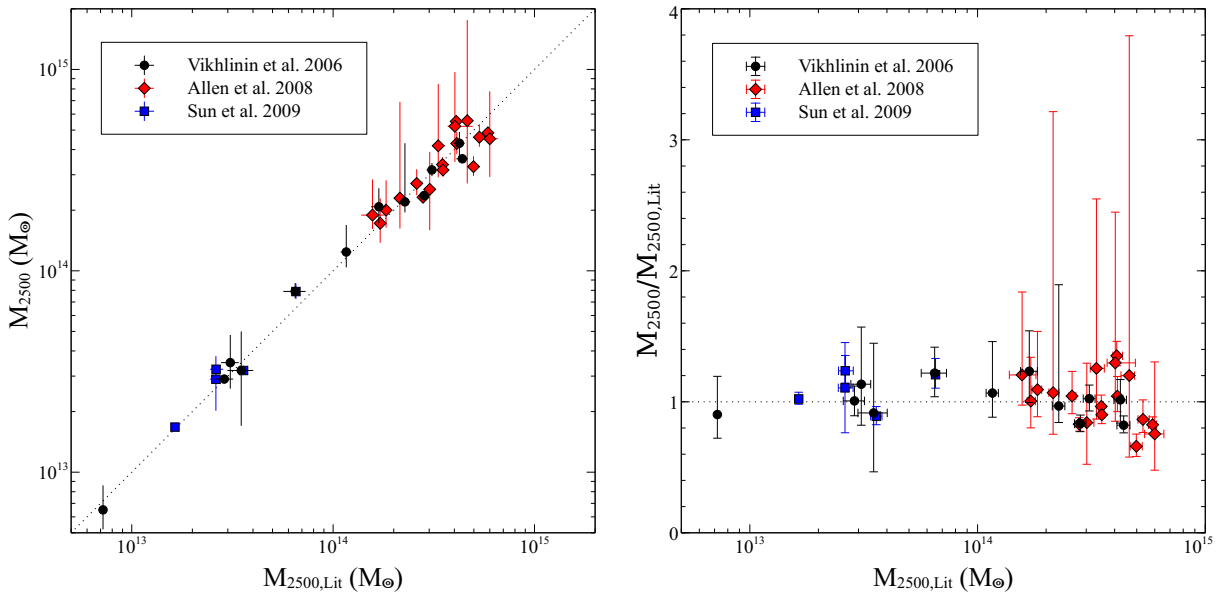

Figure 3.2: *Left:* M_{2500} from this work vs. M_{2500} values from the literature. *Right:* Ratio of M_{2500} values from this work by M_{2500} values from the literature vs. M_{2500} from the literature. The dotted lines show the line of equality.

since it relies on the assumption that there is no cluster emission beyond it (see the gas mass profiles in Appendix A). Due to this effect, we extrapolate our gas mass profiles from the second to last bin to determine M_g at R_{2500}.

3.1.4 Luminosity and Temperature

We calculated the X-ray luminosity and temperature of our sample both including and excluding the cluster cores. Spectra were extracted from apertures out to R_{2500} in each system, with the inner 0.3 R_{2500} excluded for the core-excised spectra. These spectra were fit with a PHABS(APEC) model in XSPEC, along with an additional APEC model for the excess soft background when needed. The CFLUX model in XSPEC was used to calculate the unabsorbed flux in the energy range of 0.05 keV - 50 keV.

3.2 Cavity Energetics

The mechanical energy output from the central AGN can be directly measured from cavities observed in X-ray data (McNamara et al., 2000; Churazov et al., 2001; Bîrzan et al., 2004). Using the assumption that the cavities are in pressure balance with the surrounding ICM, the total mechanical energy output from the AGN is given by the enthalpy of the cavity

$$E_{\rm cav} = \frac{\gamma}{\gamma - 1} pV, \tag{3.3}$$

where p is the pressure inside the cavity, V is the volume of the cavity, and γ is the adiabatic index of the medium filling the cavity. The usual assumption is that the cavities are filled with relativistic plasma, as they are created by radio synchrotron emitting jets. In this case, $\gamma = 4/3$, and the energy output is $E_{\rm cav} = 4pV$. The mean power output is then obtained by dividing the energy output by an estimate of the outburst age. In this study, the buoyancy timescale of the cavities is used in all power calculations (McNamara et al., 2000; Churazov et al., 2001), which is calculated as

$$t_{\rm buoy} \approx R/v_t \approx R\sqrt{SC/(2gV)}. \tag{3.4}$$

The velocity is obtained by equating the buoyancy force to the force of ram pressure on a bubble, where R is the distance from the AGN to the bubble centre, V is the volume of the bubble, S is the cross sectional area of the bubble, and C is the drag coefficient taken as $C = 0.75$. The gravitational acceleration is calculated under the assumption of an isothermal sphere as $g \approx 2\sigma^2/R$, where σ is the stellar velocity dispersion of the BCG. Cavity energies and power measurements for the systems in our sample were taken from the literature, and are listed along with the references used in Table 3.4.

The errors on the cavity powers come primarily from the uncertainties in the geometry and orientation of the cavities. Other effects can significantly alter the measurement of cavity power, including the poorly defined extent of cavities in underexposed images, the choice of location of the rims surrounding the cavities (McNamara & Nulsen 2012; Russell et al. 2013), and the effects of cluster "weather" (Mendygral, Jones & Dolag, 2012). As such, the errors on the cavity powers tend to be underestimated, which contributes to the large scatter in relations involving cavity power. As the errors are not well understood, we quote the total, not intrinsic scatter of our scaling relations involving cavity power. Additionally, AGN powers derived from X-ray cavities tend to underestimate the total power from the AGN (McNamara & Nulsen, 2007), and our results should be interpreted with this in mind.

3.3 Radio Luminosity

X-ray cavities are created by the interaction between a central radio source and the ICM. As such, we use the luminosity of central radio sources in our sample as an independent diagnostic of AGN activity. We obtain monochromatic 1.4 GHz radio luminosities of central radio sources for all of of the systems in HIFLUGCS, taken from either Mittal et al. (2009) or Bîrzan et al. (2012). In these studies, a radio source was deemed central if it is within $50h_{71}^{-1}$kpc of the X-ray peak. In systems without detected central radio sources, upper limits were derived by the noise in the NVSS images by Bîrzan et al. (2012).

3.4 Stellar and Black Hole Mass

We use K-band luminosities to trace the stellar mass in the BCGs of our sample, derived from the 2MASS Extended Source Catalog. We use the total apparent K-band magnitudes to calculate the stellar mass of our BCGs, derived from extrapolating the surface brightness profiles to the full radial extent of the galaxy. These magnitudes were corrected for galactic extinction using the values of Schlegel, Finkbeiner & Davis (1998). The evolutionary and K-corrections of Poggianti (1997) were applied as well. These were converted to absolute magnitudes using our adopted cosmology, and the redshift values given in Table 2.2. Corrected B−V colours were taken from HyperLeda[1] (Paturel et al., 2003), and K-band luminosities were converted to stellar masses using the relation of $\log(M/L_K) = -0.692 + 0.652(B-V)$ from Bell & de Jong (2001). For systems without B−V values in HyperLeda, we use the average B−V value of 0.86 ± 0.06 for our sample.

We use the K-band luminosities to estimate the black hole masses for our sample, using the relation between black hole mass and K-band luminosity of

$$\log\left(\frac{M_{\rm BH}}{M_\odot}\right) = -0.37(\pm0.04)(M_K + 24) + 8.29(\pm0.08) \tag{3.5}$$

from Graham (2007). This relation has a scatter of 0.33 dex, and we include this in the errors of our black hole masses.

Lauer et al. (2007) show that the K-band magnitudes for BCGs from 2MASS are likely underestimated, as they do not capture the full extent of the BCG envelope. Our calculated stellar masses and black hole masses are then likely to be underestimated. As

[1] http://leda.univ-lyon1.fr/

such, we additionally use the stellar mass within 20 kpc of our BCGs determined from the 2MASS circular apertures. These values should be less susceptible to biases from the shallow 2MASS images. We treat our black hole masses as estimates, and we discuss the potential biases in section 4.5.2.

Table 3.1: System properties derived from Chandra X-ray Data

System	P_{cav} [a] (10^{42} erg s^{-1})	pV (10^{58}erg)	M_{2500} [b] ($10^{13}M_{\odot}$)	Mg_{2500} ($10^{13}M_{\odot}$)	$f_{g,2500}$	kT (keV)	L_{bol} (10^{42} erg s^{-1})	References
2A0335+096	24^{+23}_{-6}	$1.1^{+1.0}_{-0.3}$	$10.4^{+1.4}_{-1.0}$	$1.04^{+0.03}_{-0.03}$	$0.10^{+0.01}_{-0.01}$	$3.46^{+0.09}_{-0.09}$	130^{+1}_{-1}	[1]
A85	37^{+37}_{-11}	$1.2^{+1.2}_{-0.4}$	$20.6^{+3.6}_{-2.7}$	$2.40^{+0.06}_{-0.06}$	$0.12^{+0.02}_{-0.02}$	$6.6^{+0.1}_{-0.1}$	471^{+2}_{-2}	[1]
A133	620^{+260}_{-20}	24^{+11}_{-1}	$12.4^{+4.5}_{-2.0}$	$1.04^{+0.06}_{-0.06}$	$0.08^{+0.03}_{-0.01}$	$4.4^{+0.1}_{-0.1}$	$96.1^{+0.8}_{-0.8}$	[1]
A262	$9.7^{+7.5}_{-2.6}$	$0.13^{+0.10}_{-0.03}$	$3.2^{+0.2}_{-0.2}$	$0.283^{+0.009}_{-0.008}$	$0.088^{+0.006}_{-0.005}$	$2.23^{+0.04}_{-0.04}$	$27.8^{+0.2}_{-0.2}$	[1]
A478	100^{+80}_{-20}	$1.5^{+1.1}_{-0.4}$	43^{+6}_{-5}	$5.4^{+0.3}_{-0.3}$	$0.13^{+0.02}_{-0.02}$	$7.5^{+0.3}_{-0.3}$	729^{+6}_{-6}	[1]
A496	172	2.34	$13.3^{+0.6}_{-0.7}$	$1.17^{+0.08}_{-0.05}$	$0.088^{+0.007}_{-0.006}$	$4.5^{+0.1}_{-0.1}$	123^{+1}_{-1}	[2]
A1795	160^{+230}_{-50}	$4.7^{+6.6}_{-1.6}$	$23.2^{+1.2}_{-1.1}$	$2.8^{+0.2}_{-0.2}$	$0.119^{+0.010}_{-0.009}$	$6.0^{+0.1}_{-0.1}$	366^{+3}_{-3}	[1]
A2029	87^{+49}_{-4}	$4.8^{+2.7}_{-0.1}$	34^{+3}_{-3}	$3.6^{+0.1}_{-0.1}$	$0.105^{+0.010}_{-0.009}$	$8.0^{+0.1}_{-0.1}$	869^{+4}_{-4}	[1]
A2052	150^{+200}_{-70}	$1.7^{+2.3}_{-0.7}$	$8.6^{+0.2}_{-0.2}$	$0.79^{+0.09}_{-0.09}$	$0.09^{+0.01}_{-0.01}$	$3.1^{+0.05}_{-0.05}$	90^{+1}_{-1}	[1]
A2199	270^{+270}_{-60}	$7.5^{+6.6}_{-1.5}$	$17.4^{+2.0}_{-1.3}$	$1.65^{+0.01}_{-0.01}$	$0.095^{+0.011}_{-0.007}$	$3.9^{+0.2}_{-0.2}$	118^{+3}_{-3}	[1]
A2204	280^{+50000}_{-0}	5.6	$55.2^{+3.0}_{-2.3}$	$6.0^{+0.2}_{-0.2}$	$0.108^{+0.007}_{-0.006}$	$9.2^{+0.3}_{-0.3}$	987^{+7}_{-7}	[3]
A2597	67^{+87}_{-29}	$3.6^{+4.6}_{-1.5}$	$14.4^{+0.7}_{-0.8}$	$1.33^{+0.04}_{-0.04}$	$0.092^{+0.005}_{-0.006}$	$4.00^{+0.05}_{-0.05}$	175^{+1}_{-1}	[1]
A4059	96^{+89}_{-35}	$3.0^{+2.5}_{-0.9}$	$15.3^{+1.0}_{-0.9}$	$1.02^{+0.04}_{-0.05}$	$0.067^{+0.005}_{-0.005}$	$4.4^{+0.2}_{-0.2}$	112^{+2}_{-2}	[1]
Centaurus	$7.4^{+5.8}_{-1.8}$	$0.060^{+0.051}_{-0.015}$	$^{*}8.2^{+0.2}_{-0.2}$	$0.46^{+0.06}_{-0.06}$	$0.056^{+0.007}_{-0.007}$	-	-	[1]
Hydra A	430^{+200}_{-50}	64^{+48}_{-11}	$16.0^{+1.2}_{-3.3}$	$1.65^{+0.03}_{-0.03}$	$0.10^{+0.01}_{-0.02}$	$3.79^{+0.07}_{-0.07}$	187^{+1}_{-1}	[1]
MKW3S	410^{+420}_{-44}	38^{+39}_{-4}	$12.4^{+7.5}_{-2.3}$	$0.96^{+0.02}_{-0.02}$	$0.08^{+0.05}_{-0.02}$	$4.3^{+0.2}_{-0.1}$	$78.1^{+0.9}_{-0.9}$	[1]
NGC507	19^{+14}_{-7}	$0.35^{+0.06}_{-0.04}$	$^{*}2.1^{+0.8}_{-0.4}$	$0.101^{+0.004}_{-0.004}$	$0.049^{+0.018}_{-0.011}$	$1.41^{+0.04}_{-0.04}$	$4.7^{+0.1}_{-0.1}$	[4],[5]
NGC1399	$1.2^{+0.5}_{-0.5}$	$0.11^{+0.05}_{-0.05}$	$^{\dagger}2.38^{+0.94}_{-0.90}$	-	-	-	-	[6]
NGC1550	15.4	0.17	$1.67^{+0.07}_{-0.05}$	$0.11^{+0.01}_{-0.01}$	$0.066^{+0.007}_{-0.006}$	$1.27^{+0.03}_{-0.03}$	$5.5^{+0.2}_{-0.2}$	[2]
NGC4636	$2.76^{+0.56}_{-0.91}$	0.012	$^{\dagger}0.82^{+0.28}_{-0.28}$	-	-	-	-	[4],[5]
NGC5044	$4.2^{+1.2}_{-2.0}$	0.049	$1.00^{+0.05}_{-0.05}$	$0.063^{+0.006}_{-0.005}$	$0.063^{+0.006}_{-0.006}$	$1.24^{+0.02}_{-0.02}$	$4.3^{+0.1}_{-0.1}$	[4],[5]
PKS1404-267	20^{+26}_{-9}	$0.12^{+0.15}_{-0.05}$	$^{*}3.2^{+0.1}_{-0.1}$	$0.225^{+0.005}_{-0.005}$	$0.069^{+0.003}_{-0.003}$	$1.66^{+0.04}_{-0.05}$	$11.4^{+0.2}_{-0.2}$	[1]
Sersic159/03	780^{+820}_{-260}	25^{+26}_{-8}	$9.5^{+1.1}_{-0.9}$	$0.84^{+0.03}_{-0.03}$	$0.09^{+0.01}_{-0.009}$	$2.53^{+0.04}_{-0.04}$	$71.9^{+0.4}_{-0.4}$	[1]
3C388	200^{+280}_{-80}	$5.2^{+7.5}_{-2.1}$	$6.7^{+1.0}_{-0.7}$	$0.45^{+0.09}_{-0.09}$	$0.067^{+0.017}_{-0.015}$	$3.39^{+0.24}_{-0.16}$	44^{+1}_{-1}	[1]
3C401	650^{+1200}_{-420}	11^{+20}_{-7}	$9.2^{+7.3}_{-2.6}$	$0.585^{+0.084}_{-0.066}$	$0.064^{+0.052}_{-0.020}$	$2.98^{+0.34}_{-0.31}$	49^{+2}_{-2}	[1]
4C55.16	420^{+440}_{-160}	12^{+12}_{-4}	$21.3^{+8.5}_{-4.7}$	$1.93^{+0.08}_{-0.11}$	$0.090^{+0.036}_{-0.020}$	$5.0^{+0.2}_{-0.2}$	304^{+5}_{-5}	[1]
A1835	1800^{+1900}_{-600}	47^{+50}_{-16}	48^{+3}_{-3}	$5.6^{+0.1}_{-0.1}$	$0.116^{+0.008}_{-0.008}$	$10.2^{+0.2}_{-0.2}$	1540^{+8}_{-8}	[1]
Cygnus A	1300^{+1100}_{-200}	84^{+70}_{-14}	$17.3^{+2.6}_{-1.9}$	$1.73^{+0.06}_{-0.06}$	$0.10^{+0.02}_{-0.01}$	$7.61^{+0.21}_{-0.20}$	287^{+2}_{-2}	[1]
HCG62	$3.9^{+6.1}_{-2.3}$	$0.046^{+0.073}_{-0.028}$	$1.70^{+0.02}_{-0.02}$	$0.055^{+0.005}_{-0.005}$	$0.032^{+0.003}_{-0.003}$	$1.06^{+0.02}_{-0.02}$	$1.97^{+0.05}_{-0.05}$	[1]
Hercules A	310^{+400}_{-90}	31^{+40}_{-9}	$20.8^{+7.8}_{-7.0}$	$1.64^{+0.22}_{-0.18}$	$0.078^{+0.031}_{-0.028}$	$5.06^{+0.17}_{-0.17}$	179^{+2}_{-2}	[1]
MACSJ0159.8-0849	377	13.3	56^{+120}_{-29}	$4.5^{+0.3}_{-0.3}$	$0.08^{+0.17}_{-0.04}$	$10.9^{+0.5}_{-0.6}$	1260^{+20}_{-20}	[7]
MACSJ0242.5-2132	353	8.96	23^{+46}_{-7}	$2.4^{+0.2}_{-0.4}$	$0.10^{+0.21}_{-0.03}$	$6.5^{+1.0}_{-0.8}$	576^{+20}_{-20}	[7]
MACSJ0429.6-0253	83	2.17	20^{+8}_{-4}	$2.22^{+0.38}_{-0.38}$	$0.11^{+0.05}_{-0.03}$	$8.1^{+1.5}_{-1.1}$	723^{+30}_{-30}	[7]

MACSJ0913.7+4056	7560	150	29^{+13}_{-5}	$2.3^{+0.3}_{-0.3}$	$0.081^{+0.037}_{-0.018}$	$7.3^{+0.7}_{-0.6}$	523^{+20}_{-20}	[7]
MACSJ1411.3+5212	3560	49.1	$17.2^{+5.7}_{-3.5}$	$1.83^{+0.17}_{-0.17}$	$0.11^{+0.04}_{-0.02}$	$6.0^{+0.5}_{-0.5}$	456^{+10}_{-10}	[7]
MACSJ1423.8+2404	1400^{+2500}_{-900}	61	$27.1^{+4.8}_{-3.4}$	$2.6^{+0.2}_{-0.2}$	$0.096^{+0.018}_{-0.014}$	$8.2^{+0.8}_{-0.6}$	801^{+20}_{-20}	[7]
MACSJ1532.8+3021	2200^{+900}_{-900}	270	42^{+43}_{-13}	$3.6^{+0.3}_{-0.3}$	$0.09^{+0.09}_{-0.03}$	$70^{+0.3}_{-0.3}$	867^{+10}_{-10}	[8]
MACSJ1720.2+3536	380	17.64	25^{+14}_{-9}	$3.2^{+0.2}_{-0.2}$	$0.12^{+0.07}_{-0.05}$	$8.13^{+0.61}_{-0.56}$	899^{+20}_{-20}	[7]
MACSJ1931.8-2634	8760	83.4	52^{+25}_{-16}	$4.4^{+0.3}_{-0.3}$	$0.084^{+0.041}_{-0.026}$	$7.9^{+0.4}_{-0.4}$	1060^{+10}_{-10}	[7]
MACSJ2046.0-3430	605	22.86	19^{+10}_{-3}	$2.2^{+0.1}_{-0.2}$	$0.12^{+0.06}_{-0.02}$	$5.2^{+0.5}_{-0.4}$	451^{+10}_{-10}	[7]
MACSJ2140.2-2339	179	3.43	19^{+3}_{-1}	$2.2^{+0.2}_{-0.2}$	$0.12^{+0.02}_{-0.01}$	$6.0^{+0.4}_{-0.4}$	479^{+10}_{-10}	[7]
MS0735.6+7421	6900^{+7600}_{-2600}	1600^{+1700}_{-600}	$28.5^{+9.9}_{-2.3}$	$2.90^{+0.08}_{-0.08}$	$0.10^{+0.04}_{-0.01}$	$6.72^{+0.08}_{-0.08}$	523^{+2}_{-2}	[1]
NGC5813	$3.97^{+1.02}_{-2.36}$	0.064	$^{\dagger}0.088^{+0.004}_{-0.004}$	-	-	-	-	[4],[5]
NGC5846	$0.88^{+0.30}_{-0.59}$	0.0022	$^{\dagger}0.12^{+0.04}_{-0.04}$	-	-	-	-	[4],[5]
Perseus	150^{+100}_{-30}	19^{+20}_{-1}	$^{*}15.0^{+0.3}_{-0.3}$	$1.74^{+0.01}_{-0.01}$	$0.116^{+0.002}_{-0.002}$	-	-	[1]
PKS0745-191	1700^{+1400}_{-300}	69^{+56}_{-10}	33^{+4}_{-3}	$4.0^{+0.2}_{-0.2}$	$0.12^{+0.02}_{-0.01}$	$8.0^{+0.2}_{-0.2}$	1200^{+10}_{-10}	[1]
RBS797	3340^{+1410}_{-1410}	38^{+50}_{-15}	50^{+27}_{-12}	$3.8^{+0.4}_{-0.4}$	$0.08^{+0.04}_{-0.02}$	$9.1^{+0.7}_{-0.6}$	926^{+20}_{-20}	[1]
Zw2701	920^{+180}_{-180}	$42.0^{+0.8}_{-0.8}$	19^{+4}_{-2}	$1.7^{+0.2}_{-0.2}$	$0.09^{+0.02}_{-0.01}$	$5.5^{+0.2}_{-0.2}$	267^{+4}_{-4}	[9]
Zw3146	5800^{+6800}_{-1500}	380^{+460}_{-110}	45^{+33}_{-16}	$5.1^{+0.9}_{-1.2}$	$0.11^{+0.08}_{-0.05}$	$8.5^{+0.6}_{-0.4}$	1300^{+20}_{-20}	[1]

Notes: [a]pV and P_{cav} values taken from the references listed, using $E_{cav} = 4pV$. We assume factor of 2 errors in systems without quoted error bars. [b]Masses marked with † are derived from Reiprich & Böhringer (2002), as described in section 4.6. References: [1] Rafferty et al. (2006), [2] Bîrzan et al. (2012), [3] Sanders, Fabian & Taylor (2009), [4] Cavagnolo et al. (2010), [5] Russell et al. (2013), [6] Shurkin et al. (2008), [7] Hlavacek-Larrondo et al. (2012), [8] Hlavacek-Larrondo et al. (2013), [9] Ma et al. in prep.

Chapter 4

Results and Discussion

4.1 Relationships between halo, gas, and stellar mass

Using our mass measurements, we investigate the relationships between the total mass, gas mass, and stellar mass in our systems. We fit the relationship between the gas mass within R_{2500} and M_{2500} in our HIFLUGCS systems using the bivariate correlated error and intrinsic scatter (BCES) method of Akritas & Bershady (1996), finding a relationship of $M_{g,2500}/10^{13}M_{\odot} = 10^{-1.27\pm0.05}(M_{2500}/10^{13}M_{\odot})^{1.20\pm0.04}$. This relation is well fit by a power law, with vertical scatter of $\approx 17\%$. Although we are measuring masses at a smaller radius, the slope of our relation is consistent with the relation at M_{500} of Gonzalez et al. (2013), who find a slope of 1.26 ± 0.03. Our M_g-M relation implies an increase of gas fractions with halo mass within R_{2500}, and at the highest mass of our sample it corresponds to a gas fraction of 0.12. Note that this does not include the contribution of stellar mass. Allen et al. (2008) find a universal gas fraction of $f_g = 0.1104 \pm 0.0016$ in relaxed clusters above 5keV. If we include the systems in our extended sample, both $f_g \propto M_{2500}^{0.2}$ and $f_g = 0.1104$ are good descriptions of our systems with $T > 5$ keV, with χ^2 values of 16.8 and 11.2 respectively for 25 data points. Our plot of $M_{g,2500}$ vs. M_{2500} in shown in Figure 4.1.

We investigate the fraction of stellar mass in the BCG to total baryonic mass in our systems. This is the fraction of the baryonic mass of a halo which was able to form stars in the BCG, and is a measure of the integrated star formation efficiency of the galaxy. We plot this fraction against gas mass at R_{2500} and against stellar mass of our BCGs in Figure 4.2. The integrated star formation efficiency of the BCG strongly decreases with the total gas mass of the systems, or equivalently with halo mass. Virial shocks in groups and clusters heat accreting gas, which limits the cooling gas that can reach the BCG in halos

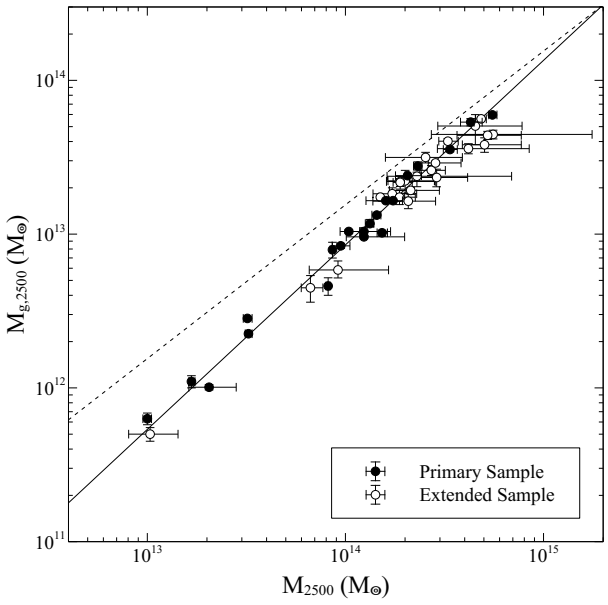

Figure 4.1: Gas mass within R_{2500} vs. M_{2500}. The solid line shows the best fit powerlaw to the primary sample, given by $M_{g,2500}/10^{13}M_\odot = 10^{-1.27}(M_{2500}/10^{13}M_\odot)^{1.2}$. The dotted line shows the Planck value of $\Omega_b/\Omega_m = 0.155$

above $\sim 10^{12}M_\odot$ (Dekel & Birnboim, 2006). However, the systems we analyse here contain massive cooling flows, and would significantly alter the relation in Figure 4.2 if they are unimpeded (discussed further in section 4.6). Additionally, thermal conduction can reduce, but not completely offset the cooling in massive cooling flows (Voigt & Fabian, 2004). The strong decrease in the integrated star formation efficiency of the BCGs suggests that there is an additional mechanism offsetting cooling flows in BCGs over long timescales.

4.2 Cluster Scaling Relations

Before investigating the scaling relations of cluster properties with AGN power, we first want to see how cluster-scale properties scale with each other in our sample. In this section, we calculate the M-T, L-T, and L-M relations for our sample. As we are using a flux limited sample, our luminosities are affected by the Malmquist bias, which causes the most luminous objects to be over-represented in a flux-limited sample. For a low-redshift sample with a log-normal distribution of intrinsic luminosities and no z cutoff, the bias on

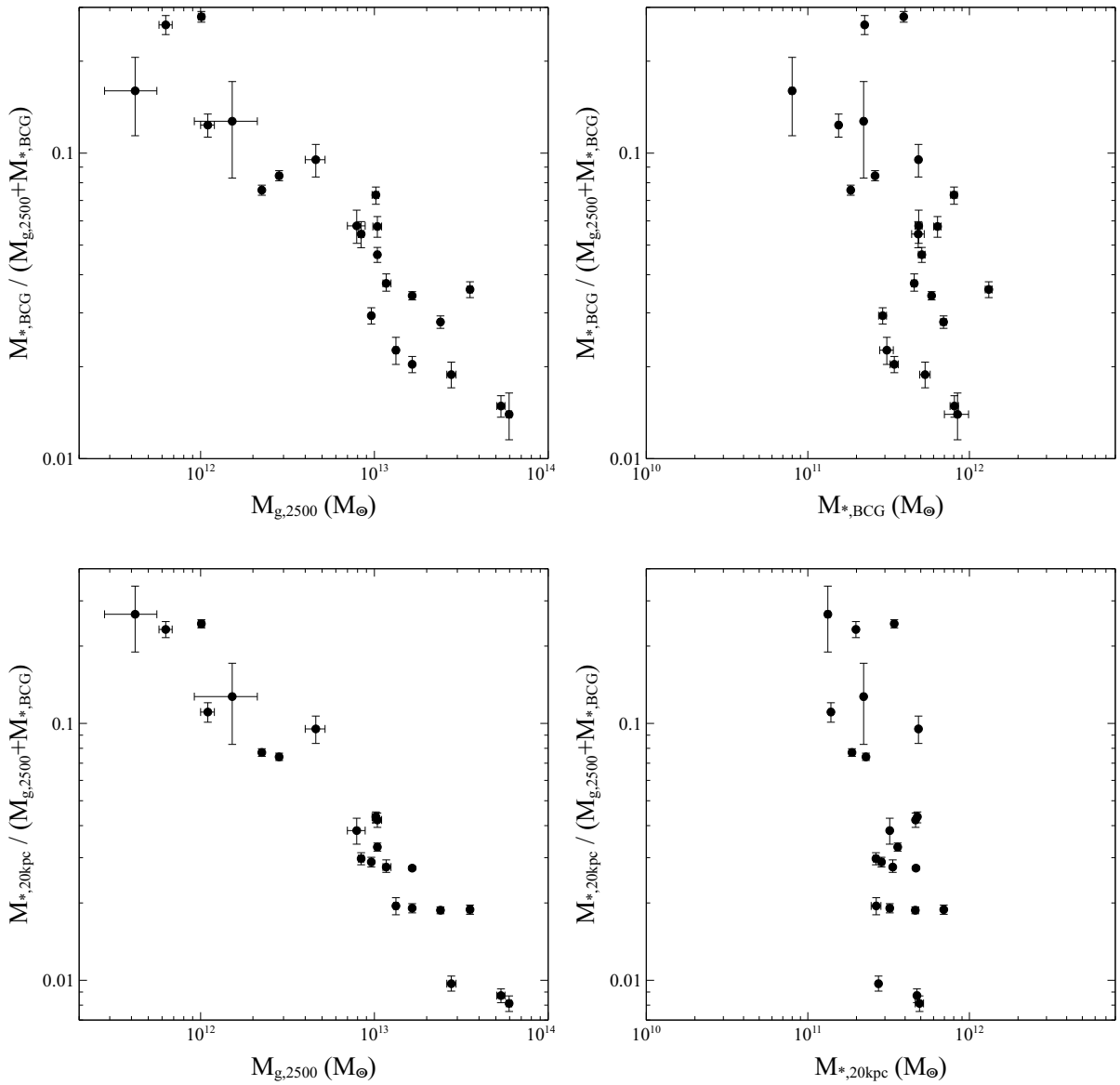

Figure 4.2: Top: $M_{*,\mathrm{BCG}}/(M_{g,2500} + M_{*,\mathrm{BCG}})$ vs. $\mathrm{M}_{g,2500}$ (*left*), $M_{*,\mathrm{BCG}}/(M_{g,2500} + M_{*,\mathrm{BCG}})$ vs. $\mathrm{M}_{*,\mathrm{BCG}}$ (*right*). Bottom: Same as above, but with stellar mass calculated at 20kpc.

Table 4.1: Cluster Scaling Relations
Fit Results to log(y) $= a + b$ log(x)

y	x	a	b	σ^a
$\frac{L_{\rm bol}}{10^{42}\ {\rm erg\ s^{-1}}}$	$\frac{M_{2500}}{10^{13}M_\odot}$	0.40($\pm$0.11)	1.55($\pm$0.09)	0.15
$\frac{L_{\rm bol}}{10^{42}\ {\rm erg\ s^{-1}}}$	$\frac{T_x}{\rm keV}$	0.43($\pm$0.07)	2.76($\pm$0.09)	0.15
$\frac{M_{2500}}{10^{13}M_\odot}$	$\frac{T_x}{\rm keV}$	0.02($\pm$0.07)	1.78($\pm$0.11)	0.11
$\frac{M_{g,2500}}{10^{13}M_\odot}$	$\frac{M_{2500}}{10^{13}M_\odot}$	-1.27($\pm$0.05)	1.20($\pm$0.04)	0.07

Note: $^a\sigma$ is the standard deviation of the log-normal residuals for each relation.

L in the L-M relation can be expressed as $\Delta \ln L = \frac{3}{2}\sigma^2$, where σ is the log-normal scatter in L for a given mass (described in Vikhlinin et al. 2009). The bias in the L-T relation would be equivalent, but where σ is the log-normal scatter in L for a given temperature. Correcting for the Malmquist bias in our sample then simply modifies the normalization of our relations involving luminosity.

We fit the L-M, L-T, and M-T relations with the bivariate correlated error and intrinsic scatter (BCES) method of Akritas & Bershady (1996). We do not include evolution in the scaling relation fits in this section in order to directly compare with the results of section 4.3, which makes no assumptions about the redshift evolution of cavity scaling relations. Our sample is at low redshift, so the evolutionary corrections are likely to be small. Our best fit relations are given by $L \propto T^{2.76\pm0.09}$, $L \propto M^{1.55\pm0.09}$, $M \propto T^{1.78\pm0.10}$, and are shown in Figure 4.3. These relations are consistent with results of previous studies that span group to cluster masses (see Giodini et al. 2013 for a review). Note that when only high mass halos are included, measured M-T relations are usually found to be closer to the $M \propto T^{3/2}$ expected from self-similar evolution (Arnaud, Pointecouteau & Pratt, 2005; Vikhlinin et al., 2006). Beyond the cooling core, the properties of these systems currently experiencing feedback are consistent with the cluster population as a whole, including non cool-core clusters.

This result seems to imply either that mechanical feedback is not strongly affecting the overall temperature and luminosity of clusters beyond the cooling radius, or that all clusters have experienced a significant level of heating from AGN. We investigate if a history of AGN heating is energetically capable of shaping the observed scaling relations in section 4.6.3.

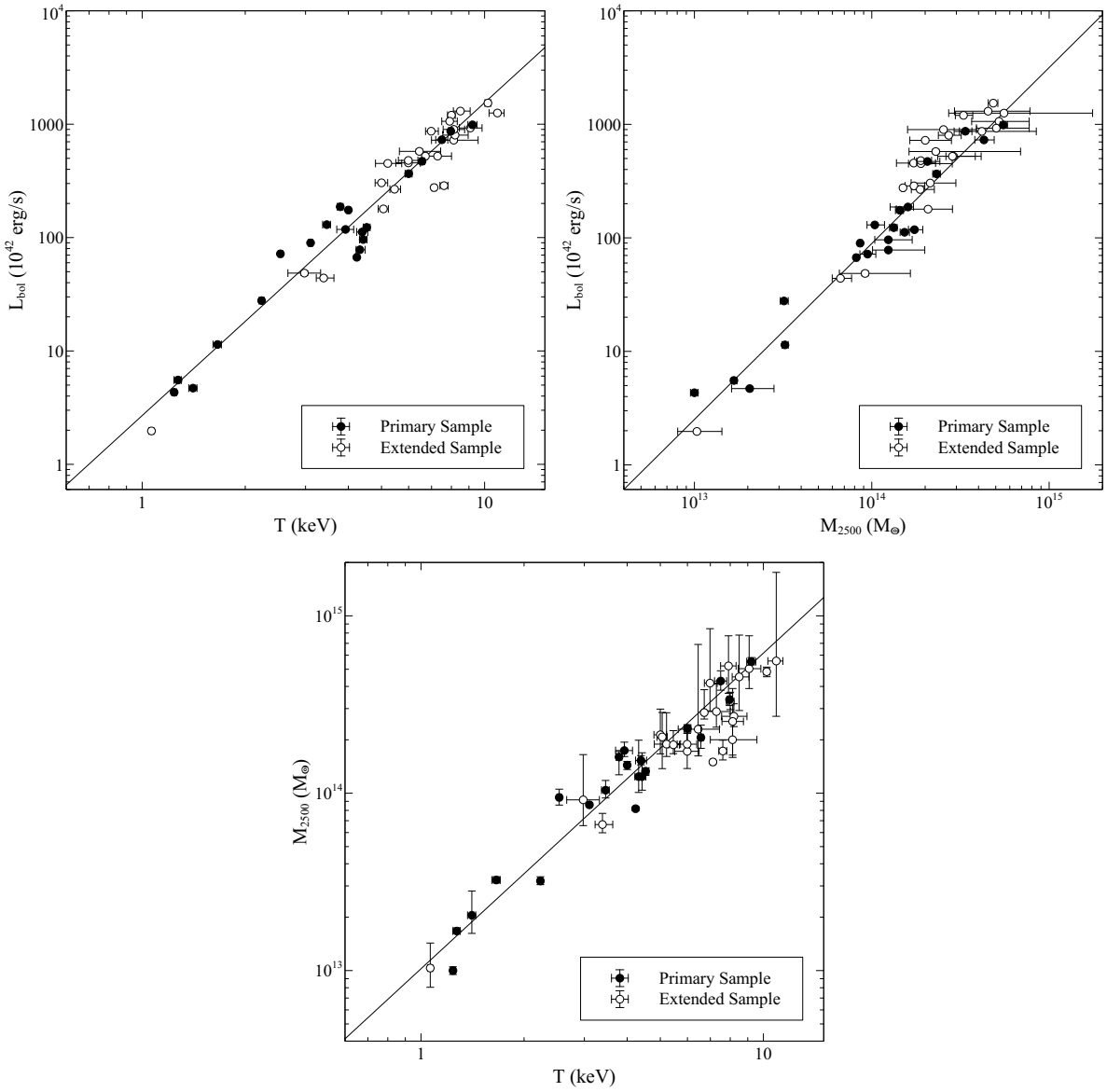

Figure 4.3: Cluster scaling relations between temperature, bolometric X-ray luminosity, and M_{2500}. Luminosity and temperature are measure in the aperture (0.3-1.0)R_{2500}. The solid line shows the best fit powerlaw to the primary sample. *Left:* Luminosity vs temperature. *Center:* luminosity vs. M_{2500}. *Right:* M_{2500} vs. temperature.

4.3 Scaling Relations with E_{cav}, P_{cav}

The scaling relations of AGN jet power with cluster properties, and cluster mass in particular, are often an input into cosmological simulations. Sijacki & Springel (2006) adopted a simple model for the relationship E_{cav} with M. They make the assumptions that $E_{cav} \propto M_{BH}$, where M_{BH} is the black hole mass, and that the mass of the central galaxy is proportional to M_{200}. The assumption $E_{cav} \propto M_{BH}$ is equivalent to assuming that the accretion rate is a fixed fraction of the Eddington rate, since $\dot{M}_{Edd} \propto M_{BH}$. Using the M_{BH}-σ relation of $M_{BH} \propto \sigma^4$ (Ferrarese & Merritt, 2000; Gebhardt et al., 2000) leads to $E_{cav} \propto M_{200}^{4/3}$ under their assumptions. Alternatively, an M_{BH}-σ relation of $M_{BH} \propto \sigma^5$ (McConnell & Ma, 2013) would lead to $E_{cav} \propto M_{200}^{5/3}$.

Mechanical AGN power has been found to have a linear relationship with the bolometric cooling luminosity of the cooling flow region (Rafferty et al., 2006; Dunn & Fabian, 2006; Hlavacek-Larrondo et al., 2012). Then if $L_{cool} \propto L_{bol}$, this would imply that $P_{cav} \propto L_{bol}$. If this linear relationship holds, then the mechanical AGN power should follow the scaling relations of X-ray luminosity with other system properties. This would lead to an expected $P_{cav} \propto M^{4/3}$ for self-similar evolution, or $P_{cav} \propto M^{1.55}$ for the $L - M$ relation derived in the previous section.

We fit a powerlaw to the relationships between E_{cav} and P_{cav} with different cluster-scale properties in our primary sample. A2204 is excluded from our fits due to the large systematic uncertainty in the energetics of the outer cavity system (Sanders, Fabian & Taylor, 2009). The relations with cluster mass and stellar mass of the BCG are shown in Figure 4.4. The rest of our fitting results are shown in Table 4.2, along with the standard deviation of the logarithmic residuals. The error on the scatter is calculated through bootstrap resampling with 10000 iterations. The X-ray derived quantities of M_{2500}, $M_{g,2500}$, T, L_{bol} all have consistent scatter with P_{cav}. The relation between P_{cav} and M_g is qualitatively very similar to the relation between P_{cav} and M_{2500}, due to the tight correlation between M_{2500} and M_g. Additionally, the scatter between P_{cav} and the BCG stellar mass is 0.68±0.09 dex, larger than the relations involving halo mass or gas mass, but consistent within the combined 1-σ errors.

We find an E_{cav}-M_{2500} relation of $\log(E_{cav}/10^{58}\mathrm{erg}) = 2.04(\pm0.30)\log(M_{2500}/10^{13}M_\odot) - 1.13(\pm0.25)$, steeper than either of the analytic scalings adopted in Sijacki & Springel (2006). However, the slope of our relation is only mildly inconsistent with the $E_{cav} \propto M^{5/3}$ derived from an M-σ relation of $M \propto \sigma^5$. The analytic E_{cav}-M relations of Sijacki & Springel (2006) implicitly use the assumption that the accretion onto the black hole is some fixed fraction of the Eddington accretion rate. If the accretion rate changes with cluster

Table 4.2: Scalings of cluster properties with P_{cav}

Fit Results to $\log\left(\frac{P_{cav}}{10^{42}\ \mathrm{erg\ s^{-1}}}\right) = a + b\ \log(\mathrm{x})$

x	a	b	σ^a
$\frac{M_{2500}}{10^{13}M_\odot}$	0.32(±0.24)	1.55(±0.26)	0.56(±0.08)
$\frac{M_g}{10^{13}M_\odot}$	1.97(±0.14)	1.18(±0.22)	0.54(±0.08)
$\frac{L_{\mathrm{bol,total}}}{10^{42}\ \mathrm{erg\ s^{-1}}}$	0.0(±0.6)	0.83(±0.23)	0.56(±0.08)
$\frac{L_{\mathrm{bol,excised}}}{10^{42}\ \mathrm{erg\ s^{-1}}}$	0.1(±0.5)	0.93(±0.23)	0.61(±0.09)
$\frac{L_{\mathrm{bol,core}}}{10^{42}\ \mathrm{erg\ s^{-1}}}$	0.2(±0.5)	0.80(±0.22)	0.55(±0.08)
$\frac{T_x}{keV}$	0.52(±0.27)	2.51(±0.41)	0.61(±0.08)
$\frac{Y_x}{10^{13}keV\,M_\odot}^b$	1.49(±0.15)	0.84(±0.18)	0.57(±0.08)
$\frac{M_{*,\mathrm{BCG}}}{10^{11}M_\odot}$	0.22(±0.36)	2.50(±0.56)	0.68(±0.08)
$\frac{M_{*,20\mathrm{kpc}}}{10^{11}M_\odot}$	0.06(±0.51)	3.35(±0.92)	0.73(±0.09)

Notes: $^a\sigma$ is the standard deviation of the log-normal residuals for each relation. $^b\mathrm{Y}_x$ is calculated as $M_g \times T_x$.

properties, this could change our cavity scaling relations. We investigate the accretion rate of the systems in our sample in section 4.5.2.

The P_{cav}-L relation is consistent with a linear scaling of cavity power and luminosity, and the P_{cav}-M and P_{cav}-T are consistent with the L-M and L-T relations from the previous section, but with higher scatter. The relation of $P_{cav} \propto M_{2500}^{1.55\pm0.26}$ is also consistent with the self-similar relation of $P_{cav} \propto M_{2500}^{4/3}$, while $P_{cav} \propto T^{2.5\pm0.4}$ is mildly inconsistent with the self-similar expectation of $P_{cav} \propto T^2$. However, there is reason to believe that a linear scaling between cavity power and luminosity may not hold at lower masses than we are probing here. The roughly linear relationship between the X-ray cooling luminosity and cavity power in clusters flattens out in elliptical galaxies (Nulsen et al., 2009).

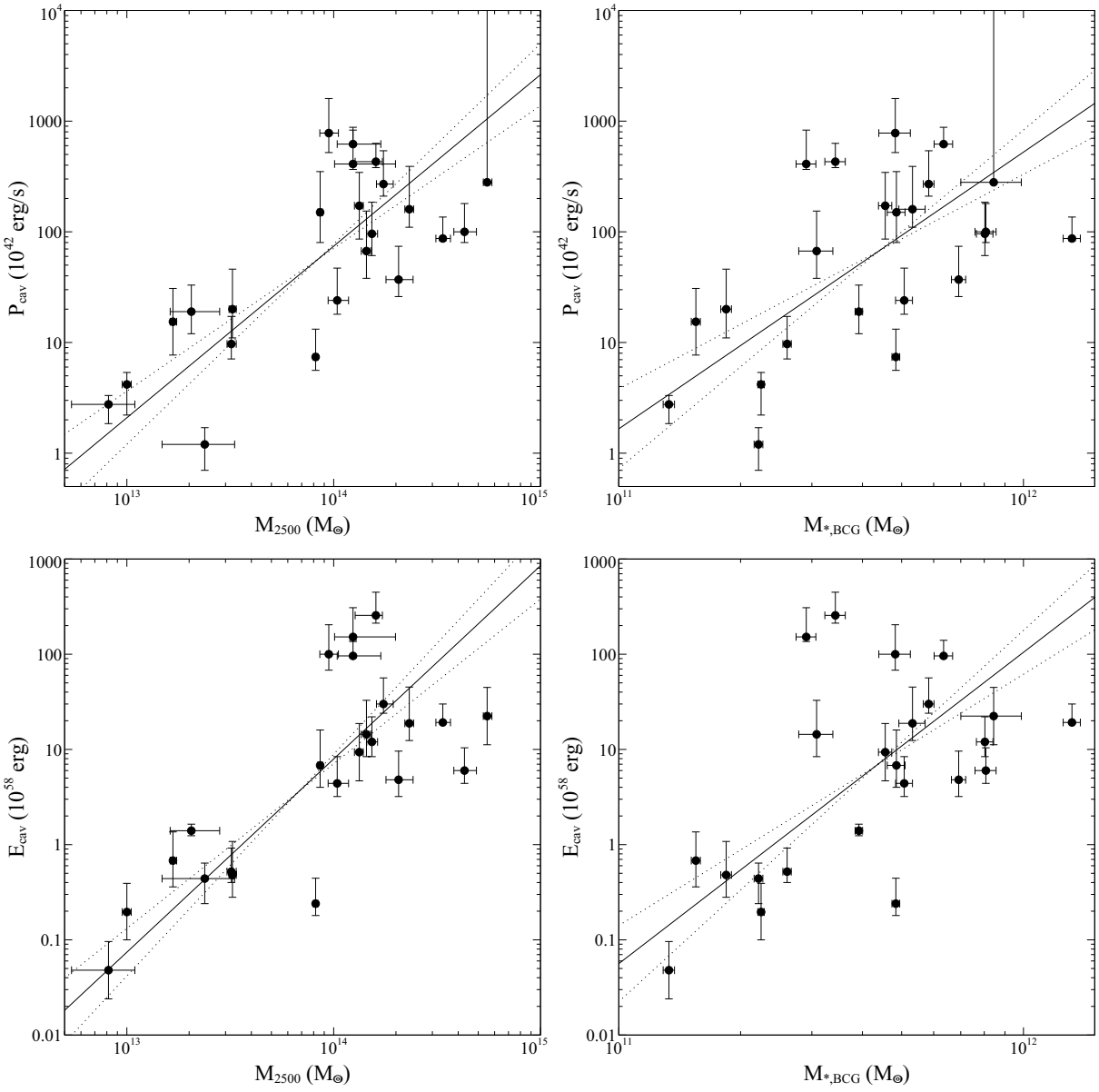

Figure 4.4: Top: Cavity power vs. M_{2500} (*Left*) and vs. $M_{*,BCG}$ (*Right*). Bottom: Cavity energy vs. M_{2500} (*Left*) and vs. $M_{*,BCG}$ (*Right*). The solid line denotes the best BCES bisector fit between the variables, and the dotted lines represent the 1-σ errors from bootstrap resampling. Cavity energy calculated as $E_{cav} = 4pV$.

4.4 Investigating Possible biases

4.4.1 Induced Correlations

In this section, we investigate how biases in cavity detections could affect the relations involving cavity power. One possibility is a preferred angular size for cavities to be detected, set by the limitations of Chandra's linear resolution and exposure times. This would cause a spurious correlation with redshift, and cavity power would scale as D_A^2, since $V \propto D_A^3$, and $t_{\rm buoy} \propto D_A$. In a flux-limited sample, this could cause a spurious correlation between the cavity power and total luminosity. To investigate this effect, we look at the angular sizes of all of the detected cavities in our sample.

The angular area of the cavities in our systems are plotted against angular diameter distance in Figure 4.5. The angular areas of detected cavities span 3 decades, and on average decrease with redshift. This provides evidence against a significant bias towards detecting cavities of a particular angular size. This implies that cavity sizes are not strongly biased by redshift, and correlations of cavity power with redshift dependent quantities are likely physical correlations.

Several other factors suggest that our observed relation between halo mass and $P_{\rm cav}$ is real. It is unlikely that much more powerful outbursts are missed in the nearby low-mass systems in our sample, as they would be easily detected. In the full HIFLUGCS sample, we also find a strong correlation in the short cooling time systems between $P_{\rm mech}$ and halo mass by using 1.4 GHz luminosity as a measure of cavity power, shown in Figure 4.10. All of the systems with short central cooling times ($t_c < 1$ Gyr) in HIFLUGCS are radio audible, so we are not missing any objects to the bottom-right or top-left of the relation. We conclude that our relation between $P_{\rm cav}$ and M_{2500} is likely real, but a larger complete sample would be beneficial to measure it to greater accuracy.

4.4.2 Reduced Scatter

The observed scatter in our measured relations could be reduced by degeneracy in our parameters. Here, we investigate potential biases between the scatter between $P_{\rm cav}$, halo mass, and the stellar mass of the BCG. Cavity powers and hydrostatic masses share a common dependence on the X-ray determined pressure of the ICM. Also, the buoyancy timescale used in determining cavity power has a dependence on the stellar velocity dispersion of the BCG. One way to make $P_{\rm cav}$ and M_{2500} fully independent would be to use lensing masses, which unfortunately have only been measured in a few of our systems. However,

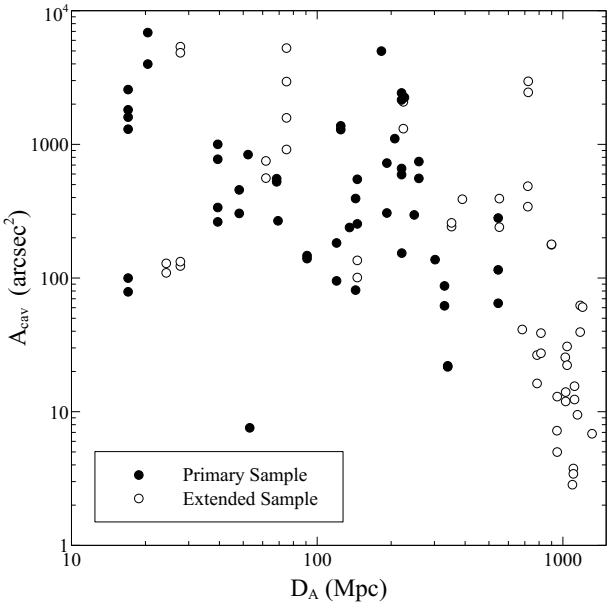

Figure 4.5: Angular area of all detected cavities in our sample vs. angular diameter distance. If there is a bias towards detecting a specific angular size of cavities, the relation should appear flat with small scatter.

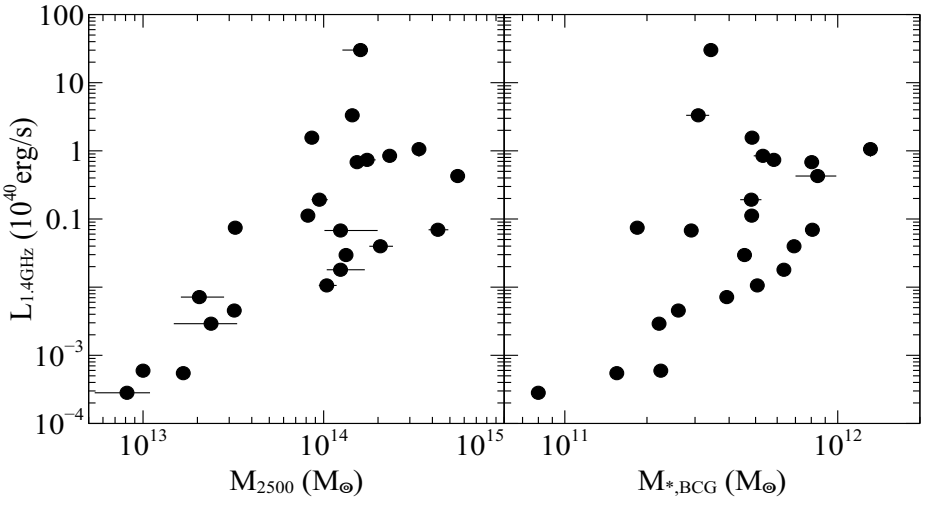

Figure 4.6: *Left*: 1.4 GHz luminosity vs. M_{2500}. *Right*: 1.4 GHz luminosity vs. $M_{*,BCG}$.

the intrinsic scatter between hydrostatic and weak lensing measurements of M_{2500} in cool-core clusters has been found to be less than 10%, or $\lesssim 0.04$ dex (Mahdavi et al., 2013). A degeneracy between P_{cav} and M_{2500} may exist, but it should be a small effect.

Another way to break the degeneracy is to use an independent measure of the mechanical power from the AGN. As such, we plot M_{2500} and $M_{*,BCG}$ against the monochromatic 1.4 GHz luminosity of the central radio source, shown in figure 4.6. We find that both M_{2500} and $M_{*,BCG}$ are strongly correlated with $L_{1.4GHz}$, with log-normal scatter of 0.88±0.14 dex and 1.12±0.16 dex respectively. The BCG stellar mass shows a suggestion of larger scatter with P_{cav} than M_{2500}, but is within the combined 1-σ errors.

4.5 Extended Sample

4.5.1 Cavity power scaling relations

We investigate the $P_{cav} - M_{2500}$ and $P_{cav} - L_{bol}$ relation including all of the systems in our extended sample. Most of the clusters seem to follow the $P_{cav} - M_{2500}$ relation derived in section 4.3, although the more massive clusters seem to lie preferentially above. We find a best fit relation of $P_{cav} \propto M_{2500}^{2.00\pm0.17}$ in our full sample, marginally inconsistent with the $P_{cav} \propto M_{2500}^{1.55\pm0.26}$ for our primary sample. This effect could either be explained by evolution of the $M - P_{cav}$ relation, or by selection biases in our extended sample. Specifically, we are biased towards detecting the largest cavities, and we could be missing objects lying in the bottom right of the graph. This bias is especially relevant at higher z, where smaller outbursts would be much more difficult to observe. Our best fit $P_{cav} - L_{bol}$ relation of our full sample is $P_{cav} \propto L_{cav}^{1.14\pm0.11}$, steeper but consistent with the relation of our primary sample, and marginally inconsistent with a linear scaling. The $P_{cav} - M_{2500}$ and $P_{cav} - L_{bol}$ relations for our full sample are shown in Figure 4.7.

4.5.2 Accretion Rate

As matter accretes onto the central SMBH, the binding energy released by the accreting mass will drive an outburst with some efficiency ϵ. Assuming that the X-ray cavities dominate the total energy output of the AGN, the accretion rate can be estimated as:

$$\dot{M}_{BH} = \frac{P_{cav}}{\epsilon c^2}. \tag{4.1}$$

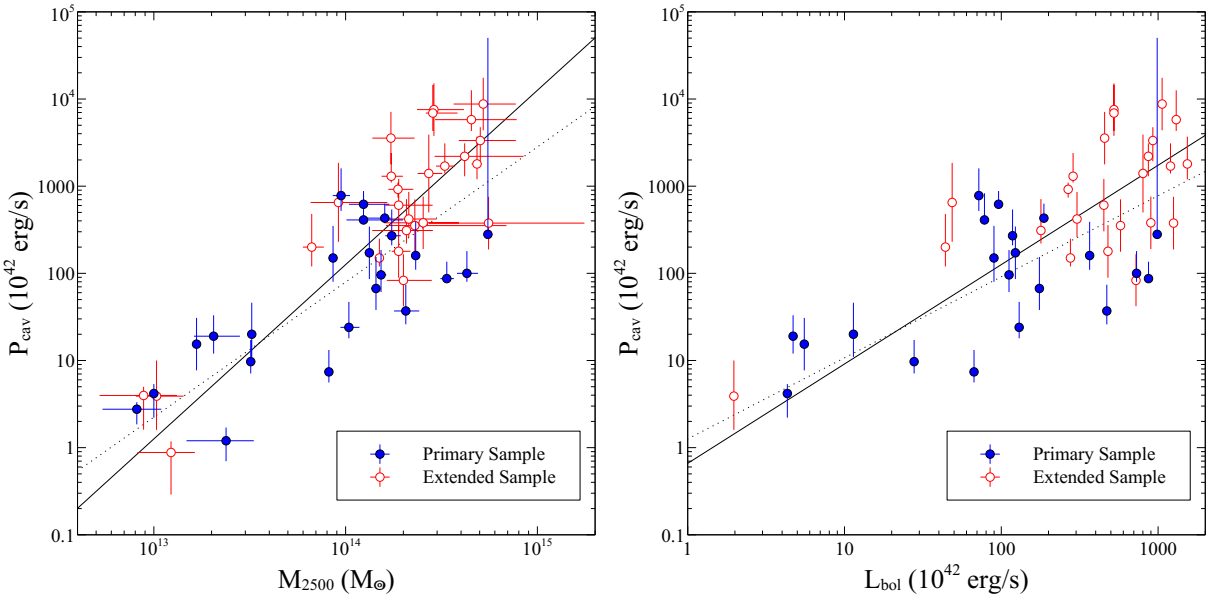

Figure 4.7: *Left:* Cavity power vs. M_{2500} in the extended sample. *Right:* Cavity power vs. L_{bol} in the aperture $(0.3\text{-}1.0)R_{2500}$ in the extended sample. The solid line is the best fit relation to the full sample, and the dotted line is the best fit to the primary sample.

The maximum accretion rate in which gravity is balanced by radiation pressure from accretion is given by the Eddington accretion rate, which for a fully ionized plasma can be calculated as (Rybicki & Lightman, 2008)

$$\frac{\dot{M}_{\rm Edd}}{M_\odot} = \frac{2.2}{\epsilon}\left(\frac{M_{\rm BH}}{10^9 M_\odot}\right). \tag{4.2}$$

The analytic scalings of cavity energy with halo mass in Sijacki & Springel (2006) discussed in section 4.3 rely on the assumption that the accretion rate is a low, fixed fraction of the Eddington rate. In this section, we investigate whether accretion efficiency a constant function of mass in our sample.

In Figure 4.8 we plot $\dot{M}/\dot{M}_{\rm Edd}$ against halo mass. The accretion rate in our systems ranges from $10^{-5}\dot{M}_{\rm Edd} - 0.04\dot{M}_{\rm Edd}$, all well below the Eddington rate, and in the range expected for radiatively inefficient accretion. We observe a weak positive trend between accretion rate and halo mass. This trend could be real, or it could be caused by a systematic underestimate of our black hole masses. This could be caused by poor surface brightness modelling of massive BCGs, similar to what has been observed in SDSS (Bernardi et al.,

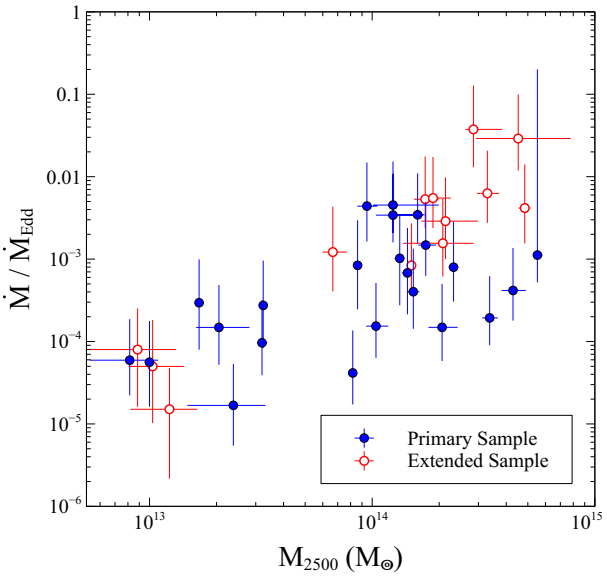

Figure 4.8: Accretion rate vs. halo mass. Blue points are from the primary sample, while red points are the systems in the extended sample with M_K values. Black hole masses are estimated from Graham (2007) using K-band luminosities derived from 2MASS, and $\dot{M}_{BH}$ is estimated as $\dot{M}_{BH} = \frac{P_{cav}}{\epsilon c^2}$.

2013). Also, the graph plotted is explicitly a relation between P_{cav}/L_K and M_{2500}, and the assumptions used to derive $\dot{M}$ and $\dot{M}_{Edd}$ rely on scaling relations between M_{BH} and M_K. Empirical relations to derive black hole mass are not well constrained above $M_{BH} \sim 10^9 M_\odot$, and there is even some suggestion of an upturn to larger black hole masses (Lauer et al., 2007). If the accretion rate is constant function of mass in our sample at $\dot{M}/\dot{M}_{Edd} = 10^{-4}$, it would imply black hole masses of $M_{BH} \gtrsim 10^{10} M_\odot$ in our high-mass systems.

4.6 AGN heating in full HIFLUGCS sample

4.6.1 Central cooling time

Our results above reveal strong correlations between AGN power and cluster properties. However, cavity systems are almost exclusively found in strong cool-core systems. This means that a sample comprised entirely of cavity systems is not representative of the

cluster population as a whole. Results from previous studies suggest that AGN power may scale differently with cluster properties in non-cool core systems. Mittal et al. (2009) found a correlation between the radio luminosity and the bolometric X-ray luminosity in strong cool-core systems, but no evidence for a correlation in weak or non cool-cores. Additionally, Ma, McNamara & Nulsen (2013) found only a weak trend between X-ray luminosity and radio luminosity. Their method involves correlating ROSAT luminosities to NVSS radio luminosities, and includes both cool and non-cool core clusters. In this section we investigate the effects of AGN heating including all of the HIFLUGCS systems.

Hudson et al. (2010) showed the central cooling time to be the best means of distinguishing a cool-core in systems with high quality X-ray data. We then separate our sample into two populations, systems with central cooling time < 1 Gyr, and systems with central cooling times have > 1 Gyr. Cooling time profiles at the centres of clusters continue to decrease with radius (Panagoulia, Fabian & Sanders, 2014), so it is important to define the central cooling time in a way that is not biased by resolution effects. We use the t_c values of Hudson et al. (2010), where the central cooling times are all determined at a consistent radius of $0.004R_{500}$. This radius is reached by the data in all of the systems in their sample, so their t_c values are unlikely to be biased by resolution effects.

4.6.2 M-$P_{\rm mech}$ relation

In all HIFLUGCS systems, we estimate the mechanical power from the 1.4 GHz radio luminosity using the relation from Cavagnolo et al. (2010):

$$\log P_{\rm mech} = 0.75(\pm 0.14)\log P_{1.4} + 1.91(\pm 0.18), \tag{4.3}$$

where $P_{\rm mech}$ is in units of 10^{42} erg s^{-1} and $P_{1.4}$ is in units of 10^{40} erg s^{-1}. This relation has been measured over the full range of radio luminosities in our sample, and has a scatter of 0.78 dex. As many of our systems do not have observed cavities, we will refer to the power estimated from this relation as the mechanical power, or $P_{\rm mech}$ throughout this section. We take radio luminosities from Bîrzan et al. (2012), which are either detections or upper limits derived from noise in the NVSS images. As a time consideration, we derive M_{2500} for the remaining HIFLUGCS systems from the parameters in Reiprich & Böhringer (2002). ROSAT, ASCA, and Einstein are used for these mass measurements, and likely have different systematics than our Chandra based mass measurements. To correct for this, we compare how our mass measurements differ in the 24 systems where we have already determined M_{2500} using Chandra data. We find that the average ratio of our measurements to be $M_{2500}/M_{2500,\rm Reiprich} = 1.18$, with a $1-\sigma$ scatter of 0.33, and we plot our comparison

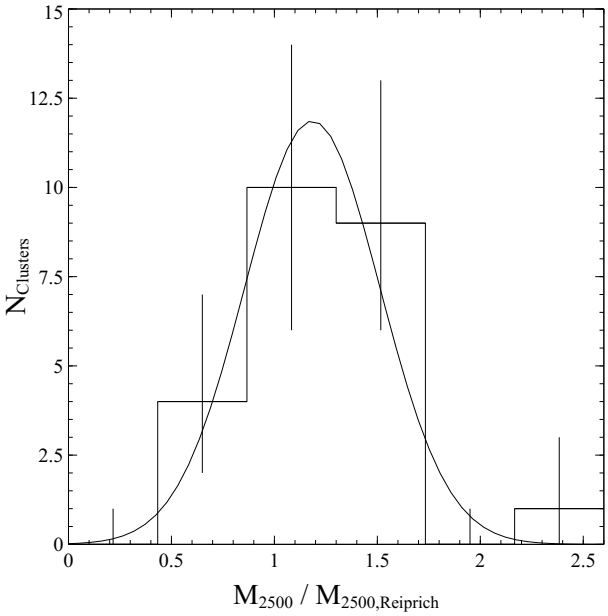

Figure 4.9: Distribution of the ratio of our M_{2500} measurements to the M_{2500} measurements of Reiprich & Böhringer (2002), used as a correction factor to estimate M_{2500} for the remaining systems in our sample.

between the mass measurements in Figure 4.9. We apply this ratio to the M_{2500} values derived from Reiprich & Böhringer (2002) to estimate M_{2500} for the rest of the HIFLUGCS systems.

We plot the mechanical power estimated from equation 4.3 against M_{2500} for the full HIFLUGCS sample in Figure 4.10. Mechanical power is found to be a function of both halo mass and the central cooling time. There is a clear offset between the distributions of $P_{\rm mech}$ for the systems having short and long central cooling times. The bulk of the systems with $t_c > 1$ Gyr experience outbursts that are 2 orders of magnitude less powerful than typical for systems with shorter cooling times. Nevertheless, a small fraction of the systems with long central cooling time exhibit powerful AGN outbursts. In Figure 4.10, we overlay our $P_{\rm cav}$-M_{2500} relation from section 4.3 and plot its 2σ scatter as a threshold to determine which systems have high mechanical power for a given halo mass. We find $11/36(\sim 30\%)$ of the $t_c > 1$ Gyr systems are above this threshold, while all 28 of the $t_c < 1$ Gyr systems harbour powerful radio outbursts.

The AGN in short cooling time systems could be fueled by their cooling atmospheres, while the mechanism fueling the long cooling time systems is unknown. Unresolved coronae

(Sun et al., 2009) or cold gas accreted from interloping galaxies (Hardcastle, Evans & Croston, 2007) may be important. This result shows heating from AGN is significant in all clusters, but systems with long central cooling times are not necessarily heated by a feedback cycle.

4.6.3 Energy per particle injected by AGN

Wu, Fabian & Nulsen (2000) estimate that an additional energy injection of $\sim 1-3$ keV particle^{-1} into the ICM is needed to reproduce the observed scaling relations in clusters, where the range in values corresponds to different heating prescriptions. The injection of energy into the IGM before virialization (pre-heating Evrard & Henry 1991; Kaiser 1991) would reduce the energy requirements further. The energy per particle injected by an AGN outburst can be calculated as

$$E/\mathrm{par} = \frac{E_{\mathrm{cav}}\mu m_p}{M_g}. \tag{4.4}$$

We calculate the energy per particle within R_{2500} injected from AGN outbursts for the systems in our extended sample. We use the energy injected within R_{2500} since it is accurately measured in our sample, but note that if the energy is spread throughout the full cluster volume these values are high by factors of $2-3$. We plot this against cluster mass in Figure 4.12. We find a weak positive trend between energy per particle and halo mass, with considerable scatter. The energy output in the majority of our systems is well short of the $\sim 1-3$ keV particle^{-1} needed to reproduce the observed scaling relations. In MS0735.6+7421, the system harbouring the most energetic outburst in our sample, the energy output within R_{2500} is ~ 0.8 keV particle^{-1} or ~ 0.3 keV particle^{-1} within R_{500}. In the most extreme cases, single massive outbursts can contribute a significant amount of energy into the ICM, comparable to the excess energy needed to break self-similarity.

Ma, McNamara & Nulsen (2013) find that the energy from radio AGN integrated to z=2 can exceed 1 keV particle^{-1} within R_{500}, and find that the integrated energy per particle heating decreases with increasing cluster luminosity (see also Giodini et al. 2010; Best et al. 2007). Using our relationships of $P_{\mathrm{cav}} \propto M_{2500}^{1.55}$, $M_{g,2500} \propto M_{2500}^{1.2}$, we find that the rate of energy input within R_{2500} is E particle$^{-1}s^{-1} \propto M_{2500}^{0.35}$. However, our result was derived only using systems currently exhibiting cavities, and does not take energy lost to radiative cooling into account. Figure 4.10 shows a much weaker trend between halo mass and AGN power when all clusters are included. The weakening of the relationship between mass and AGN power would then increase the relative contribution of energy per particle in low mass systems, since $E/\mathrm{par} \propto P_{\mathrm{mech}}/M_g$.

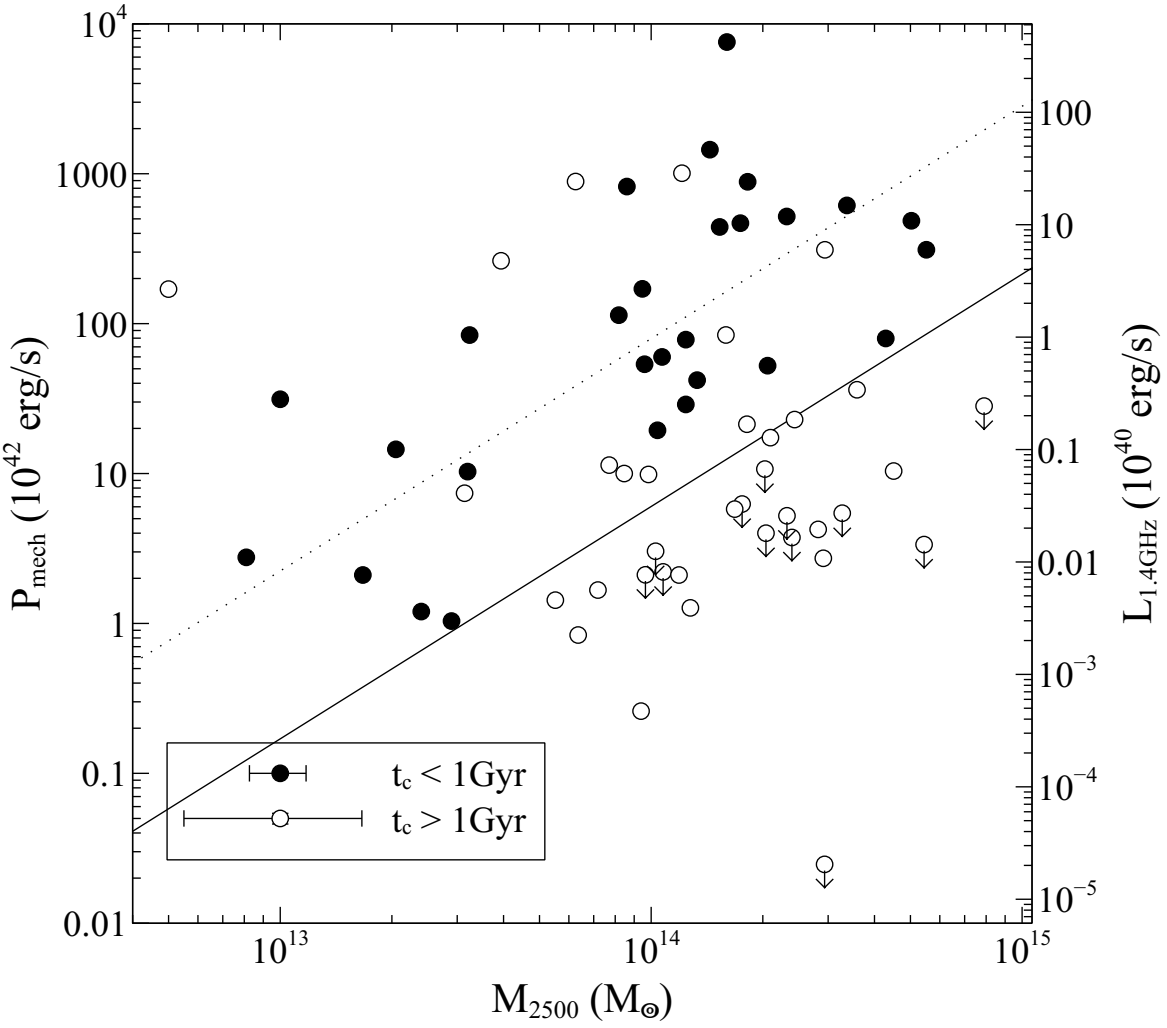

Figure 4.10: 1.4 GHz luminosity vs. M_{2500} in the full HIFLUGCS sample, with mechanical powers estimated using equation 4.3. Systems are shown as either open or closed symbols based on the central cooling times from Hudson et al. (2010). The dotted line is our best fit P_{mech}-M_{2500} relation from section 4.3, and the solid line is the 2-σ lower limit on the relation. The average size of the error bars is shown at the bottom left. The average error on the 1.4 GHz is smaller than the symbol size, and there is a scatter of 0.78 dex in the relationship between $L_{1.4GHz}$ and P_{mech}.

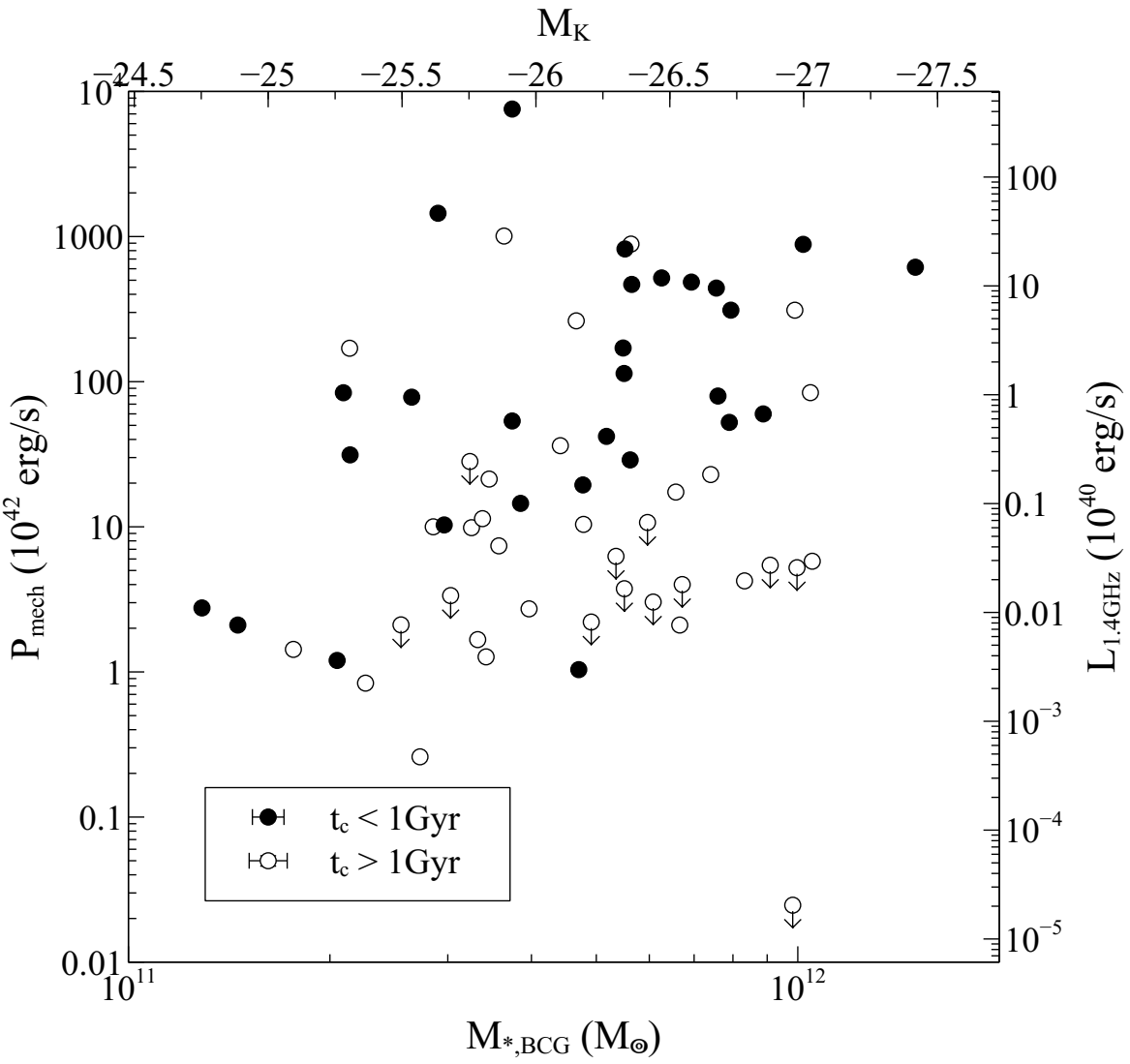

Figure 4.11: 1.4 GHz luminosity vs. $M_{*,BCG}$ in the full HIFLUGCS sample, with mechanical powers estimated using equation 4.3. Systems are shown as either open or closed symbols based on the central cooling times from Hudson et al. (2010). The average size of the error bars is shown at the bottom left. The average error on the 1.4 GHz is smaller than the symbol size, and there is a scatter of 0.78 dex in the relationship between $L_{1.4GHz}$ and P_{mech}.

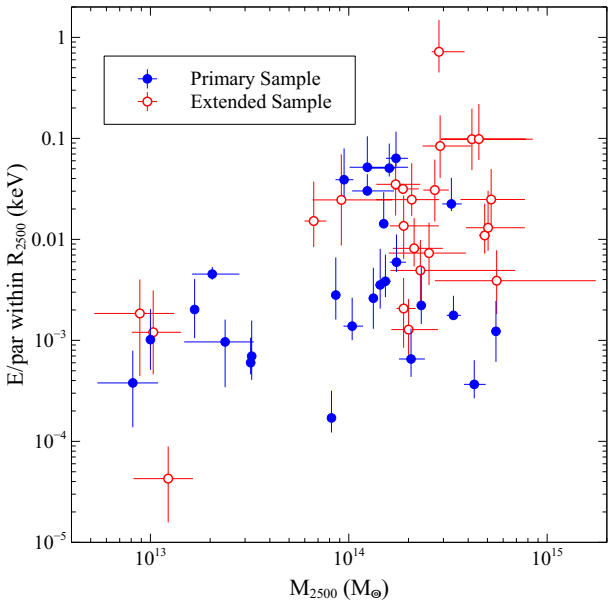

Figure 4.12: Mechanical energy per particle within R_{2500} injected from recent AGN outbursts vs. M_{2500}. This does not take into account the energy lost to radiative cooling.

We now consider the effects of cooling, which could cause a significant amount of the injected energy to be radiated away in short central cooling time systems. We plot the mechanical energy against the cooling luminosity for all of our systems in figure 4.13. The power from feedback closely matches the cooling luminosity (see also Rafferty et al. 2006, Hlavacek-Larrondo et al. 2012), so the majority of the energy from feedback is likely expended balancing radiative losses, and is not retained by the hot atmosphere. The additional energy to heat the ICM from mass-dependent feedback cycle will come from rare, powerful outbursts that greatly exceed the cooling luminosity, such as the outburst in MS0735. Since $P_{\rm mech}$ is typically greater than $L_{\rm cool}$ in less massive systems, the mechanical energy from AGN will most likely be retained by the ICM. This could well lead to a greater energy per particle from AGN in less massive systems as has been found in the full cluster population, but it is unclear without a larger sample which covers a larger range in redshift.

4.6.4 Stellar mass to halo mass relation

We further investigate how the stellar mass of BCGs relates to the halo mass in the full HIFLUGCS sample. We investigate the relationship between halo mass and $M_{*,\rm BCG}/M_{2500}$,

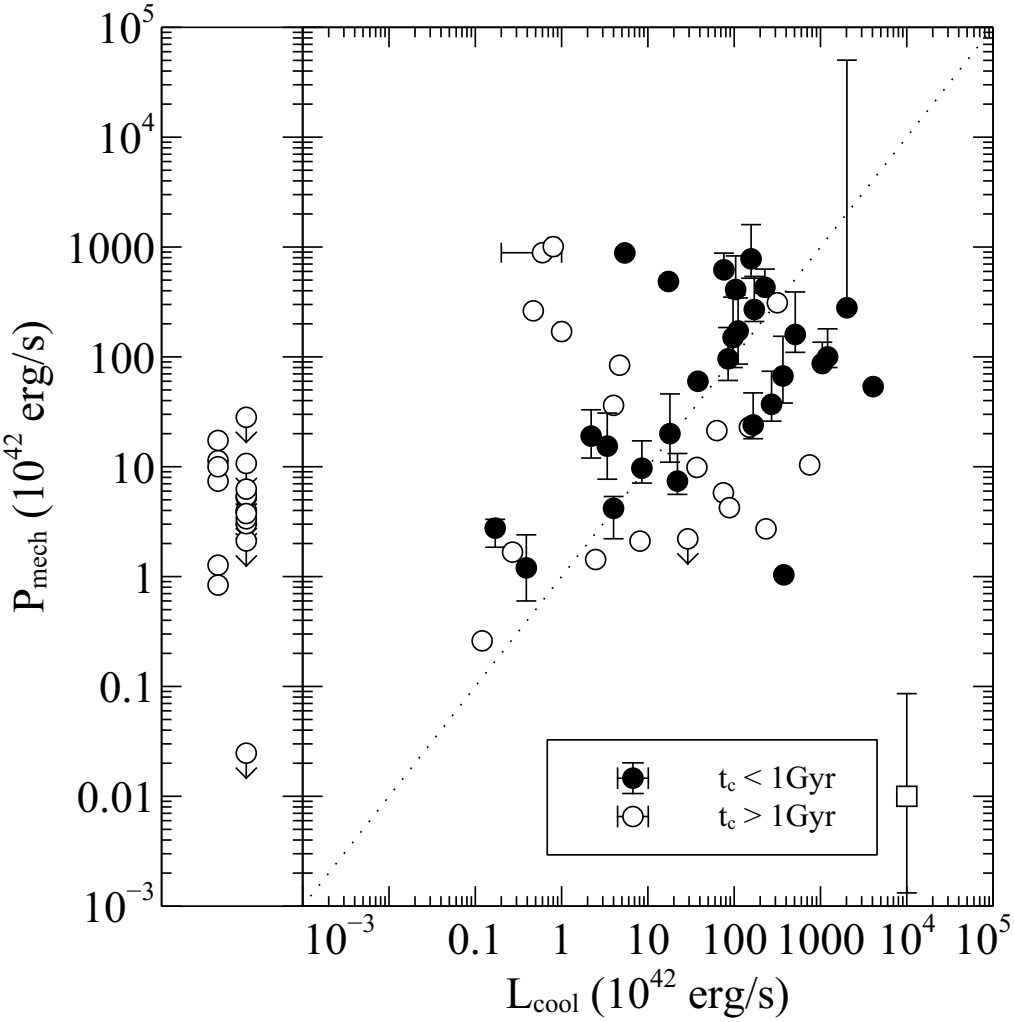

Figure 4.13: Mechanical energy from recent AGN outbursts vs. bolometric luminosity within r_{cool}. Systems are shown as either open or closed symbols based on the central cooling times from Hudson et al. (2010). The dotted line represents the line of equality. The mechanical power of systems with a cooling luminosity of zero are shown in the left column of the plot. P_{mech} values with vertical error bars are derived from X-ray cavities, which those without are estimated from the 1.4 GHz luminosity. The point in the bottom right represents the scatter in the P_{mech} - $P_{1.4GHz}$ relation.

with the sample divided by central cooling time, in Figure 4.14. $M_{*,\rm BCG}/M_{2500}$ is a measure of the integrated star formation efficiency of the BCG (Gonzalez et al., 2013). The strong downward trend in Figure 4.14 then may be interpreted as the decrease of star formation efficiency with halo mass (eg: Behroozi, Wechsler & Conroy 2013; Gonzalez et al. 2013; Kravtsov, Vikhlinin & Meshscheryakov 2014). We find that systems follow this trend independently of the central cooling time. To estimate the potential contribution of the cooling flows in these systems, we calculate the gas mass within the cooling radius. The values of $\rm r_{cool}$ represent the radius where the cooling time of the ICM is less than 7.7 Gyr, and are taken from Bîrzan et al. (2012). In systems where we do not have the full mass profile, the gas mass within $\rm r_{cool}$ is estimated assuming the gas density follows an NFW profile with $c_{500} = 3$, a typical value for halos in our mass range (Vikhlinin et al., 2006), and $\rm M_{g,2500}$ is calculated using $M_g/10^{13}M_\odot = 10^{-1.27}(M_{2500}/10^{13}M_\odot)^{1.20}$. The value $(M_{*,\rm BCG} + M_g(< r_{\rm cool}))/M_{2500}$ then gives an upper limit to the stellar mass of BCGs if the ICM is efficiently cooling, shown in the right panel of Figure 4.14. Unimpeded cooling flows could fuel enough star formation to significantly increase the stellar mass in BCGs, and provide a strong separation between systems with and without large cooling flows. Instead, the growth of stellar mass in BCGs since $z \sim 1$ seems to be dominated by mergers, with less than a factor of 2 growth in stellar mass between $z = 0.9$ and $z = 0.2$ (Lidman et al., 2012, 2013). For BCGs to lie tightly on the same trend between M_* and M_{2500} regardless of the central cooling of the BCG provides further evidence that cooling is well balanced by heating in cool-cores, preventing most of the available cooling gas from forming stars in the BCG.

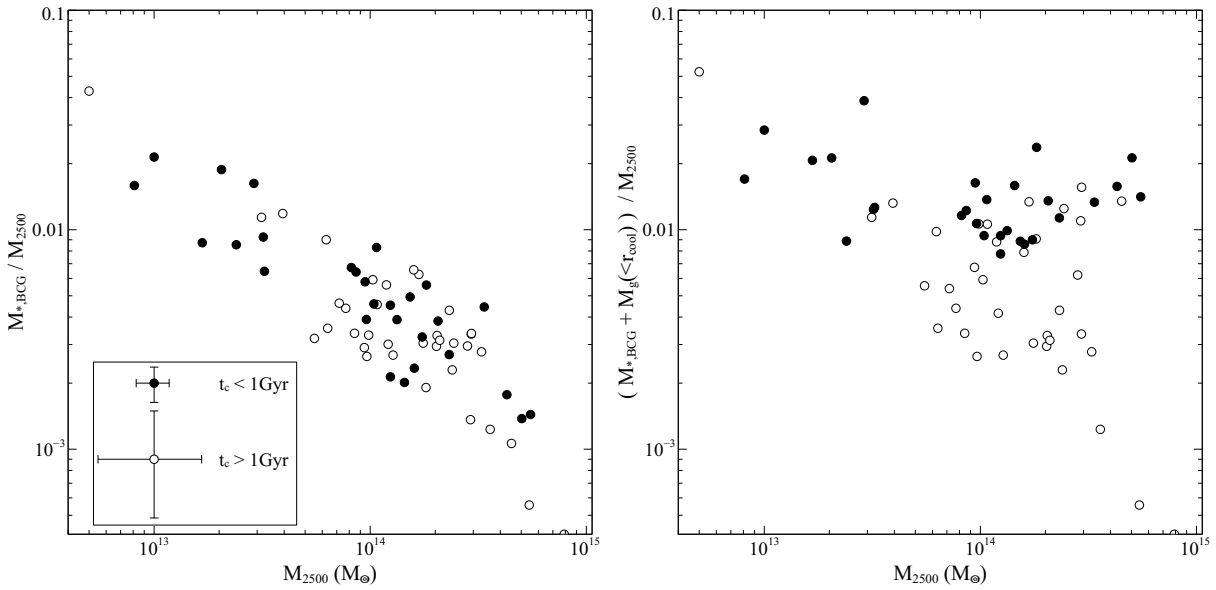

Figure 4.14: *Left:* $M_{*,BCG}/M_{2500}$ vs. M_{2500} in the full HIFLUGCS sample. *Right:* ($M_{*,BCG}$ + $M_g(< r_{cool})$)/M_{2500} vs. M_{2500}, representing the total possible stellar mass in the BCGs if cooling flows were unimpeded. Systems are shown as either open or closed symbols based on the central cooling times from Hudson et al. (2010). The average size of the error bars is shown on the bottom left.

Table 4.3: Properties of the HIFLUGCS systems

System	$M_{2500,corr}$[a] 10^{13} ($M_\odot$)	$L_{1.4GHz}$[b] (10^{32} erg s^{-1} Hz^{-1})	t_{cool}[c] (Gyr)	r_{cool}[d] (kpc)	L_{cool}[e] 10^{42} erg s^{-1}	M_K
2A0335+096	-	$1.06 \pm 0.05 \times 10^{-2}$	0.31	57	166^{+1}_{-1}	-
A85	-	$3.98 \pm 0.17 \times 10^{-2}$	0.51	116	271^{+3}_{-2}	-
A133	-	$1.8 \pm 0.1 \times 10^{-2}$	0.47	76	76^{+1}_{-1}	-
A262	-	$4.54 \pm 0.01 \times 10^{-3}$	0.43	57	$8.52^{+0.05}_{-0.06}$	-
A478	-	$6.95 \pm 0.27 \times 10^{-2}$	0.43	161	1209^{+8}_{-9}	-
A496	-	$2.96 \pm 0.11 \times 10^{-2}$	0.47	87	111^{+1}_{-1}	-
A1795	-	$8.45 \pm 0.24 \times 10^{-1}$	0.61	116	510^{+5}_{-4}	-
A2029	-	1.06 ± 0.24	0.53	127	1049^{+5}_{-5}	-
A2052	-	1.56 ± 0.028	0.51	80	97^{+1}_{-1}	-
A2199	-	$7.37 \pm 0.16 \times 10^{-1}$	0.60	106	171^{+2}_{-2}	-
A2204	-	$4.27 \pm 0.15 \times 10^{-1}$	0.25	148	2024^{+31}_{-29}	-
A2597	-	3.32 ± 0.09	0.42	119	367^{+3}_{-3}	-
A4059	-	6.82 ± 0.23	0.70	84	85^{+1}_{-1}	-
Centaurus	-	1.12 ± 0.03	0.42	87	$22.0^{+0.1}_{-0.1}$	-
Hydra A	-	30.1 ± 0.3	0.41	107	227^{+2}_{-2}	-
MKW3S	-	6.78 ± 0.001	0.86	92	104^{+1}_{-1}	-
NGC507	-	$7.15 \pm 0.35 \times 10^{-3}$	0.48	47	$2.20^{+0.03}_{-0.03}$	-
NGC1399	-	$2.91 \pm 0.01 \times 10^{-3}$	0.69	24	$0.39^{+0.01}_{-0.01}$	-
NGC1550	-	$5.47 \pm 0.53 \times 10^{-4}$	0.23	76	$3.38^{+0.04}_{-0.03}$	-
NGC4636	-	$2.82 \pm 0.03 \times 10^{-4}$	0.21	61	$0.17^{+0.002}_{-0.002}$	-
NGC5044	-	$5.95 \pm 0.50 \times 10^{-4}$	0.21	50	$4.0^{+0.02}_{-0.02}$	-
PKS1404-267	-	$7.45 \pm 0.26 \times 10^{-2}$	0.55	69	18^{+1}_{-1}	-
Sersic159/03	-	$1.92 \pm 0.2 \times 10^{-1}$	0.88	111	157^{+1}_{-1}	-
A0119	$10.3^{+3.9}_{-3.9}$	8.9×10^{-4}	14.03	-	-	-26.44 ± 0.05
A0400	$3.9^{+1.4}_{-1.4}$	$3.41 \pm 0.21 \times 10^{-1}$	8.04	22	$0.47^{+0.03}_{-0.01}$	-26.15 ± 0.05
A0399	23^{+13}_{-11}	1.84×10^{-4}	12.13	-	-	-26.97 ± 0.08
A0401	33^{+11}_{-11}	1.94×10^{-3}	8.81	-	-	-26.87 ± 0.06
A3112	$18.2^{+6.8}_{-7.5}$	1.72 ± 0.012	0.37	130	376^{+5}_{-5}	-27.00 ± 0.07
IIIZw54	$5.5^{+5.0}_{-3.2}$	$3.85 \pm 0.19 \times 10^{-3}$	5.48	30	$2.48^{+0.07}_{-0.06}$	-25.29 ± 0.08
A3158	$21.0^{+7.1}_{-7.0}$	$9.11 \pm 0.12 \times 10^{-3}$	8.22	-	-	-26.52 ± 0.10
EXO0422	$9.6^{+5.5}_{-4.4}$	$4.1 \pm 0.1 \times 10^{-2}$	0.47	64	38^{+2}_{-1}	-25.91 ± 0.05
A3266	29^{+11}_{-11}	1.46×10^{-6}	7.62	-	-	-26.96 ± 0.06
A3376	$0.5^{+2.1}_{-0.5}$	$1.91 \pm 0.06 \times 10^{-1}$	16.47	19	$1.0^{+0.1}_{-0.1}$	-25.30 ± 0.09
A3391	$15.9^{+6.0}_{-5.9}$	3.99 ± 0.49	12.46	29	$4.7^{+0.3}_{-0.2}$	-27.03 ± 0.04
A3395s	12^{+14}_{-10}	2.05 ± 0.09	12.66	22	$0.8^{+0.1}_{-0.1}$	-25.88 ± 0.07
A0576	12^{+15}_{-8}	$5.47 \pm 0.68 \times 10^{-4}$	3.62	41	$8.1^{+0.2}_{-0.2}$	-26.54 ± 0.08
A0754	54^{+19}_{-18}	1.02×10^{-3}	9.53	-	-	-25.68 ± 0.13
A1060	$9.4^{+3.2}_{-3.2}$	$3.42 \pm 0.34 \times 10^{-5}$	2.87	48	$0.120^{+0.003}_{-0003}$	-25.57 ± 0.04
A1367	$6.4^{+2.3}_{-2.3}$	1.6×10^{-4}	27.97	-	-	-25.36 ± 0.04
MKW4	$2.31^{+0.78}_{-0.78}$	$2.13 \pm 0.45 \times 10^{-4}$	0.28	47	$5.4^{+0.1}_{-0.1}$	-26.16 ± 0.03

ZwCl1215	$20.3\ ^{+9.1}_{-8.6}$	4.79×10^{-3}	10.99	-	-	-26.42 ± 0.08
A1644	$10.7\ ^{+6.8}_{-5.5}$	$4.76 \pm 0.15 \times 10^{-2}$	0.84	55	$17.3^{+0.3}_{-0.3}$	-26.85 ± 0.06
A1650	$29\ ^{+14}_{-12}$	$7.7 \pm 1.6 \times 10^{-4}$	1.25	97	234^{+3}_{-3}	-25.97 ± 0.10
A1651	$24.4\ ^{+8.4}_{-8.4}$	$1.32 \pm 0.18 \times 10^{-2}$	3.63	94	150^{+2}_{-3}	-26.65 ± 0.10
COMA	$36\ ^{+12}_{-12}$	$2.43 \pm 0.01 \times 10^{-2}$	15.97	20	$4.0^{+0.1}_{-0.1}$	-26.09 ± 0.03
A1736	$3.1\ ^{+4.7}_{-3.1}$	$2.92 \pm 0.35 \times 10^{-3}$	16.59	-	-	-25.86 ± 0.05
A3558	$16.8\ ^{+5.8}_{-5.8}$	$2.11 \pm 0.33 \times 10^{-3}$	1.69	75	75^{+2}_{-1}	-27.03 ± 0.05
A3562	$12.8\ ^{+4.2}_{-4.2}$	$2.8 \pm 0.5 \times 10^{-4}$	5.15	-	-	-25.81 ± 0.05
A3571	$28.2\ ^{+9.4}_{-9.4}$	$1.39 \pm 0.06 \times 10^{-3}$	2.13	55	88^{+1}_{-1}	-26.78 ± 0.04
MKW8	$7.2\ ^{+3.1}_{-2.7}$	$4.02 \pm 0.25 \times 10^{-4}$	10.87	19	$0.27^{+0.02}_{-0.01}$	-25.78 ± 0.04
RXJ1504	$50.3^{+5.8}_{-4.7}$	$7.74 \pm 0.27 \times 10^{-1}$	0.59	172	4080^{+49}_{-55}	-26.58 ± 0.18
A2065	$18\ ^{+42}_{-18}$	$1.20 \pm 0.22 \times 10^{-2}$	1.34	63	63^{+1}_{-1}	-25.83 ± 0.07
A2063	$9.8\ ^{+3.3}_{-3.3}$	$4.29 \pm 0.28 \times 10^{-3}$	2.36	68	37^{+1}_{-1}	-25.76 ± 0.06
A2142	$45\ ^{+17}_{-16}$	$4.60 \pm 0.071 \times 10^{-3}$	1.94	126	749^{+5}_{-5}	-26.18 ± 0.10
A2147	$8.5\ ^{+4.1}_{-3.4}$	$4.37 \pm 0.31 \times 10^{-3}$	17.04	-	-	-25.62 ± 0.04
A2163	$79\ ^{+27}_{-27}$	1.74×10^{-2}	9.65	-	-	-25.75 ± 0.25
A2244	$29\ ^{+29}_{-15}$	$4.27 \pm 0.15 \times 10^{-1}$	1.53	113	316^{+3}_{-3}	-26.97 ± 0.09
A2256	$24.0\ ^{+9.4}_{-9.2}$	1.18×10^{-3}	11.56	-	-	-26.33 ± 0.07
A2255	$17.6\ ^{+6.6}_{-6.5}$	2.34×10^{-3}	20.66	-	-	-26.30 ± 0.08
A3667	$20.4\ ^{+7.2}_{-7.2}$	1.29×10^{-3}	6.14	-	-	-26.55 ± 0.05
A2589	$10.8\ ^{+9.2}_{-5.6}$	5.83×10^{-4}	1.18	62	29^{+1}_{-1}	-26.21 ± 0.06
A2634	$6.3\ ^{+2.8}_{-2.7}$	1.73 ± 0.086	1.52	17	$0.6^{+0.4}_{-0.4}$	-26.35 ± 0.03
A2657	$9.7\ ^{+3.4}_{-3.4}$	5.49×10^{-4}	2.68	-	-	-25.50 ± 0.10
A4038	$7.7\ ^{+2.6}_{-2.5}$	$5.19 \pm 0.08 \times 10^{-3}$	1.68	-	-	-25.80 ± 0.06

Notes: [a]M_{2500} values derived from Reiprich & Böhringer (2002) with the correction factor 0f 1.18 and additional error of 0.33 dex applied. [b]1.4 GHz luminosity of central radio sources from Mittal et al. (2009); Bîrzan et al. (2012). Values without error bars are upper limits derived from the noise in NVSS images form Bîrzan et al. (2012). [c]Cooling time at $r = 0.004R_{500}$, from Hudson et al. (2010). [d]The cooling radius from Bîrzan et al. (2012), which is the radius within which the cooling time of the ICM is less than 7.7 Gyr. [e]The bolometric luminosity within R_{cool} from Bîrzan et al. (2012).

4.7 Preliminary results - Missing baryons

With the effects of shock heating and gravitational infall included, the ICM is expected to form self-similarly to the dark matter distribution (Navarro, Frenk & White, 1995). The gas fraction in clusters should then be a constant function of halo mass, and should be near the cosmic baryon fraction given that stellar mass contains only a small amount of the baryonic mass in clusters. Measured gas fractions in galaxy clusters are usually significantly below the cosmic baryon fraction when measured at R_{2500}, and tend to decrease towards the centres of galaxies (Allen et al. 2004, 2008; Vikhlinin et al. 2006, see figure 4.15). Gas fractions are usually close to the cosmic value when measured in the regions near R_{500}, and higher in clusters outskirts where the effects of gas clumping and non-thermal pressure are important (Vikhlinin et al., 2006; Simionescu et al., 2011). Gas fractions are lower in poor clusters and groups (Sun et al., 2009; Gonzalez et al., 2013), and it has been suggested that AGN could be the cause of the lower observed gas fractions by driving gas into cluster outskirts (Puchwein, Sijacki & Springel, 2008; Giodini et al., 2010). In this section we aim to answer if mechanical outbursts are energetically capable of unbinding sufficient gas to lower the gas fractions to the observed values.

Under the assumption that the low gas fractions are caused by gas being expelled into cluster outskirts, we can construct profiles of the "missing gas mass" through the difference between our gas fraction profiles and the cosmic baryon fraction. The energy required to move this gas into the cluster outskirts (taken as beyond R_{500}) can be calculated as:

$$E_{\rm bind} = 4\pi \int_0^{R_{2500}} [\phi(r) - \phi(R_{500})]\rho_g(r) r^2 dr. \tag{4.5}$$

For simplicity, we refer to this as the binding energy throughout this section. We calculate the binding energy for all of our systems with mass profiles that reach R_{2500}. As we have not accounted for the mass in stars, this is an overestimate of the energy required to recreate the baryon fraction profiles in clusters.

We plot the binding energy of the missing gas against cavity energies of our systems in Figure 4.15. The largest outburst in our sample contributes $\sim 6\%$ of the required energy to displace the missing gas, while the majority of outbursts in our systems are $2-3$ orders of magnitude lower than the binding energy.

We use the values of Ma, McNamara & Nulsen (2013) to estimate the total energy from AGN since z=2, taking this as the time when BCGs were formed (eg: van Dokkum & Franx 2001). They measure the average AGN power out to z=0.6 in a sample with 685 clusters split into 4 luminosity bins, using central radio sources from NVSS and the scaling

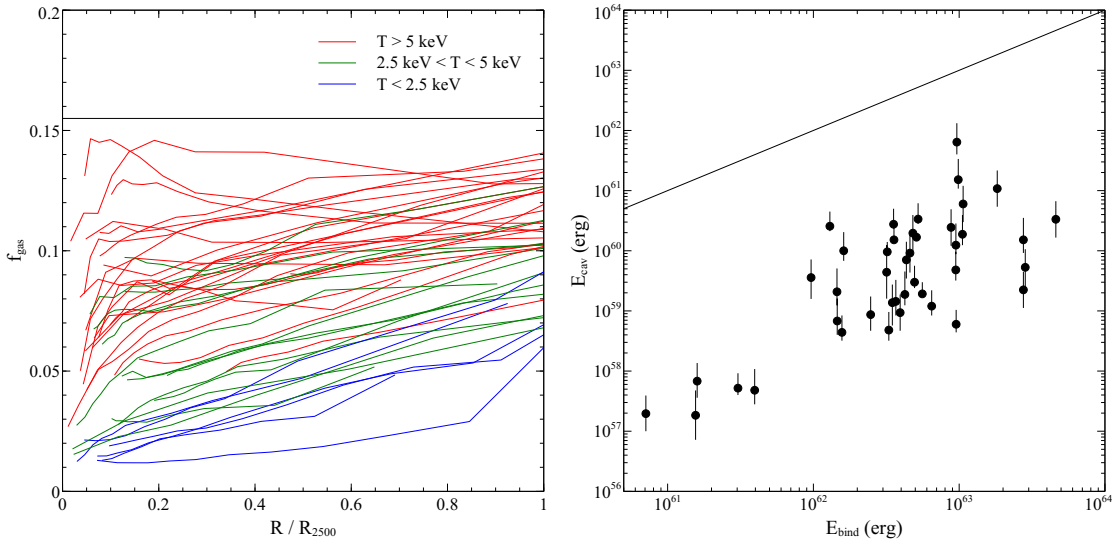

Figure 4.15: *Left:* Gas fraction profiles of all systems, sorted by the core-excised temperature. The horizontal line is the Planck value of the cosmic baryon fraction. *Right:* Binding energy of the missing gas vs. AGN mechanical energy estimated from X-ray cavities. The solid line is the line of equality. The errors on the binding energies have not yet been calculated.

relation between mechanical power and 1.4 GHz luminosity of Cavagnolo et al. (2010). Extrapolating to z=2 gives a conservative lower limit on the mechanical energy output, as AGN are more active in the past. We plot the binding energy of the missing gas against the total cluster luminosity along with the total AGN energy from Ma, McNamara & Nulsen (2013) in figure 4.16.

Mechanical AGN are energetically sufficient in low mass systems to reproduce the observed gas fraction profiles, provided the AGN can efficiently transfer kinetic energy to the ICM. This is bolstered by the fact that it would have been easier to unbind the same amount of gas at earlier times, as clusters will have been less massive. The ratio of AGN power to binding energy is lower in high mass systems due to the weak dependence of mechanical power with halo mass in the full cluster population. It is difficult to make conclusions for the high mass systems, as the binding energies are overestimated, AGN powers are underestimated, and the missing gas will have been easier to unbind at higher redshift. Gas fractions are below the cosmic value out to z=0.543, the highest redshift in our sample, and gas fractions at R_{2500} have been found to be constant with redshift beyond $z = 1$ in our cosmology (Allen et al., 2008). The observed gas fraction profiles are

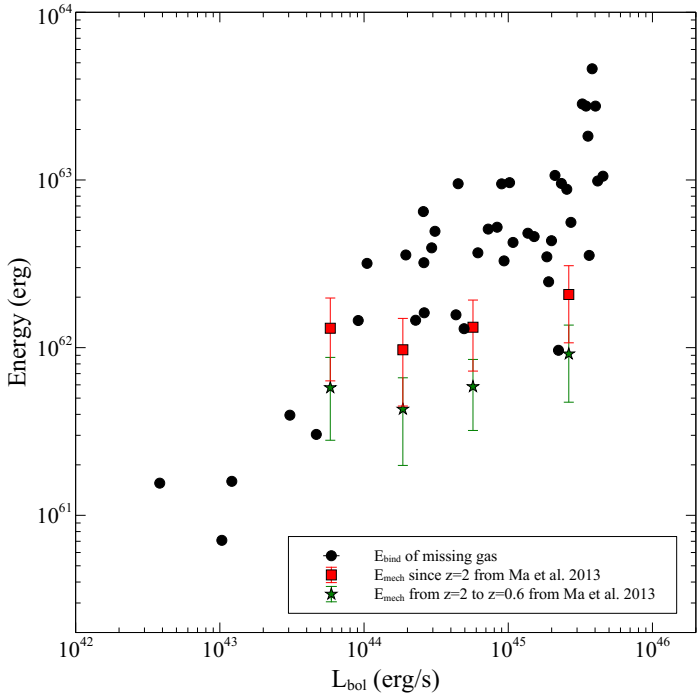

Figure 4.16: Energy vs. bolometric luminosity (core included). The black points are individual clusters, and the y values are the current binding energies of the missing gas, which are an overestimate of the energy required to reproduce the observed gas fractions. The red points are the total energy from radio-AGN estimated by extrapolating the jet powers of Ma, McNamara & Nulsen (2013) to z=2. The green points are the total energy from radio-AGN between z=2 and z=0.6, estimated the same way. The errors on the binding energies have not yet been calculated.

likely then shaped by processes at high redshifts. This could be by unbinding gas through powerful radio-AGN or quasar activity, or by the addition of heat which causes the ICM to be more spatially extended than the dark matter distribution.

Chapter 5

Conclusions

5.1 Summary

We have investigated the relationship between AGN feedback and large scale properties of galaxy clusters at $z < 0.55$. In the full HIFLUGCS sample, we find that the power output from AGN is strongly coupled to total cluster mass in systems with central cooling times shorter than 1 Gyr, with no evidence for a correlation in systems with central cooling times greater than 1 Gyr. This provides additional evidence that ICM cooling in the centres of galaxy clusters is providing the causal link between AGN and their host systems. Additionally, we find that the fraction of mass in stars in BCGs strongly decreases with total halo mass, with no separation based on the central cooling time. Unimpeded cooling flows could significantly alter this relation, suggesting that the cooling of the ICM is well balanced by heating over long timescales, such that only a small amount of the available gas is able to form stars.

Using the subset of HIFLUGCS with X-ray cavities and $t_{\rm c,central} < 1$ Gyr, we investigate the scaling relationships between cavity power and cluster properties. The relationship between cavity power and luminosity is found to be $P_{\rm cav} \propto L_{\rm bol}^{0.93\pm0.23}$, consistent with linear scaling. Cavity power then scales with the other cluster properties equivalently to the bolometric X-ray luminosity, but with much larger scatter. We find no significant difference in the scatter between halo mass, gas mass, and BCG stellar mass with $\rm P_{cav}$. We find a relation between cavity power and halo mass of $P_{\rm cav} \propto M_{2500}^{1.55\pm0.26}$, and a relation between total cavity energy and mass as $E_{\rm cav} \propto M_{2500}^{2.04\pm0.30}$. Our scaling of $\rm E_{cav}$ with mass is steeper than analytic scalings of $E_{\rm cav} \propto M^{4/3}$ or $E_{\rm cav} \propto M^{5/3}$ which have been used in simulations. We find a weak positive trend between accretion efficiency and mass in our

sample, which may help explain the steep slope of our E_{cav}-M_{2500} relation, but this may also be explained as a systematic underestimate of our black hole masses.

We investigated the effect of AGN feedback on cluster scaling relations. We find core excised L-T and M-T relations in our subset of cavity systems in HIFLUGCS with short central cooling times consistent with the cluster population as a whole. These results seem to imply that radio-mode feedback is not greatly affecting cluster-scale properties beyond the cooling radius. However, this interpretation is complicated by the fact that we are only able to observe very recent AGN activity. It could be that a history of AGN heating is present in almost all galaxy clusters, including systems without cool cores. We find that $\sim 30\%$ of systems with $t_{c,central} > 1$ Gyr in HIFLUGCS have radio outbursts of comparable power to the systems with $t_{c,central} < 1$ Gyr. The AGN power in the short cooling time systems follows the cooling luminosity of the ICM, so much of the energy output from a feedback loop is used to balance radiative losses. Additional energy which can heat the ICM is then dominated by rare powerful outbursts which greatly exceed the cooling luminosity of the ICM, such as the outburst in MS0735. The weak dependence of mechanical AGN power with mass in long cooling time systems implies that AGN heating will be more significant in low mass systems. This is roughly consistent with previous studies which find scaling relations to be further from self-similar in groups and poor clusters than in massive clusters.

5.2 Future Work

There are interesting topics to be explored to continue this work, which we briefly discuss here.

A similar study could be extended to a larger, representative sample. Detailed analysis of the full cluster population will allow for a more self-contained comparison of the cluster scaling relations, and the relative effects of AGN heating in cool-core and non cool-core clusters. A larger sample will enable more accurate determinations of the P_{cav} relations measured in this study, and may make it possible to study the evolution of these relations. Additionally, the addition of more low-mass systems will be necessary to study the form of the P_{cav} relations, and see if they follow a powerlaw at low masses. Developing an automated algorithm to detect X-ray cavities would be extremely useful for studies of this kind. This would remove subjective biases from cavity measurement and detection, allow the formal significance to be quantified, and allow for accurate error bars on mechanical AGN power to be calculated.

A more accurate tracer of mechanical power from AGN would also be useful to incorporate into a new study. Low-frequency radio emission is more tightly correlated to AGN power than the 1.4 GHz emission used in this study, and additional wavebands can be used to further constrain the AGN power (Bîrzan et al., 2008). This would allow for a more detailed measurement of the $P_{\rm mech} - M$ relation in long and short cooling time systems, as studied in section 4.6.2. In a large enough sample, the integrated energy per particle from AGN could be calculated in several mass bins in both cool-core and non cool-core systems, and tied directly to the scaling relations and cooling luminosities in those samples.

Mechanical feedback has been primarily studied at low redshifts due to the limitations of X-ray imaging, while AGN are known to be more active in the past (Smolčić et al., 2009). For measuring the total contribution of AGN over cluster timescales, another approach is needed. One possible project would be to measure the central radio sources in high-redshift cluster samples selected by the Sunyaev Zel'dovich signal (Sunyaev & Zeldovich, 1972). A possible sample is the high-redshift cluster sample constructed form South Pole Telescope observations (McDonald et al., 2013). It will then be possible to estimate the total contribution from radio-AGN over cluster timescales without much extrapolation, and measure the evolution of radio-AGN in clusters.

One use of our results is that the measured relationship between $\rm P_{mech}$ and cluster mass could be used as the prescription for feedback in simulations. The simulation results of cluster scaling relations, entropy profiles, and the truncation of BCG stellar masses could be compared to observations.

The upcoming Astro-H telescope will test the validity of the hydrostatic equilibrium assumption in cluster mass measurements. The high spectral resolution of Astro-H will enable measurements of the bulk and turbulent motions in the ICM to better than 100 km/s, which will produce the first observational measurements of the non-thermal pressure support in the ICM. Astro-H should be able to map the non-thermal pressure profile out to $\rm R_{2500}$ in several nearby relaxed clusters, and will quantify the extent to which cluster masses are underestimated. Multiple temperature components in the ICM will also be easier to detect outside of bright cluster cores, which can bias mass measurements low when spectra are fit with a one-temperature model.

References

Akritas M. G., Bershady M. A., 1996, ApJ, 470, 706

Allen S. W., Dunn R. J. H., Fabian A. C., Taylor G. B., Reynolds C. S., 2006, MNRAS, 372, 21

Allen S. W., Rapetti D. A., Schmidt R. W., Ebeling H., Morris R. G., Fabian A. C., 2008, MNRAS, 383, 879

Allen S. W., Schmidt R. W., Ebeling H., Fabian A. C., van Speybroeck L., 2004, MNRAS, 353, 457

Anders E., Grevesse N., 1989, Geochim. Cosmochim. Acta, 53, 197

Arnaud K. A., 1996, in Astronomical Society of the Pacific Conference Series, Vol. 101, Astronomical Data Analysis Software and Systems V, Jacoby G. H., Barnes J., eds., p. 17

Arnaud M., Pointecouteau E., Pratt G. W., 2005, A&A, 441, 893

Bahcall J. N., Sarazin C. L., 1977, ApJ, 213, L99

Behroozi P. S., Wechsler R. H., Conroy C., 2013, ApJ, 762, L31

Bell E. F., de Jong R. S., 2001, ApJ, 550, 212

Bernardi M., Meert A., Sheth R. K., Vikram V., Huertas-Company M., Mei S., Shankar F., 2013, MNRAS, 436, 697

Best P. N., von der Linden A., Kauffmann G., Heckman T. M., Kaiser C. R., 2007, MNRAS, 379, 894

Bîrzan L., McNamara B. R., Nulsen P. E. J., Carilli C. L., Wise M. W., 2008, ApJ, 686, 859

Bîrzan L., Rafferty D. A., McNamara B. R., Wise M. W., Nulsen P. E. J., 2004, ApJ, 607, 800

Bîrzan L., Rafferty D. A., Nulsen P. E. J., McNamara B. R., Röttgering H. J. A., Wise M. W., Mittal R., 2012, MNRAS, 427, 3468

Blanton E. L., Randall S. W., Clarke T. E., Sarazin C. L., McNamara B. R., Douglass E. M., McDonald M., 2011, ApJ, 737, 99

Bower R. G., Benson A. J., Malbon R., Helly J. C., Frenk C. S., Baugh C. M., Cole S., Lacey C. G., 2006, MNRAS, 370, 645

Cavagnolo K. W., McNamara B. R., Nulsen P. E. J., Carilli C. L., Jones C., Bîrzan L., 2010, ApJ, 720, 1066

Churazov E., Brüggen M., Kaiser C. R., Böhringer H., Forman W., 2001, ApJ, 554, 261

Conroy C., van Dokkum P., Kravtsov A., 2014, ArXiv e-prints

Croton D. J. et al., 2006, MNRAS, 365, 11

De Grandi S., Molendi S., 2001, ApJ, 551, 153

Dekel A., Birnboim Y., 2006, MNRAS, 368, 2

Dong R., Rasmussen J., Mulchaey J. S., 2010, ApJ, 712, 883

Dunn R. J. H., Fabian A. C., 2006, MNRAS, 373, 959

Dunn R. J. H., Fabian A. C., Taylor G. B., 2005, MNRAS, 364, 1343

Ebeling H., Edge A. C., Henry J. P., 2001, ApJ, 553, 668

Edge A. C., 2001, MNRAS, 328, 762

Evrard A. E., Henry J. P., 1991, ApJ, 383, 95

Fabian A. C., 1994, ARA&A, 32, 277

Fabian A. C., 2012, ARA&A, 50, 455

Fabian A. C., Sanders J. S., Taylor G. B., Allen S. W., Crawford C. S., Johnstone R. M., Iwasawa K., 2006, MNRAS, 366, 417

Fabricant D., Lecar M., Gorenstein P., 1980, Highlights of Astronomy, 5, 689

Ferrarese L., Merritt D., 2000, ApJ, 539, L9

Forman W. et al., 2007, ApJ, 665, 1057

Forman W. et al., 2005, ApJ, 635, 894

Foster A. R., Ji L., Smith R. K., Brickhouse N. S., 2012, ApJ, 756, 128

Freeman P. E., Kashyap V., Rosner R., Lamb D. Q., 2002, ApJS, 138, 185

Gaspari M., Brighenti F., Temi P., Ettori S., 2014, ApJ, 783, L10

Gebhardt K. et al., 2000, ApJ, 539, L13

Giacconi R., Murray S., Gursky H., Kellogg E., Schreier E., Tananbaum H., 1972, ApJ, 178, 281

Giodini S., Lovisari L., Pointecouteau E., Ettori S., Reiprich T. H., Hoekstra H., 2013, Space Sci. Rev., 177, 247

Giodini S. et al., 2010, ApJ, 714, 218

Gitti M., McNamara B. R., Nulsen P. E. J., Wise M. W., 2007, ApJ, 660, 1118

Gonzalez A. H., Sivanandam S., Zabludoff A. I., Zaritsky D., 2013, ApJ, 778, 14

Graham A. W., 2007, MNRAS, 379, 711

Gursky H., Schwartz D. A., 1977, ARA&A, 15, 541

Hardcastle M. J., Evans D. A., Croston J. H., 2007, MNRAS, 376, 1849

Hlavacek-Larrondo J. et al., 2013, ApJ, 777, 163

Hlavacek-Larrondo J., Fabian A. C., Edge A. C., Ebeling H., Sanders J. S., Hogan M. T., Taylor G. B., 2012, MNRAS, 421, 1360

Hubble E. P., 1926, ApJ, 64, 321

Hudson D. S., Mittal R., Reiprich T. H., Nulsen P. E. J., Andernach H., Sarazin C. L., 2010, A&A, 513, A37

Kaiser N., 1986, MNRAS, 222, 323

Kaiser N., 1991, ApJ, 383, 104

Kalberla P. M. W., Burton W. B., Hartmann D., Arnal E. M., Bajaja E., Morras R., Pöppel W. G. L., 2005, A&A, 440, 775

Kirkpatrick C. C., McNamara B. R., Cavagnolo K. W., 2011, ApJ, 731, L23

Kravtsov A., Vikhlinin A., Meshscheryakov A., 2014, ArXiv e-prints

Kriss G. A., Cioffi D. F., Canizares C. R., 1983, ApJ, 272, 439

Lauer T. R. et al., 2007, ApJ, 662, 808

Lidman C. et al., 2013, MNRAS, 433, 825

Lidman C. et al., 2012, MNRAS, 427, 550

Lin Y.-T., Mohr J. J., Stanford S. A., 2003, ApJ, 591, 749

Ma C.-J., McNamara B. R., Nulsen P. E. J., 2013, ApJ, 763, 63

Mahdavi A., Hoekstra H., Babul A., Bildfell C., Jeltema T., Henry J. P., 2013, ApJ, 767, 116

Mahdavi A., Hoekstra H., Babul A., Henry J. P., 2008, MNRAS, 384, 1567

Markevitch M., 1998, ApJ, 504, 27

Maughan B. J. et al., 2008, MNRAS, 387, 998

McCarthy I. G. et al., 2010, MNRAS, 406, 822

McConnell N. J., Ma C.-P., 2013, ApJ, 764, 184

McDonald M. et al., 2013, ApJ, 774, 23

McNamara B. R., Nulsen P. E. J., 2007, ARA&A, 45, 117

McNamara B. R., Nulsen P. E. J., 2012, New Journal of Physics, 14, 055023

McNamara B. R. et al., 2014, ArXiv e-prints

McNamara B. R. et al., 2000, ApJ, 534, L135

Mendygral P. J., Jones T. W., Dolag K., 2012, ApJ, 750, 166

Million E. T., Werner N., Simionescu A., Allen S. W., Nulsen P. E. J., Fabian A. C., Böhringer H., Sanders J. S., 2010, MNRAS, 407, 2046

Mitchell R. J., Culhane J. L., Davison P. J. N., Ives J. C., 1976, MNRAS, 175, 29P

Mittal R., Hudson D. S., Reiprich T. H., Clarke T., 2009, A&A, 501, 835

Nagai D., Kravtsov A. V., Vikhlinin A., 2007, ApJ, 668, 1

Navarro J. F., Frenk C. S., White S. D. M., 1995, MNRAS, 275, 720

Navarro J. F., Frenk C. S., White S. D. M., 1997, ApJ, 490, 493

Nelson K., Lau E. T., Nagai D., 2014, ArXiv e-prints

Nulsen P., Jones C., Forman W., Churazov E., McNamara B., David L., Murray S., 2009, in American Institute of Physics Conference Series, Vol. 1201, American Institute of Physics Conference Series, Heinz S., Wilcots E., eds., pp. 198–201

Nulsen P. E. J., Hambrick D. C., McNamara B. R., Rafferty D., Birzan L., Wise M. W., David L. P., 2005, ApJ, 625, L9

Nulsen P. E. J., Powell S. L., Vikhlinin A., 2010, ApJ, 722, 55

O'Sullivan E., Giacintucci S., David L. P., Gitti M., Vrtilek J. M., Raychaudhury S., Ponman T. J., 2011, ApJ, 735, 11

Panagoulia E. K., Fabian A. C., Sanders J. S., 2014, MNRAS, 438, 2341

Paturel G., Petit C., Prugniel P., Theureau G., Rousseau J., Brouty M., Dubois P., Cambrésy L., 2003, A&A, 412, 45

Peterson J. R., Fabian A. C., 2006, Phys. Rep., 427, 1

Poggianti B. M., 1997, A&AS, 122, 399

Pointecouteau E., Arnaud M., Pratt G. W., 2005, A&A, 435, 1

Pratt G. W., Croston J. H., Arnaud M., Böhringer H., 2009, A&A, 498, 361

Puchwein E., Sijacki D., Springel V., 2008, ApJ, 687, L53

Rafferty D. A., McNamara B. R., Nulsen P. E. J., 2008, ApJ, 687, 899

Rafferty D. A., McNamara B. R., Nulsen P. E. J., Wise M. W., 2006, ApJ, 652, 216

Randall S. W. et al., 2011, ApJ, 726, 86

Reiprich T. H., Böhringer H., 2002, ApJ, 567, 716

Russell H. R., McNamara B. R., Edge A. C., Hogan M. T., Main R. A., Vantyghem A. N., 2013, MNRAS, 432, 530

Russell H. R. et al., 2014, ApJ, 784, 78

Russell H. R., Sanders J. S., Fabian A. C., 2008, MNRAS, 390, 1207

Rybicki G. B., Lightman A. P., 2008, Radiative processes in astrophysics. John Wiley & Sons

Salomé P., Combes F., 2003, A&A, 412, 657

Sanders J. S., Fabian A. C., Allen S. W., Schmidt R. W., 2004, MNRAS, 349, 952

Sanders J. S., Fabian A. C., Taylor G. B., 2009, MNRAS, 393, 71

Sarazin C. L., 1988, Cambridge Astrophysics Series, Cambridge: Cambridge University Press, 1988, 1

Schlegel D. J., Finkbeiner D. P., Davis M., 1998, ApJ, 500, 525

Schmidt R. W., Allen S. W., 2007, MNRAS, 379, 209

Serlemitsos P. J., Smith B. W., Boldt E. A., Holt S. S., Swank J. H., 1977, ApJ, 211, L63

Short C. J., Thomas P. A., Young O. E., Pearce F. R., Jenkins A., Muanwong O., 2010, MNRAS, 408, 2213

Shurkin K., Dunn R. J. H., Gentile G., Taylor G. B., Allen S. W., 2008, MNRAS, 383, 923

Sijacki D., Springel V., 2006, MNRAS, 366, 397

Simionescu A. et al., 2011, Science, 331, 1576

Simionescu A., Werner N., Finoguenov A., Böhringer H., Brüggen M., 2008, A&A, 482, 97

Skrutskie M. F. et al., 2006, AJ, 131, 1163

Smith S., 1936, ApJ, 83, 23

Smolčić V. et al., 2009, ApJ, 696, 24

Sun M., Voit G. M., Donahue M., Jones C., Forman W., Vikhlinin A., 2009, ApJ, 693, 1142

Sunyaev R. A., Zeldovich Y. B., 1972, Comments on Astrophysics and Space Physics, 4, 173

Takahashi T. et al., 2012, in Society of Photo-Optical Instrumentation Engineers (SPIE) Conference Series, Vol. 8443, Society of Photo-Optical Instrumentation Engineers (SPIE) Conference Series

van Dokkum P. G., Franx M., 2001, ApJ, 553, 90

Vantyghem A. N., McNamara B. R., Russell H. R., Main R. A., Nulsen P. E. J., Wise M. W., Hoekstra H., Gitti M., 2014, MNRAS, 442, 3192

Vikhlinin A. et al., 2009, ApJ, 692, 1033

Vikhlinin A., Kravtsov A., Forman W., Jones C., Markevitch M., Murray S. S., Van Speybroeck L., 2006, ApJ, 640, 691

Vikhlinin A., Markevitch M., Murray S. S., Jones C., Forman W., Van Speybroeck L., 2005, ApJ, 628, 655

Voigt L. M., Fabian A. C., 2004, MNRAS, 347, 1130

Werner N. et al., 2010, MNRAS, 407, 2063

Wu K. K. S., Fabian A. C., Nulsen P. E. J., 2000, MNRAS, 318, 889

Zwicky F., 1933, Helvetica Physica Acta, 6, 110

Zwicky F., 1937, ApJ, 86, 217

APPENDICES

Appendix A

Mass Profiles

Here we present our mass profiles for all systems in our sample:

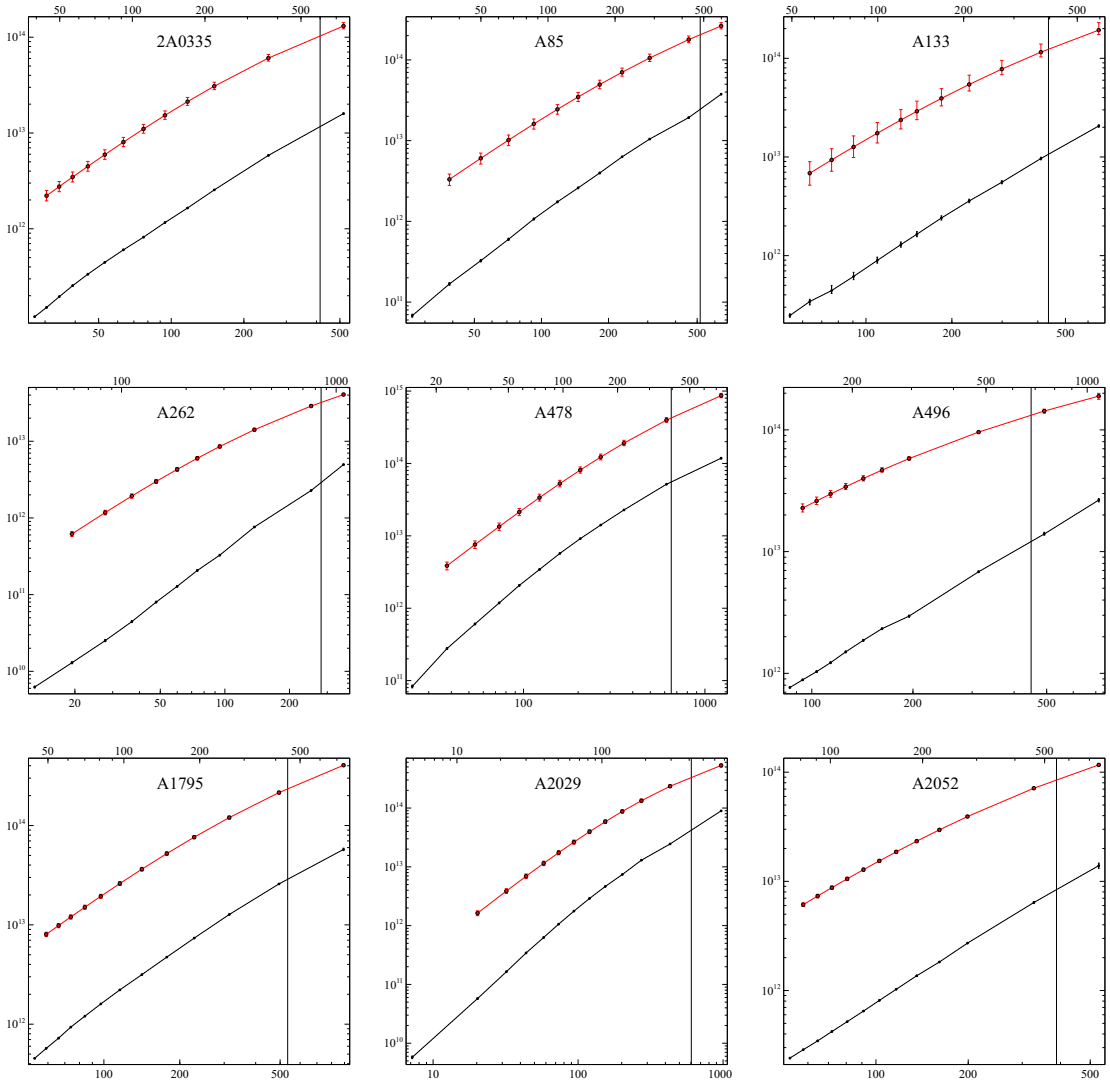

Figure A.1: Mass profiles. The y axis gives the enclosed mass in $M_{\odot}$, the lower x-axis gives the radius from the cluster centre in kpc, and the upper x-axis gives the radius from the cluster centre in arcseconds. The red curve denotes the total mass profile, and the dashed black curve is the gas mass profile. The solid vertical line denotes R_{2500}. Note that the error bars in each profile are correlated.

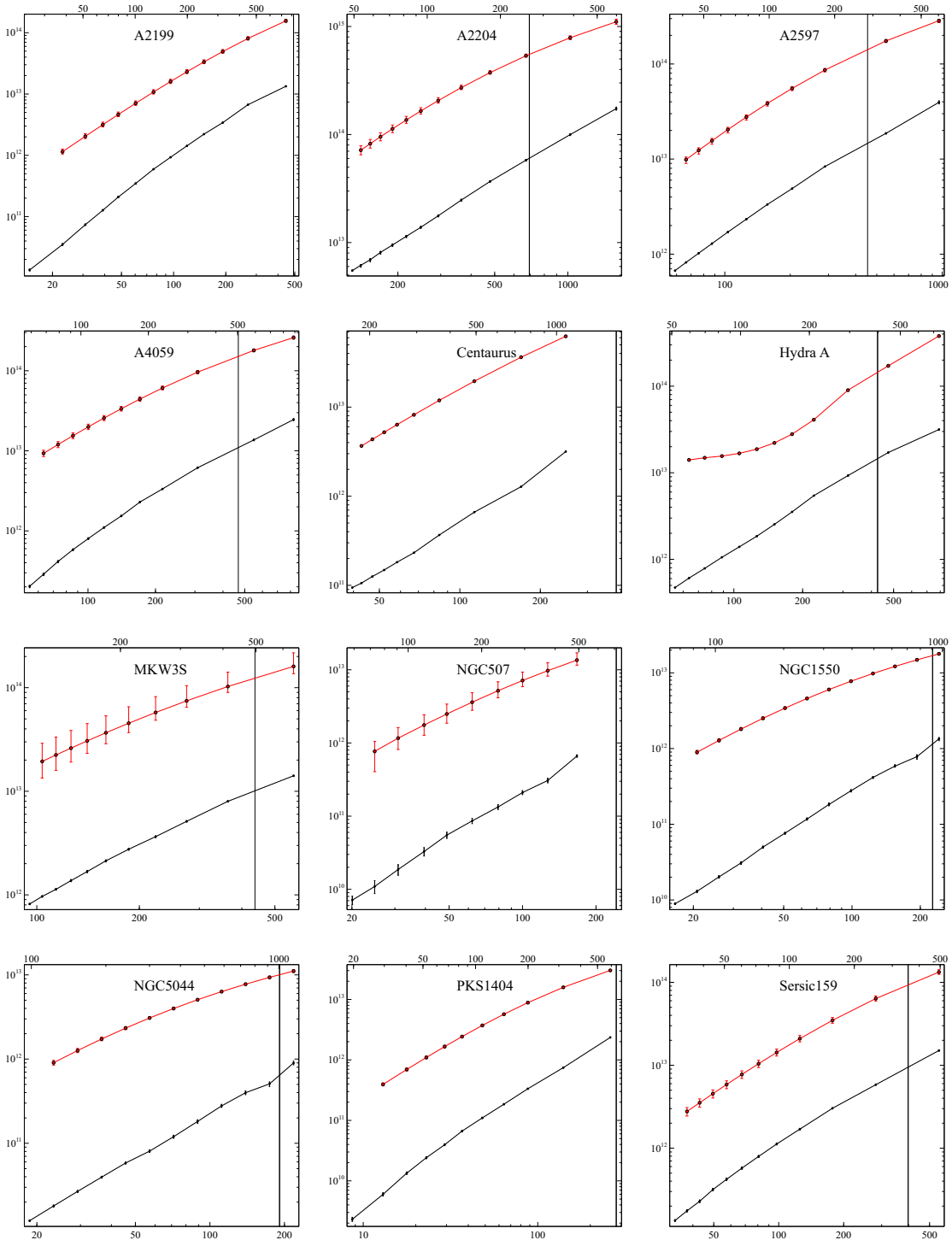
A2199
A2204
A2597
A4059
Centaurus
Hydra A
MKW3S
NGC507
NGC1550
NGC5044
PKS1404
Sersic159

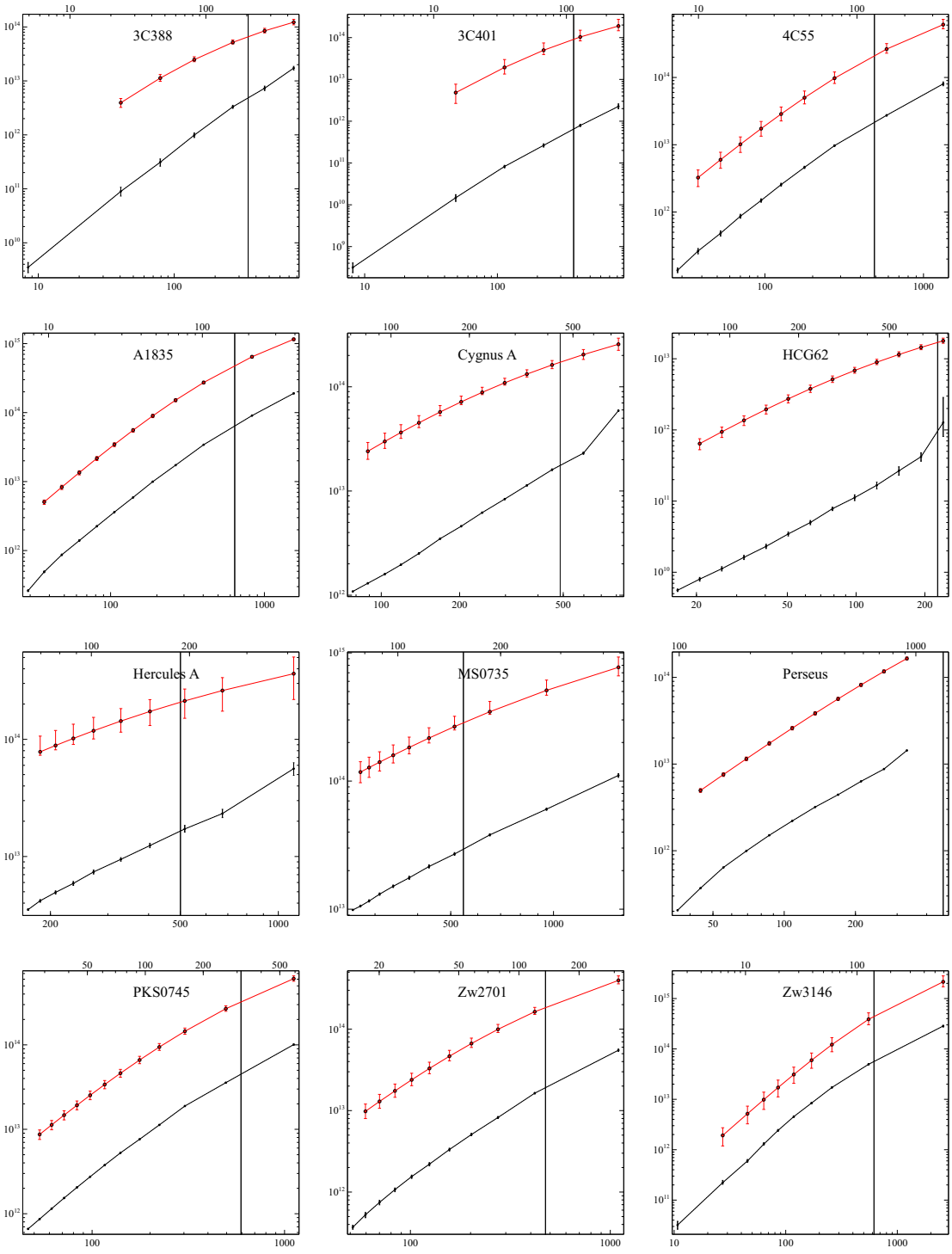
3C388
3C401
4C55
A1835
Cygnus A
HCG62
Hercules A
MS0735
Perseus
PKS0745
Zw2701
Zw3146

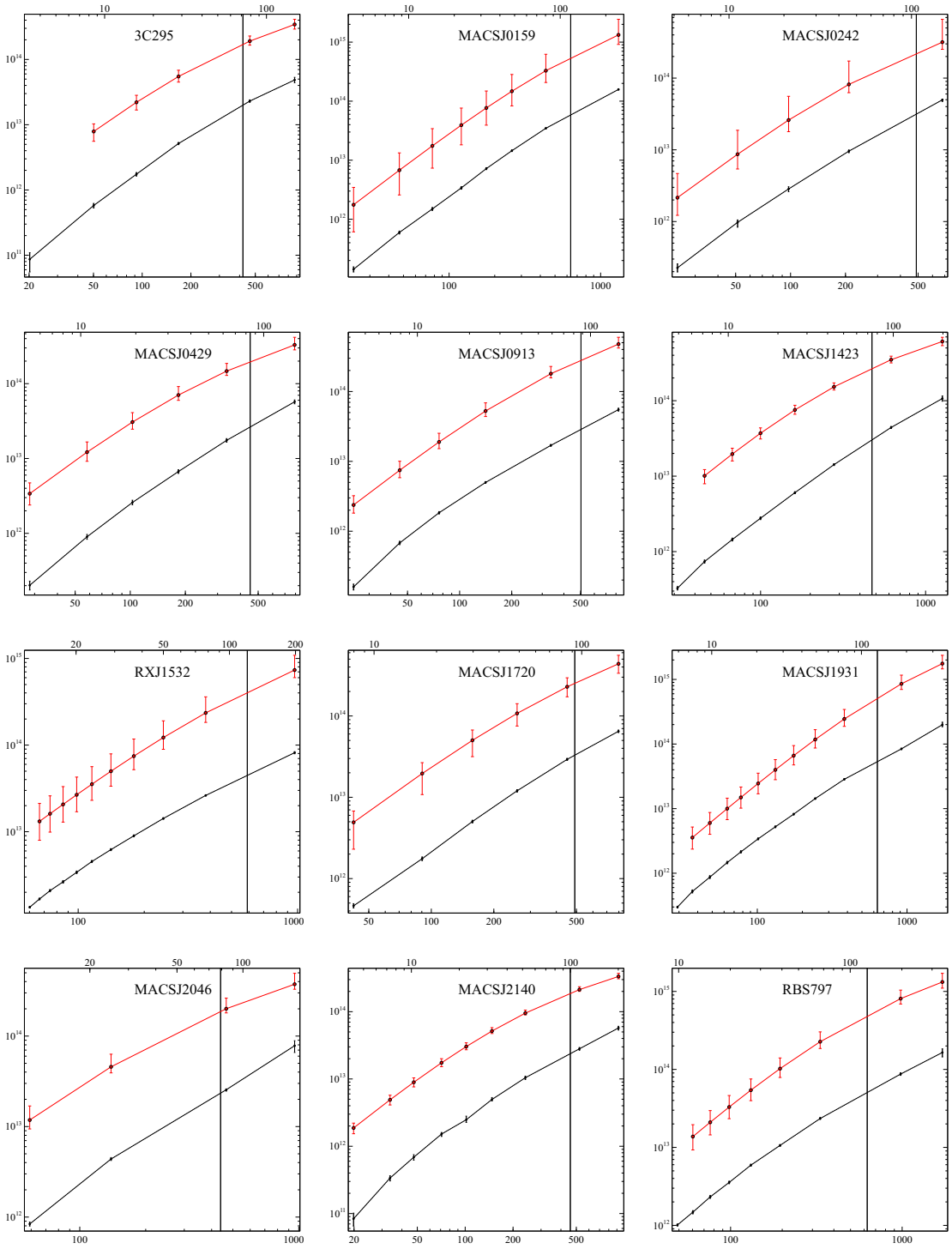
3C295
MACSJ0159
MACSJ0242
MACSJ0429
MACSJ0913
MACSJ1423
RXJ1532
MACSJ1720
MACSJ1931
MACSJ2046
MACSJ2140
RBS797

Table A.1: Derived Mass Profiles

ρ_o is given in units of $M_\odot/\mathrm{kpc}^3$, R_s is given in units of kpc

2A0335	r (kpc)	27.2	30.4	34.3	39.0	45.1	53.1	63.4	76.8	94.2	117	151	253	518
$\rho_o=2.21^{+0.19}_{-0.15}\times10^6$	M_g (10^{12} $M_\odot$)	$0.121^{+0.001}_{-0.001}$	$0.151^{+0.002}_{-0.002}$	$0.195^{+0.003}_{-0.003}$	$0.255^{+0.004}_{-0.004}$	$0.336^{+0.005}_{-0.005}$	$0.447^{+0.006}_{-0.006}$	$0.603^{+0.008}_{-0.008}$	$0.818^{+0.01}_{-0.01}$	$1.16^{+0.01}_{-0.01}$	$1.65^{+0.02}_{-0.02}$	$2.55^{+0.02}_{-0.02}$	$5.83^{+0.05}_{-0.05}$	$15.9^{+0.21}_{-0.21}$
$R_s=2.04^{+0.28}_{-0.22}\times10^2$	M (10^{13} $M_\odot$)	-	$0.221^{+0.03}_{-0.03}$	$0.276^{+0.04}_{-0.03}$	$0.347^{+0.04}_{-0.04}$	$0.449^{+0.06}_{-0.05}$	$0.594^{+0.07}_{-0.06}$	$0.803^{+0.1}_{-0.08}$	$1.1^{+0.13}_{-0.11}$	$1.53^{+0.17}_{-0.14}$	$2.13^{+0.23}_{-0.18}$	$3.08^{+0.31}_{-0.25}$	$6.06^{+0.54}_{-0.42}$	$13.1^{+1.11}_{-0.88}$
A85	r (kpc)	26.3	38.6	53.4	71.2	92.4	118	146	183	230	306	458	640	
$\rho_o=1.04^{+0.1}_{-0.08}\times10^6$	M_g (10^{12} $M_\odot$)	$0.0679^{+0.003}_{-0.003}$	$0.168^{+0.006}_{-0.006}$	$0.326^{+0.01}_{-0.01}$	$0.6^{+0.02}_{-0.02}$	$1.07^{+0.03}_{-0.03}$	$1.74^{+0.04}_{-0.04}$	$2.6^{+0.05}_{-0.05}$	$3.97^{+0.07}_{-0.07}$	$6.3^{+0.1}_{-0.09}$	$10.5^{+0.13}_{-0.13}$	$19.3^{+0.29}_{-0.29}$	$37.6^{+0.46}_{-0.46}$	
$R_s=3.81^{+0.66}_{-0.53}\times10^2$	M (10^{13} $M_\odot$)	-	$0.331^{+0.05}_{-0.05}$	$0.604^{+0.1}_{-0.09}$	$1.02^{+0.16}_{-0.15}$	$1.61^{+0.24}_{-0.22}$	$2.44^{+0.35}_{-0.32}$	$3.47^{+0.48}_{-0.42}$	$4.95^{+0.65}_{-0.56}$	$7.03^{+0.88}_{-0.74}$	$10.6^{+1.23}_{-1.01}$	$17.8^{+1.9}_{-1.5}$	$26.3^{+2.64}_{-2.09}$	
A133	r (kpc)	54.1	63.5	75.8	90.5	110	132	151	184	230	299	410	654	
$\rho_o=1.09^{+0.21}_{-0.11}\times10^6$	M_g (10^{12} $M_\odot$)	$0.247^{+0.01}_{-0.01}$	$0.343^{+0.02}_{-0.03}$	$0.442^{+0.06}_{-0.03}$	$0.615^{+0.06}_{-0.04}$	$0.894^{+0.07}_{-0.05}$	$1.29^{+0.08}_{-0.07}$	$1.65^{+0.1}_{-0.09}$	$2.41^{+0.12}_{-0.11}$	$3.58^{+0.15}_{-0.14}$	$5.54^{+0.21}_{-0.2}$	$9.64^{+0.3}_{-0.29}$	$20.6^{+0.56}_{-0.56}$	
$R_s=3.14^{+1.3}_{-0.75}\times10^2$	M (10^{13} $M_\odot$)	-	$0.685^{+0.21}_{-0.17}$	$0.933^{+0.28}_{-0.22}$	$1.26^{+0.37}_{-0.28}$	$1.74^{+0.49}_{-0.36}$	$2.37^{+0.65}_{-0.45}$	$2.91^{+0.78}_{-0.52}$	$3.93^{+1.0}_{-0.63}$	$5.43^{+1.31}_{-0.77}$	$7.78^{+1.75}_{-0.95}$	$11.5^{+2.39}_{-1.22}$	$19.3^{+3.68}_{-1.91}$	
A262	r (kpc)	13.0	19.4	27.7	36.8	47.8	59.9	74.4	94.7	137	252	357		
$\rho_o=2.29^{+0.09}_{-0.07}\times10^6$	M_g (10^{11} $M_\odot$)	$0.0624^{+0.002}_{-0.002}$	$0.13^{+0.004}_{-0.004}$	$0.252^{+0.008}_{-0.008}$	$0.445^{+0.01}_{-0.01}$	$0.799^{+0.02}_{-0.02}$	$1.28^{+0.03}_{-0.03}$	$2.07^{+0.04}_{-0.04}$	$3.27^{+0.06}_{-0.06}$	$7.62^{+0.11}_{-0.11}$	$22.8^{+0.41}_{-0.4}$	$49.6^{+0.8}_{-0.79}$		
$R_s=1.34^{+0.11}_{-0.1}\times10^2$	M (10^{12} $M_\odot$)	-	$0.618^{+0.05}_{-0.04}$	$1.18^{+0.08}_{-0.08}$	$1.93^{+0.13}_{-0.12}$	$2.99^{+0.19}_{-0.17}$	$4.29^{+0.25}_{-0.23}$	$6.0^{+0.33}_{-0.3}$	$8.54^{+0.43}_{-0.38}$	$14.1^{+0.62}_{-0.54}$	$28.8^{+1.08}_{-0.93}$	$40.6^{+1.52}_{-1.33}$		
A478	r (kpc)	24.4	37.8	54.0	73.4	94.8	123	159	205	266	358	614	1230	
$\rho_o=8.38^{+0.64}_{-0.53}\times10^5$	M_g (10^{12} $M_\odot$)	$0.0831^{+0.004}_{-0.004}$	$0.277^{+0.008}_{-0.008}$	$0.606^{+0.01}_{-0.01}$	$1.18^{+0.02}_{-0.02}$	$2.07^{+0.03}_{-0.03}$	$3.43^{+0.05}_{-0.05}$	$5.71^{+0.07}_{-0.07}$	$9.14^{+0.1}_{-0.1}$	$14.1^{+0.14}_{-0.14}$	$22.8^{+0.21}_{-0.21}$	$51.6^{+0.5}_{-0.5}$	$118.0^{+2.84}_{-2.8}$	
$R_s=5.53^{+0.68}_{-0.56}\times10^2$	M (10^{13} $M_\odot$)	-	$0.386^{+0.05}_{-0.05}$	$0.758^{+0.09}_{-0.09}$	$1.34^{+0.16}_{-0.15}$	$2.14^{+0.25}_{-0.23}$	$3.37^{+0.38}_{-0.35}$	$5.27^{+0.58}_{-0.52}$	$8.11^{+0.85}_{-0.75}$	$12.3^{+1.21}_{-1.06}$	$19.1^{+1.77}_{-1.52}$	$39.7^{+3.26}_{-2.71}$	$86.4^{+6.55}_{-5.47}$	
A496	r (kpc)	86.0	93.9	103	114	126	142	162	195	314	492	714		
$\rho_o=6.51^{+0.11}_{-0.11}\times10^6$	M_g (10^{12} $M_\odot$)	$0.765^{+0.006}_{-0.006}$	$0.884^{+0.01}_{-0.01}$	$1.03^{+0.02}_{-0.02}$	$1.22^{+0.02}_{-0.02}$	$1.5^{+0.02}_{-0.02}$	$1.87^{+0.03}_{-0.03}$	$2.33^{+0.03}_{-0.03}$	$2.95^{+0.05}_{-0.05}$	$6.83^{+0.11}_{-0.1}$	$14.0^{+0.46}_{-0.31}$	$26.5^{+0.78}_{-0.91}$		
$R_s=1.31^{+0.26}_{-0.21}\times10^2$	M (10^{13} $M_\odot$)	-	$2.28^{+0.18}_{-0.16}$	$2.61^{+0.2}_{-0.17}$	$2.97^{+0.21}_{-0.18}$	$3.41^{+0.22}_{-0.18}$	$3.98^{+0.22}_{-0.18}$	$4.67^{+0.22}_{-0.17}$	$5.81^{+0.21}_{-0.15}$	$9.59^{+0.17}_{-0.19}$	$14.3^{+0.49}_{-0.58}$	$18.9^{+1.02}_{-1.09}$		
A1795	r (kpc)	53.1	59.0	66.1	73.9	84.0	97.2	116	141	178	228	314	495	892
$\rho_o=1.17^{+0.03}_{-0.03}\times10^6$	M_g (10^{12} $M_\odot$)	$0.453^{+0.003}_{-0.003}$	$0.571^{+0.008}_{-0.006}$	$0.724^{+0.01}_{-0.009}$	$0.935^{+0.01}_{-0.009}$	$1.2^{+0.01}_{-0.01}$	$1.6^{+0.02}_{-0.01}$	$2.21^{+0.02}_{-0.02}$	$3.16^{+0.02}_{-0.02}$	$4.73^{+0.03}_{-0.03}$	$7.36^{+0.04}_{-0.04}$	$12.7^{+0.06}_{-0.06}$	$25.8^{+0.21}_{-0.22}$	$57.5^{+1.68}_{-1.54}$
$R_s=3.73^{+0.21}_{-0.21}\times10^2$	M (10^{13} $M_\odot$)	-	$0.802^{+0.04}_{-0.04}$	$0.984^{+0.05}_{-0.05}$	$1.2^{+0.06}_{-0.06}$	$1.51^{+0.07}_{-0.07}$	$1.94^{+0.09}_{-0.09}$	$2.61^{+0.12}_{-0.11}$	$3.63^{+0.16}_{-0.15}$	$5.22^{+0.21}_{-0.2}$	$7.64^{+0.29}_{-0.27}$	$12.0^{+0.41}_{-0.38}$	$21.5^{+0.64}_{-0.58}$	$40.4^{+1.12}_{-1.03}$
A2029	r (kpc)	7.18	20.3	32.0	43.8	57.9	73.4	93.6	120	154	202	273	431	970
$\rho_o=2.2^{+0.126}_{-0.11}\times10^6$	M_g (10^{12} $M_\odot$)	$0.00577^{+0.0003}_{-0.0003}$	$0.0575^{+0.002}_{-0.002}$	$0.164^{+0.004}_{-0.004}$	$0.343^{+0.006}_{-0.006}$	$0.629^{+0.01}_{-0.01}$	$1.06^{+0.015}_{-0.015}$	$1.77^{+0.021}_{-0.021}$	$2.9^{+0.03}_{-0.03}$	$4.63^{+0.044}_{-0.044}$	$7.4^{+0.063}_{-0.063}$	$13.0^{+0.091}_{-0.097}$	$24.5^{+0.21}_{-0.211}$	$89.5^{+1.068}_{-1.05}$
$R_s=3.04^{+0.296}_{-0.257}\times10^2$	M (10^{13} $M_\odot$)	-	$0.163^{+0.016}_{-0.015}$	$0.388^{+0.036}_{-0.035}$	$0.692^{+0.063}_{-0.061}$	$1.15^{+0.101}_{-0.097}$	$1.74^{+0.147}_{-0.14}$	$2.63^{+0.214}_{-0.201}$	$3.95^{+0.305}_{-0.283}$	$5.86^{+0.427}_{-0.39}$	$8.76^{+0.596}_{-0.536}$	$13.3^{+0.839}_{-0.743}$	$23.5^{+1.34}_{-1.173}$	$53.0^{+2.972}_{-2.664}$
A2199	r (kpc)	14.8	22.8	30.9	39.0	47.9	60.4	76.6	96.0	119	150	192	268	444
$\rho_o=1.02^{+0.063}_{-0.046}\times10^6$	M_g (10^{12} $M_\odot$)	$0.0135^{+0.0005}_{-0.0005}$	$0.0351^{+0.001}_{-0.001}$	$0.0738^{+0.002}_{-0.002}$	$0.127^{+0.003}_{-0.003}$	$0.208^{+0.004}_{-0.004}$	$0.347^{+0.006}_{-0.006}$	$0.594^{+0.008}_{-0.008}$	$0.929^{+0.011}_{-0.011}$	$1.43^{+0.015}_{-0.014}$	$2.21^{+0.019}_{-0.019}$	$3.41^{+0.026}_{-0.026}$	$6.69^{+0.034}_{-0.034}$	$13.4^{+0.074}_{-0.074}$
$R_s=3.63^{+0.356}_{-0.255}\times10^2$	M (10^{13} $M_\odot$)	-	$0.114^{+0.012}_{-0.009}$	$0.204^{+0.021}_{-0.017}$	$0.316^{+0.032}_{-0.025}$	$0.463^{+0.046}_{-0.036}$	$0.705^{+0.068}_{-0.053}$	$1.08^{+0.101}_{-0.078}$	$1.6^{+0.144}_{-0.111}$	$2.31^{+0.201}_{-0.153}$	$3.34^{+0.278}_{-0.21}$	$4.93^{+0.39}_{-0.291}$	$8.06^{+0.589}_{-0.433}$	$15.6^{+1.025}_{-0.742}$
A2204	r (kpc)	130	141	154	170	190	217	248	293	364	479	673	1020	1580
$\rho_o=3.11^{+0.11}_{-0.09}\times10^6$	M_g (10^{13} $M_\odot$)	$0.55^{+0.005}_{-0.005}$	$0.616^{+0.009}_{-0.03}$	$0.693^{+0.02}_{-0.03}$	$0.811^{+0.02}_{-0.03}$	$0.95^{+0.02}_{-0.03}$	$1.14^{+0.02}_{-0.03}$	$1.38^{+0.03}_{-0.04}$	$1.77^{+0.04}_{-0.04}$	$2.47^{+0.05}_{-0.05}$	$3.68^{+0.06}_{-0.06}$	$5.79^{+0.1}_{-0.1}$	$9.98^{+0.2}_{-0.2}$	$17.4^{+0.56}_{-0.56}$
$R_s=3.05^{+0.54}_{-0.45}\times10^2$	M (10^{14} $M_\odot$)	-	$0.716^{+0.07}_{-0.07}$	$0.822^{+0.08}_{-0.07}$	$0.953^{+0.09}_{-0.08}$	$1.13^{+0.1}_{-0.09}$	$1.36^{+0.11}_{-0.1}$	$1.65^{+0.12}_{-0.1}$	$2.06^{+0.13}_{-0.11}$	$2.72^{+0.15}_{-0.11}$	$3.74^{+0.16}_{-0.12}$	$5.36^{+0.2}_{-0.15}$	$7.87^{+0.33}_{-0.31}$	$11.1^{+0.63}_{-0.61}$
A2597	r (kpc)	59.0	66.4	75.9	87.3	103	126	157	204	289	551	966		
$\rho_o=2.1^{+0.07}_{-0.08}\times10^6$	M_g (10^{12} $M_\odot$)	$0.671^{+0.005}_{-0.005}$	$0.819^{+0.01}_{-0.01}$	$1.02^{+0.01}_{-0.01}$	$1.29^{+0.02}_{-0.02}$	$1.71^{+0.03}_{-0.03}$	$2.33^{+0.03}_{-0.03}$	$3.33^{+0.04}_{-0.04}$	$4.89^{+0.06}_{-0.06}$	$8.34^{+0.08}_{-0.08}$	$18.6^{+0.28}_{-0.28}$	$39.5^{+1.51}_{-1.53}$		
$R_s=2.34^{+0.2}_{-0.25}\times10^2$	M (10^{13} $M_\odot$)	-	$0.986^{+0.06}_{-0.09}$	$1.24^{+0.08}_{-0.1}$	$1.56^{+0.09}_{-0.12}$	$2.04^{+0.12}_{-0.15}$	$2.76^{+0.15}_{-0.19}$	$3.84^{+0.19}_{-0.24}$	$5.54^{+0.24}_{-0.29}$	$8.63^{+0.33}_{-0.38}$	$17.5^{+0.57}_{-0.67}$	$28.5^{+1.05}_{-1.31}$		
A4059	r (kpc)	54.9	63.4	73.5	85.7	100	118	141	170	215	308	549	826	
$\rho_o=2.11^{+0.09}_{-0.08}\times10^6$	M_g (10^{12} $M_\odot$)	$0.203^{+0.006}_{-0.008}$	$0.288^{+0.008}_{-0.01}$	$0.415^{+0.01}_{-0.01}$	$0.583^{+0.01}_{-0.02}$	$0.803^{+0.02}_{-0.02}$	$1.1^{+0.02}_{-0.02}$	$1.54^{+0.03}_{-0.03}$	$2.29^{+0.03}_{-0.04}$	$3.34^{+0.05}_{-0.05}$	$6.15^{+0.08}_{-0.08}$	$13.7^{+0.3}_{-0.3}$	$24.6^{+0.71}_{-0.73}$	
$R_s=2.37^{+0.29}_{-0.25}\times10^2$	M (10^{13} $M_\odot$)	-	$0.931^{+0.08}_{-0.08}$	$1.2^{+0.11}_{-0.1}$	$1.54^{+0.13}_{-0.12}$	$1.99^{+0.16}_{-0.15}$	$2.56^{+0.19}_{-0.18}$	$3.35^{+0.24}_{-0.22}$	$4.42^{+0.29}_{-0.26}$	$6.09^{+0.36}_{-0.31}$	$9.6^{+0.48}_{-0.4}$	$17.9^{+0.78}_{-0.67}$	$25.9^{+1.21}_{-1.09}$	
Centaurus	r (kpc)	39.6	42.9	47.1	52.1	58.2	67.3	83.8	113	169	249			
$\rho_o=1.36^{+0.01}_{-0.01}\times10^6$	M_g (10^{11} $M_\odot$)	$0.944^{+0.005}_{-0.005}$	$1.06^{+0.008}_{-0.008}$	$1.26^{+0.01}_{-0.01}$	$1.49^{+0.01}_{-0.01}$	$1.82^{+0.02}_{-0.02}$	$2.32^{+0.03}_{-0.03}$	$3.67^{+0.04}_{-0.04}$	$6.63^{+0.05}_{-0.05}$	$12.8^{+0.13}_{-0.13}$	$31.7^{+0.21}_{-0.21}$			
$R_s=276.0$	M (10^{12} $M_\odot$)	-	$3.67^{+0.03}_{-0.04}$	$4.35^{+0.03}_{-0.05}$	$5.22^{+0.04}_{-0.06}$	$6.35^{+0.05}_{-0.07}$	$8.19^{+0.06}_{-0.09}$	$11.9^{+0.09}_{-0.13}$	$19.5^{+0.15}_{-0.21}$	$36.3^{+0.28}_{-0.39}$	$62.3^{+0.47}_{-0.68}$			
Hydra A	r (kpc)	55.3	63.6	74.5	88.7	106	126	150	180	224	316	474	790	
$\rho_o=8.96^{+0.31}_{-0.16}\times10^5$	M_g (10^{12} $M_\odot$)	$0.472^{+0.003}_{-0.003}$	$0.607^{+0.005}_{-0.005}$	$0.787^{+0.008}_{-0.008}$	$1.06^{+0.01}_{-0.01}$	$1.39^{+0.01}_{-0.01}$	$1.85^{+0.02}_{-0.02}$	$2.53^{+0.03}_{-0.03}$	$3.53^{+0.03}_{-0.03}$	$5.44^{+0.04}_{-0.04}$	$9.28^{+0.07}_{-0.07}$	$17.1^{+0.15}_{-0.15}$	$31.6^{+0.47}_{-0.47}$	
$R_s=3.41^{+0.25}_{-0.24}\times10^2$	M (10^{13} $M_\odot$)	-	$0.626^{+0.04}_{-0.04}$	$0.828^{+0.05}_{-0.05}$	$1.12^{+0.07}_{-0.06}$	$1.51^{+0.09}_{-0.08}$	$2.02^{+0.11}_{-0.1}$	$2.68^{+0.14}_{-0.12}$	$3.54^{+0.18}_{-0.15}$	$4.9^{+0.23}_{-0.18}$	$7.9^{+0.33}_{-0.23}$	$13.1^{+0.48}_{-0.28}$	$22.6^{+0.79}_{-0.42}$	
MKW3S	r (kpc)	95.3	104	114	126	141	160	186	223	275	364	567		
$\rho_o=2.26^{+0.79}_{-0.28}\times10^6$	M_g (10^{12} $M_\odot$)	$0.816^{+0.01}_{-0.01}$	$0.966^{+0.01}_{-0.02}$	$1.13^{+0.03}_{-0.02}$	$1.37^{+0.03}_{-0.03}$	$1.68^{+0.04}_{-0.04}$	$2.13^{+0.05}_{-0.05}$	$2.76^{+0.06}_{-0.06}$	$3.65^{+0.07}_{-0.08}$	$5.12^{+0.09}_{-0.08}$	$7.99^{+0.12}_{-0.12}$	$14.1^{+0.19}_{-0.19}$		
$R_s=2.14^{+2.06}_{-0.9}\times10^2$	M (10^{13} $M_\odot$)	-	$1.94^{+0.97}_{-0.6}$	$2.24^{+1.1}_{-0.65}$	$2.61^{+1.25}_{-0.69}$	$3.06^{+1.44}_{-0.74}$	$3.67^{+1.68}_{-0.79}$	$4.54^{+2.0}_{-0.85}$	$5.76^{+2.44}_{-0.91}$	$7.46^{+3.0}_{-0.99}$	$10.3^{+3.86}_{-1.26}$	$16.0^{+5.65}_{-2.4}$		
NGC507	r (kpc)	20.1	24.8	30.9	39.5	49.0	62.2	79.4	100	127	167			
$\rho_o=2.31^{+0.53}_{-0.33}\times10^6$	M_g (10^{11} $M_\odot$)	$0.0713^{+0.009}_{-0.009}$	$0.109^{+0.02}_{-0.02}$	$0.187^{+0.03}_{-0.03}$	$0.329^{+0.04}_{-0.04}$	$0.55^{+0.05}_{-0.05}$	$0.861^{+0.07}_{-0.07}$	$1.33^{+0.1}_{-0.1}$	$2.1^{+0.14}_{-0.13}$	$3.07^{+0.23}_{-0.22}$	$6.63^{+0.26}_{-0.25}$			
$R_s=1.15^{+0.77}_{-0.34}\times10^2$	M (10^{12} $M_\odot$)	-	$0.768^{+0.28}_{-0.36}$	$1.16^{+0.46}_{-0.35}$	$1.76^{+0.67}_{-0.48}$	$2.49^{+0.91}_{-0.63}$	$3.61^{+1.25}_{-0.81}$	$5.17^{+1.69}_{-1.03}$	$7.13^{+2.17}_{-1.26}$	$9.72^{+2.74}_{-1.54}$	$13.6^{+3.49}_{-1.98}$			

NGC1550	r (kpc)	16.6	20.8	25.9	32.4	40.5	50.7	63.3	79.2	99.0	124	155	193	242	
ρ_o=$8.23^{+0.22}_{-0.14}\times10^{6}$	M_g (10^{11} $M_\odot$)	$0.0891^{+0.002}_{-0.002}$	$0.13^{+0.005}_{-0.005}$	$0.202^{+0.009}_{-0.008}$	$0.308^{+0.01}_{-0.01}$	$0.499^{+0.02}_{-0.02}$	$0.762^{+0.02}_{-0.03}$	$1.17^{+0.05}_{-0.04}$	$1.83^{+0.08}_{-0.08}$	$2.77^{+0.1}_{-0.1}$	$4.15^{+0.13}_{-0.13}$	$5.87^{+0.26}_{-0.19}$	$7.82^{+0.48}_{-0.59}$	$13.4^{+0.58}_{-0.73}$	
R_s=$5.87^{+0.53}_{-0.37}\times10^{1}$	M (10^{12} $M_\odot$)	-	$0.894^{+0.05}_{-0.04}$	$1.28^{+0.07}_{-0.05}$	$1.81^{+0.09}_{-0.07}$	$2.51^{+0.12}_{-0.08}$	$3.42^{+0.14}_{-0.09}$	$4.58^{+0.16}_{-0.11}$	$6.02^{+0.19}_{-0.12}$	$7.76^{+0.22}_{-0.13}$	$9.81^{+0.26}_{-0.16}$	$12.2^{+0.32}_{-0.21}$	$14.9^{+0.43}_{-0.29}$	$17.8^{+0.57}_{-0.39}$	
NGC5044	r (kpc)	18.7	23.4	29.2	36.5	45.6	57.1	71.3	89.1	111	139	174	218		
ρ_o=$1.01^{+0.03}_{-0.02}\times10^{7}$	M_g (10^{11} $M_\odot$)	$0.12^{+0.002}_{-0.002}$	$0.18^{+0.005}_{-0.005}$	$0.268^{+0.007}_{-0.008}$	$0.396^{+0.01}_{-0.01}$	$0.583^{+0.02}_{-0.02}$	$0.806^{+0.03}_{-0.03}$	$1.2^{+0.05}_{-0.05}$	$1.82^{+0.09}_{-0.09}$	$2.78^{+0.12}_{-0.12}$	$3.99^{+0.2}_{-0.21}$	$5.08^{+0.29}_{-0.36}$	$8.99^{+0.45}_{-0.45}$		
R_s=$4.51^{+0.54}_{-0.47}\times10^{1}$	M (10^{12} $M_\odot$)	-	$0.905^{+0.06}_{-0.06}$	$1.26^{+0.07}_{-0.07}$	$1.73^{+0.09}_{-0.08}$	$2.33^{+0.1}_{-0.09}$	$3.08^{+0.12}_{-0.1}$	$3.99^{+0.13}_{-0.1}$	$5.07^{+0.15}_{-0.12}$	$6.32^{+0.18}_{-0.16}$	$7.75^{+0.24}_{-0.22}$	$9.35^{+0.33}_{-0.31}$	$11.1^{+0.44}_{-0.43}$		
PKS1404	r (kpc)	8.66	13.0	17.8	23.0	29.3	36.8	48.1	64.0	87.7	140	260			
ρ_o=$4.4^{+0.12}_{-0.11}\times10^{6}$	M_g (10^{11} $M_\odot$)	$0.0231^{+0.002}_{-0.002}$	$0.0599^{+0.004}_{-0.004}$	$0.134^{+0.006}_{-0.006}$	$0.241^{+0.009}_{-0.009}$	$0.396^{+0.01}_{-0.01}$	$0.665^{+0.02}_{-0.02}$	$1.1^{+0.03}_{-0.03}$	$1.85^{+0.04}_{-0.04}$	$3.34^{+0.06}_{-0.06}$	$7.44^{+0.13}_{-0.13}$	$23.6^{+0.45}_{-0.43}$			
R_s=$9.82^{+0.6}_{-0.54}\times10^{1}$	M (10^{12} $M_\odot$)	-	$0.394^{+0.02}_{-0.02}$	$0.695^{+0.04}_{-0.04}$	$1.1^{+0.06}_{-0.05}$	$1.66^{+0.08}_{-0.08}$	$2.43^{+0.11}_{-0.11}$	$3.72^{+0.16}_{-0.15}$	$5.7^{+0.22}_{-0.21}$	$8.85^{+0.31}_{-0.28}$	$15.9^{+0.48}_{-0.43}$	$30.2^{+0.87}_{-0.8}$			
Sersic159	r (kpc)	33.1	37.6	43.0	49.5	57.3	67.5	80.7	97.8	125	177	282	553		
ρ_o=$1.62^{+0.11}_{-0.1}\times10^{6}$	M_g (10^{12} $M_\odot$)	$0.134^{+0.003}_{-0.003}$	$0.175^{+0.006}_{-0.006}$	$0.229^{+0.009}_{-0.008}$	$0.316^{+0.01}_{-0.01}$	$0.421^{+0.01}_{-0.01}$	$0.574^{+0.02}_{-0.02}$	$0.794^{+0.02}_{-0.02}$	$1.12^{+0.03}_{-0.03}$	$1.7^{+0.04}_{-0.03}$	$3.03^{+0.06}_{-0.05}$	$5.83^{+0.09}_{-0.09}$	$15.1^{+0.26}_{-0.25}$		
R_s=$2.33^{+0.29}_{-0.26}\times10^{2}$	M (10^{13} $M_\odot$)	-	$0.277^{+0.03}_{-0.03}$	$0.353^{+0.04}_{-0.04}$	$0.453^{+0.05}_{-0.05}$	$0.586^{+0.06}_{-0.06}$	$0.774^{+0.08}_{-0.08}$	$1.04^{+0.11}_{-0.1}$	$1.43^{+0.14}_{-0.13}$	$2.1^{+0.19}_{-0.18}$	$3.48^{+0.29}_{-0.27}$	$6.38^{+0.48}_{-0.42}$	$13.3^{+0.93}_{-0.81}$		
3C388	r (kpc)	8.41	40.5	78.9	140	270	463	757							
ρ_o=$4.32^{+0.46}_{-0.28}\times10^{6}$	M_g (10^{12} $M_\odot$)	$0.00351^{+0.0008}_{-0.0007}$	$0.0896^{+0.02}_{-0.02}$	$0.311^{+0.05}_{-0.05}$	$0.988^{+0.09}_{-0.1}$	$3.3^{+0.23}_{-0.21}$	$7.31^{+0.7}_{-0.68}$	$17.3^{+1.31}_{-1.31}$							
R_s=$1.27^{+0.38}_{-0.27}\times10^{2}$	M (10^{13} $M_\odot$)	-	$0.394^{+0.08}_{-0.07}$	$1.13^{+0.18}_{-0.14}$	$2.48^{+0.32}_{-0.21}$	$5.18^{+0.55}_{-0.34}$	$8.47^{+0.95}_{-0.7}$	$12.2^{+1.61}_{-1.28}$							
3C401	r (kpc)	8.14	48.5	113	223	421	816								
ρ_o=$2.03^{+0.9}_{-0.39}\times10^{6}$	M_g (10^{12} $M_\odot$)	$0.00032^{+9e-05}_{-8e-05}$	$0.0148^{+0.003}_{-0.003}$	$0.0825^{+0.005}_{-0.006}$	$0.264^{+0.02}_{-0.02}$	$0.79^{+0.06}_{-0.04}$	$2.26^{+0.33}_{-0.28}$								
R_s=$2.1^{+1.82}_{-0.82}\times10^{2}$	M (10^{13} $M_\odot$)	-	$0.483^{+0.29}_{-0.22}$	$1.93^{+1.05}_{-0.59}$	$4.99^{+2.45}_{-1.06}$	$10.4^{+4.67}_{-2.0}$	$18.9^{+8.45}_{-4.34}$								
4C55	r (kpc)	28.1	37.9	52.5	70.0	94.6	127	178	275	585	1330				
ρ_o=$9.31^{+1.84}_{-1.19}\times10^{5}$	M_g (10^{12} $M_\odot$)	$0.136^{+0.01}_{-0.01}$	$0.263^{+0.02}_{-0.02}$	$0.482^{+0.04}_{-0.04}$	$0.866^{+0.06}_{-0.06}$	$1.48^{+0.09}_{-0.09}$	$2.55^{+0.13}_{-0.12}$	$4.61^{+0.18}_{-0.18}$	$9.7^{+0.26}_{-0.26}$	$27.4^{+0.54}_{-0.73}$	$80.3^{+5.65}_{-5.01}$				
R_s=$4.28^{+1.4}_{-0.9}\times10^{2}$	M (10^{13} $M_\odot$)	-	$0.324^{+0.1}_{-0.09}$	$0.598^{+0.18}_{-0.15}$	$1.01^{+0.29}_{-0.25}$	$1.73^{+0.48}_{-0.39}$	$2.86^{+0.77}_{-0.61}$	$5.0^{+1.28}_{-0.95}$	$9.74^{+2.32}_{-1.6}$	$26.4^{+5.46}_{-3.46}$	$61.0^{+12.11}_{-8.12}$				
A1835	r (kpc)	29.1	37.0	48.2	62.6	81.4	106	140	188	265	403	830	1550		
ρ_o=$1.47^{+0.05}_{-0.06}\times10^{6}$	M_g (10^{12} $M_\odot$)	$0.262^{+0.007}_{-0.007}$	$0.491^{+0.01}_{-0.01}$	$0.867^{+0.02}_{-0.02}$	$1.4^{+0.03}_{-0.03}$	$2.25^{+0.04}_{-0.04}$	$3.61^{+0.06}_{-0.06}$	$5.89^{+0.09}_{-0.08}$	$9.97^{+0.12}_{-0.12}$	$17.3^{+0.18}_{-0.18}$	$34.2^{+0.32}_{-0.29}$	$90.4^{+0.87}_{-0.86}$	$190.0^{+3.17}_{-3.18}$		
R_s=$4.39^{+0.29}_{-0.31}\times10^{2}$	M (10^{13} $M_\odot$)	-	$0.506^{+0.03}_{-0.04}$	$0.83^{+0.05}_{-0.06}$	$1.35^{+0.09}_{-0.1}$	$2.17^{+0.13}_{-0.15}$	$3.45^{+0.2}_{-0.23}$	$5.55^{+0.31}_{-0.35}$	$8.97^{+0.47}_{-0.52}$	$15.2^{+0.72}_{-0.79}$	$27.3^{+1.14}_{-1.23}$	$64.5^{+2.32}_{-2.5}$	$116.0^{+4.31}_{-4.73}$		
Cygnus A	r (kpc)	77.8	88.8	103	119	140	168	203	244	298	363	453	598	815	
ρ_o=$6.33^{+0.63}_{-0.3}\times10^{6}$	M_g (10^{12} $M_\odot$)	$1.09^{+0.005}_{-0.002}$	$1.3^{+0.008}_{-0.02}$	$1.59^{+0.02}_{-0.02}$	$1.96^{+0.02}_{-0.03}$	$2.52^{+0.03}_{-0.04}$	$3.49^{+0.04}_{-0.04}$	$4.59^{+0.06}_{-0.06}$	$6.2^{+0.07}_{-0.07}$	$8.37^{+0.1}_{-0.1}$	$11.3^{+0.17}_{-0.17}$	$16.0^{+0.27}_{-0.26}$	$23.1^{+0.55}_{-0.54}$	$59.0^{+0.65}_{-0.64}$	
R_s=$1.45^{+0.7}_{-0.43}\times10^{2}$	M (10^{13} $M_\odot$)	-	$2.41^{+0.52}_{-0.39}$	$2.99^{+0.6}_{-0.42}$	$3.65^{+0.68}_{-0.44}$	$4.51^{+0.77}_{-0.45}$	$5.73^{+0.88}_{-0.44}$	$7.17^{+0.97}_{-0.42}$	$8.85^{+1.05}_{-0.43}$	$10.9^{+1.16}_{-0.54}$	$13.2^{+1.32}_{-0.81}$	$16.2^{+1.66}_{-1.28}$	$20.4^{+2.4}_{-2.07}$	$25.6^{+3.68}_{-3.21}$	
HCG62	r (kpc)	16.5	20.7	25.8	32.3	40.4	50.4	63.1	78.8	98.5	123	154	192	241	
ρ_o=$3.63^{+0.32}_{-0.26}\times10^{6}$	M_g (10^{11} $M_\odot$)	$0.0558^{+0.002}_{-0.002}$	$0.08^{+0.005}_{-0.005}$	$0.112^{+0.008}_{-0.008}$	$0.162^{+0.01}_{-0.01}$	$0.231^{+0.02}_{-0.02}$	$0.345^{+0.02}_{-0.02}$	$0.5^{+0.03}_{-0.03}$	$0.782^{+0.04}_{-0.05}$	$1.12^{+0.11}_{-0.1}$	$1.67^{+0.18}_{-0.18}$	$2.66^{+0.37}_{-0.35}$	$4.2^{+0.58}_{-0.57}$	$12.7^{+15.92}_{-4.62}$	
R_s=$8.67^{+2.02}_{-1.66}\times10^{1}$	M (10^{12} $M_\odot$)	-	$0.642^{+0.11}_{-0.11}$	$0.94^{+0.15}_{-0.16}$	$1.36^{+0.21}_{-0.21}$	$1.94^{+0.29}_{-0.27}$	$2.73^{+0.37}_{-0.34}$	$3.78^{+0.48}_{-0.41}$	$5.13^{+0.6}_{-0.49}$	$6.84^{+0.73}_{-0.57}$	$8.95^{+0.88}_{-0.68}$	$11.5^{+1.06}_{-0.82}$	$14.5^{+1.29}_{-1.04}$	$17.9^{+1.6}_{-1.35}$	
Hercules A	r (kpc)	171	186	207	235	271	329	404	516	674	1110				
ρ_o=$8.73^{+2.26}_{-0.55}\times10^{6}$	M_g (10^{13} $M_\odot$)	$0.352^{+0.005}_{-0.005}$	$0.419^{+0.01}_{-0.01}$	$0.494^{+0.01}_{-0.02}$	$0.589^{+0.02}_{-0.02}$	$0.738^{+0.03}_{-0.03}$	$0.945^{+0.03}_{-0.03}$	$1.24^{+0.06}_{-0.05}$	$1.72^{+0.12}_{-0.1}$	$2.33^{+0.2}_{-0.18}$	$5.62^{+0.69}_{-0.7}$				
R_s=$1.35^{+1.87}_{-0.85}\times10^{2}$	M (10^{14} $M_\odot$)	-	$0.782^{+0.28}_{-0.05}$	$0.886^{+0.3}_{-0.07}$	$1.02^{+0.33}_{-0.11}$	$1.18^{+0.36}_{-0.18}$	$1.43^{+0.4}_{-0.28}$	$1.73^{+0.45}_{-0.42}$	$2.13^{+0.56}_{-0.62}$	$2.61^{+0.75}_{-0.87}$	$3.63^{+1.41}_{-1.44}$				
MACSJ0159	r (kpc)	23.4	47.0	77.5	120	176	260	435	1310						
ρ_o=$7.51^{+6.23}_{-2.32}\times10^{5}$	M_g (10^{12} $M_\odot$)	$0.142^{+0.01}_{-0.01}$	$0.596^{+0.03}_{-0.03}$	$1.5^{+0.09}_{-0.09}$	$3.39^{+0.17}_{-0.17}$	$7.2^{+0.27}_{-0.27}$	$14.5^{+0.42}_{-0.42}$	$34.7^{+0.57}_{-0.58}$	$158.0^{+2.7}_{-2.7}$						
R_s=$7.0^{+7.34}_{-2.67}\times10^{2}$	M (10^{13} $M_\odot$)	$132.0^{+111.22}_{-40.99}$	$0.176^{+0.17}_{-0.11}$	$0.677^{+0.65}_{-0.42}$	$1.75^{+1.67}_{-1.02}$	$3.92^{+3.72}_{-2.1}$	$7.67^{+7.19}_{-3.75}$	$14.7^{+13.58}_{-6.42}$	$32.8^{+29.44}_{-12.11}$						
MACSJ0242	r (kpc)	24.0	51.2	97.6	209	679									
ρ_o=$2.57^{+2.78}_{-0.51}\times10^{6}$	M_g (10^{12} $M_\odot$)	$0.226^{+0.03}_{-0.03}$	$0.974^{+0.08}_{-0.14}$	$2.84^{+0.21}_{-0.24}$	$9.58^{+0.37}_{-0.47}$	$49.7^{+1.12}_{-2.55}$									
R_s=$2.58^{+2.34}_{-0.81}\times10^{2}$	M (10^{13} $M_\odot$)	$31.7^{+34.38}_{-6.51}$	$0.215^{+0.25}_{-0.09}$	$0.867^{+1.01}_{-0.33}$	$2.6^{+2.97}_{-0.81}$	$8.17^{+9.12}_{-1.9}$									
MACSJ0429	r (kpc)	28.2	58.0	103	183	336	791								
ρ_o=$3.94^{+1.01}_{-0.49}\times10^{6}$	M_g (10^{12} $M_\odot$)	$0.202^{+0.03}_{-0.03}$	$0.899^{+0.07}_{-0.07}$	$2.58^{+0.19}_{-0.18}$	$6.69^{+0.38}_{-0.38}$	$17.5^{+0.96}_{-0.96}$	$57.2^{+3.39}_{-3.38}$								
R_s=$2.02^{+1.03}_{-0.51}\times10^{2}$	M (10^{13} $M_\odot$)	$33.0^{+8.67}_{-4.69}$	$0.339^{+0.13}_{-0.1}$	$1.22^{+0.45}_{-0.3}$	$3.07^{+1.03}_{-0.6}$	$7.04^{+2.11}_{-1.05}$	$14.7^{+3.92}_{-1.84}$								
MACSJ0913	r (kpc)	24.4	45.1	76.1	141	336	827								
ρ_o=$2.28^{+0.57}_{-0.27}\times10^{6}$	M_g (10^{12} $M_\odot$)	$0.159^{+0.02}_{-0.02}$	$0.68^{+0.04}_{-0.04}$	$1.84^{+0.07}_{-0.07}$	$4.99^{+0.15}_{-0.15}$	$16.9^{+0.51}_{-0.51}$	$55.1^{+2.66}_{-2.6}$								
R_s=$3.05^{+1.15}_{-0.57}\times10^{2}$	M (10^{13} $M_\odot$)	$47.8^{+12.0}_{-5.83}$	$0.237^{+0.08}_{-0.06}$	$0.746^{+0.26}_{-0.16}$	$1.9^{+0.63}_{-0.37}$	$5.26^{+1.62}_{-0.88}$	$18.0^{+4.85}_{-2.31}$								
MACSJ1423	r (kpc)	31.3	45.8	67.4	99.8	161	279	618	1260						
ρ_o=$4.67^{+0.53}_{-0.4}\times10^{6}$	M_g (10^{12} $M_\odot$)	$0.327^{+0.02}_{-0.02}$	$0.738^{+0.04}_{-0.04}$	$1.45^{+0.06}_{-0.06}$	$2.76^{+0.11}_{-0.11}$	$6.04^{+0.18}_{-0.18}$	$14.2^{+0.38}_{-0.38}$	$44.2^{+1.39}_{-1.39}$	$107.0^{+8.73}_{-8.38}$						
R_s=$2.11^{+0.59}_{-0.46}\times10^{2}$	M (10^{13} $M_\odot$)	-	$1.01^{+0.21}_{-0.22}$	$1.96^{+0.38}_{-0.37}$	$3.7^{+0.66}_{-0.59}$	$7.54^{+1.16}_{-0.93}$	$15.3^{+1.95}_{-1.4}$	$34.9^{+4.04}_{-3.22}$	$60.9^{+8.3}_{-7.27}$						
RXJ1532	r (kpc)	60.1	66.6	74.4	85.4	98.4	115	141	179	244	381	969			
ρ_o=$1.1^{+0.52}_{-0.2}\times10^{6}$	M_g (10^{12} $M_\odot$)	$1.34^{+0.03}_{-0.03}$	$1.67^{+0.04}_{-0.04}$	$2.09^{+0.06}_{-0.06}$	$2.64^{+0.09}_{-0.09}$	$3.4^{+0.12}_{-0.12}$	$4.53^{+0.13}_{-0.13}$	$6.21^{+0.17}_{-0.16}$	$8.96^{+0.22}_{-0.22}$	$14.2^{+0.26}_{-0.29}$	$26.2^{+0.45}_{-0.34}$	$81.7^{+2.36}_{-2.28}$			

$R_s=5.02^{+3.78}_{-1.55}\times10^2$	M (10^{13} $M_\odot$)	-	$1.32^{+0.81}_{-0.52}$	$1.61^{+0.98}_{-0.62}$	$2.07^{+1.25}_{-0.78}$	$2.67^{+1.6}_{-0.97}$	$3.54^{+2.1}_{-1.23}$	$4.99^{+2.93}_{-1.64}$	$7.46^{+4.29}_{-2.26}$	$12.2^{+6.83}_{-3.28}$	$23.5^{+12.5}_{-5.26}$	$73.5^{+35.22}_{-13.43}$		
MACSJ1720	r (kpc)	42.2	90.4	158	259	451	797							
$\rho_o=1.22^{+0.33}_{-0.29}\times10^6$	M_g (10^{13} $M_\odot$)	$0.0462^{+0.003}_{-0.003}$	$0.176^{+0.009}_{-0.009}$	$0.504^{+0.02}_{-0.02}$	$1.2^{+0.04}_{-0.04}$	$2.93^{+0.09}_{-0.09}$	$6.48^{+0.24}_{-0.24}$							
$R_s=4.05^{+1.67}_{-1.5}\times10^2$	M (10^{14} $M_\odot$)	$4.38^{+1.19}_{-1.03}$	$0.0492^{+0.02}_{-0.03}$	$0.196^{+0.07}_{-0.09}$	$0.502^{+0.17}_{-0.19}$	$1.08^{+0.34}_{-0.32}$	$2.28^{+0.66}_{-0.56}$							
MACSJ1931	r (kpc)	29.3	36.8	48.2	62.9	77.7	101	132	175	244	381	917	1720	
$\rho_o=5.13^{+1.75}_{-0.88}\times10^5$	M_g (10^{12} $M_\odot$)	$0.299^{+0.01}_{-0.01}$	$0.522^{+0.03}_{-0.03}$	$0.87^{+0.05}_{-0.04}$	$1.46^{+0.07}_{-0.06}$	$2.14^{+0.08}_{-0.08}$	$3.41^{+0.1}_{-0.11}$	$5.23^{+0.15}_{-0.16}$	$8.2^{+0.22}_{-0.23}$	$14.3^{+0.31}_{-0.31}$	$28.5^{+0.5}_{-0.5}$	$84.1^{+2.1}_{-2.1}$	$199.0^{+19.13}_{-13.8}$	
$R_s=8.51^{+3.92}_{-2.03}\times10^2$	M (10^{13} $M_\odot$)	-	$0.356^{+0.16}_{-0.12}$	$0.599^{+0.27}_{-0.2}$	$1.0^{+0.45}_{-0.32}$	$1.49^{+0.67}_{-0.47}$	$2.45^{+1.09}_{-0.75}$	$3.99^{+1.75}_{-1.18}$	$6.61^{+2.85}_{-1.86}$	$11.7^{+4.93}_{-3.07}$	$24.4^{+9.83}_{-5.66}$	$85.5^{+30.99}_{-15.55}$	$176.0^{+60.45}_{-30.22}$	
MACSJ2140	r (kpc)	19.9	33.7	47.5	71.0	102	147	239	523	921				
$\rho_o=4.9^{+0.5}_{-0.25}\times10^6$	M_g (10^{12} $M_\odot$)	$0.0837^{+0.02}_{-0.02}$	$0.337^{+0.03}_{-0.03}$	$0.687^{+0.06}_{-0.06}$	$1.52^{+0.09}_{-0.12}$	$2.48^{+0.33}_{-0.22}$	$4.96^{+0.34}_{-0.24}$	$10.4^{+0.59}_{-0.63}$	$28.1^{+1.32}_{-1.33}$	$57.2^{+3.45}_{-3.92}$				
$R_s=1.76^{+0.36}_{-0.3}\times10^2$	M (10^{13} $M_\odot$)	$33.4^{+3.78}_{-2.57}$	$0.187^{+0.03}_{-0.03}$	$0.49^{+0.08}_{-0.08}$	$0.893^{+0.15}_{-0.13}$	$1.74^{+0.26}_{-0.22}$	$3.03^{+0.42}_{-0.31}$	$5.15^{+0.64}_{-0.42}$	$9.52^{+1.03}_{-0.55}$	$21.3^{+2.19}_{-1.24}$				
MS0735	r (kpc)	258	272	288	309	339	378	432	513	651	954	1550		
$\rho_o=1.44^{+0.29}_{-0.07}\times10^6$	M_g (10^{13} $M_\odot$)	$0.987^{+0.008}_{-0.009}$	$1.06^{+0.02}_{-0.01}$	$1.16^{+0.03}_{-0.02}$	$1.31^{+0.03}_{-0.03}$	$1.51^{+0.03}_{-0.03}$	$1.76^{+0.05}_{-0.05}$	$2.15^{+0.06}_{-0.06}$	$2.7^{+0.07}_{-0.07}$	$3.8^{+0.08}_{-0.07}$	$6.03^{+0.11}_{-0.12}$	$11.1^{+0.35}_{-0.39}$		
$R_s=3.68^{+0.27}_{-1.43}\times10^2$	M (10^{14} $M_\odot$)	-	$1.17^{+0.24}_{-0.2}$	$1.27^{+0.26}_{-0.21}$	$1.4^{+0.29}_{-0.21}$	$1.59^{+0.32}_{-0.2}$	$1.83^{+0.37}_{-0.2}$	$2.16^{+0.44}_{-0.18}$	$2.66^{+0.54}_{-0.16}$	$3.48^{+0.71}_{-0.16}$	$5.1^{+1.04}_{-0.43}$	$7.72^{+1.57}_{-1.1}$		
Perseus	r (kpc)	35.4	44.3	55.3	69.2	86.5	108	135	169	211	264	330		
$\rho_o=7.42^{+0.25}_{-0.23}\times10^5$	M_g (10^{12} $M_\odot$)	$0.205^{+0.0006}_{-0.0006}$	$0.37^{+0.001}_{-0.001}$	$0.641^{+0.002}_{-0.002}$	$0.994^{+0.002}_{-0.002}$	$1.51^{+0.003}_{-0.003}$	$2.21^{+0.004}_{-0.004}$	$3.19^{+0.005}_{-0.005}$	$4.43^{+0.008}_{-0.008}$	$6.31^{+0.01}_{-0.01}$	$8.75^{+0.02}_{-0.02}$	$14.4^{+0.03}_{-0.03}$		
$R_s=5.84^{+0.26}_{-0.24}\times10^2$	M (10^{13} $M_\odot$)	-	$0.496^{+0.03}_{-0.02}$	$0.756^{+0.04}_{-0.04}$	$1.15^{+0.06}_{-0.05}$	$1.73^{+0.08}_{-0.08}$	$2.59^{+0.12}_{-0.12}$	$3.85^{+0.18}_{-0.17}$	$5.65^{+0.25}_{-0.24}$	$8.19^{+0.36}_{-0.34}$	$11.7^{+0.49}_{-0.46}$	$16.5^{+0.66}_{-0.62}$		
PKS0745	r (kpc)	46.5	53.4	61.6	71.5	83.4	97.7	116	140	177	224	303	495	1120
$\rho_o=1.65^{+0.13}_{-0.11}\times10^6$	M_g (10^{12} $M_\odot$)	$0.661^{+0.006}_{-0.006}$	$0.865^{+0.01}_{-0.01}$	$1.15^{+0.02}_{-0.02}$	$1.53^{+0.02}_{-0.02}$	$2.05^{+0.03}_{-0.03}$	$2.74^{+0.03}_{-0.03}$	$3.76^{+0.04}_{-0.04}$	$5.26^{+0.05}_{-0.05}$	$7.62^{+0.07}_{-0.07}$	$11.3^{+0.09}_{-0.09}$	$18.9^{+0.12}_{-0.12}$	$35.7^{+0.24}_{-0.24}$	$101.0^{+1.51}_{-1.5}$
$R_s=3.51^{+0.5}_{-0.42}\times10^2$	M (10^{13} $M_\odot$)	-	$0.869^{+0.11}_{-0.11}$	$1.13^{+0.14}_{-0.14}$	$1.47^{+0.19}_{-0.18}$	$1.93^{+0.24}_{-0.23}$	$2.53^{+0.3}_{-0.29}$	$3.39^{+0.39}_{-0.37}$	$4.61^{+0.51}_{-0.47}$	$6.62^{+0.7}_{-0.63}$	$9.43^{+0.94}_{-0.82}$	$14.5^{+1.33}_{-1.13}$	$26.8^{+2.18}_{-1.81}$	$60.8^{+4.81}_{-4.14}$
RBS797	r (kpc)	49.0	60.3	76.1	98.1	131	194	333	980	1720				
$\rho_o=1.69^{+0.48}_{-0.25}\times10^6$	M_g (10^{13} $M_\odot$)	$0.101^{+0.003}_{-0.003}$	$0.148^{+0.007}_{-0.007}$	$0.232^{+0.01}_{-0.01}$	$0.356^{+0.01}_{-0.01}$	$0.592^{+0.02}_{-0.02}$	$1.06^{+0.03}_{-0.03}$	$2.34^{+0.07}_{-0.06}$	$8.72^{+0.34}_{-0.33}$	$16.5^{+1.87}_{-2.01}$				
$R_s=4.21^{+2.26}_{-1.15}\times10^2$	M (10^{14} $M_\odot$)	-	$0.138^{+0.06}_{-0.04}$	$0.21^{+0.09}_{-0.07}$	$0.329^{+0.13}_{-0.1}$	$0.542^{+0.21}_{-0.14}$	$1.02^{+0.38}_{-0.23}$	$2.27^{+0.76}_{-0.41}$	$8.09^{+2.31}_{-1.19}$	$13.2^{+3.86}_{-2.19}$				
Zw2701	r (kpc)	51.5	59.6	70.1	83.7	101	124	157	202	274	419	1100		
$\rho_o=2.35^{+0.29}_{-0.17}\times10^6$	M_g (10^{12} $M_\odot$)	$0.37^{+0.02}_{-0.02}$	$0.526^{+0.04}_{-0.04}$	$0.747^{+0.05}_{-0.05}$	$1.07^{+0.05}_{-0.06}$	$1.55^{+0.07}_{-0.08}$	$2.2^{+0.1}_{-0.11}$	$3.33^{+0.13}_{-0.13}$	$5.09^{+0.17}_{-0.17}$	$8.23^{+0.24}_{-0.24}$	$16.4^{+0.3}_{-0.3}$	$55.1^{+1.77}_{-1.78}$		
$R_s=2.48^{+0.79}_{-0.49}\times10^2$	M (10^{13} $M_\odot$)	-	$0.98^{+0.22}_{-0.18}$	$1.3^{+0.29}_{-0.23}$	$1.75^{+0.37}_{-0.29}$	$2.39^{+0.49}_{-0.36}$	$3.29^{+0.64}_{-0.45}$	$4.65^{+0.84}_{-0.57}$	$6.66^{+1.11}_{-0.7}$	$9.96^{+1.48}_{-0.86}$	$16.4^{+2.13}_{-1.19}$	$39.7^{+5.41}_{-3.69}$		
Zw3146	r (kpc)	10.7	27.2	45.4	63.6	85.4	118	170	259	553	2580			
$\rho_o=5.79^{+1.79}_{-1.12}\times10^5$	M_g (10^{12} $M_\odot$)	$0.032^{+0.006}_{-0.006}$	$0.222^{+0.02}_{-0.02}$	$0.598^{+0.04}_{-0.04}$	$1.29^{+0.08}_{-0.05}$	$2.42^{+0.1}_{-0.08}$	$4.53^{+0.14}_{-0.14}$	$8.43^{+0.23}_{-0.24}$	$17.2^{+0.33}_{-0.35}$	$49.5^{+1.07}_{-0.98}$	$285.0^{+9.36}_{-12.26}$			
$R_s=7.38^{+3.07}_{-1.92}\times10^2$	M (10^{13} $M_\odot$)	-	$0.192^{+0.08}_{-0.07}$	$0.517^{+0.21}_{-0.19}$	$0.983^{+0.4}_{-0.35}$	$1.71^{+0.69}_{-0.59}$	$3.1^{+1.24}_{-1.03}$	$5.97^{+2.32}_{-1.83}$	$12.2^{+4.56}_{-3.37}$	$38.7^{+13.27}_{-8.62}$	$215.0^{+66.78}_{-43.64}$			

Appendix B

Studying AGN Feedback in the Virgo Cluster with Astro-H

The work in this chapter was performed as a co-author to the Astro-H White Paper titled "AGN Feedback in the Virgo Cluster".

As the closest galaxy cluster to us, and as one of the brightest extra-galactic X-ray sources in the sky, the Virgo Cluster is one of the best targets for studying AGN feedback. M87, the central dominant galaxy in the Virgo Cluster has been observed with high spatial resolution in the X-ray band, revealing many interactions of the intracluster medium with the AGN. These include cavities in the ICM, a shock front driven by the AGN, and metal enriched central cluster gas dragged into the hot atmosphere (Forman et al., 2005; Simionescu et al., 2008; Million et al., 2010; Werner et al., 2010). High resolution spectra for M87 would enable measurements of the dynamics of these interactions, and measure the metal abundance of the uplifted central gas independently of the ambient cluster atmosphere. This makes the Soft X-ray Spectrometer (SXS) on board the upcoming Astro-H telescope ideal for observing M87, as it will have very high spectral resolution of $\Delta E \sim 5eV$ (Takahashi et al., 2012). This will allow us to observe many individual spectral lines in the ICM which are unresolved with current instruments. This will enable the first accurate determination of velocity structure in the ICM, as well as accurate abundance measurements of trace elements, which will help to constrain transport properties in the ICM, as well as probe the star formation history in centres of clusters.

M87 is one of the proposed targets to have guaranteed time for observations in the early science phase of Astro-H. We have been collaborating on the white paper which details the science goals, observing strategy, and the expected constraints on measurements made

with the new observations. Two of the proposed pointings include the eastern and south-western X-ray arms of cold metal-enriched gas that have been uplifted by the AGN. The primary goals of these pointings will be to measure the turbulence of the ICM imparted by a shock front at 3', measure the line of sight velocity of the cold gas being uplifted, and to measure the abundances of the uplifted gas independently of the ambient gas. The pointing strategy, location of the shock front, and the uplifted X-ray arms are illustrated in figure 1.

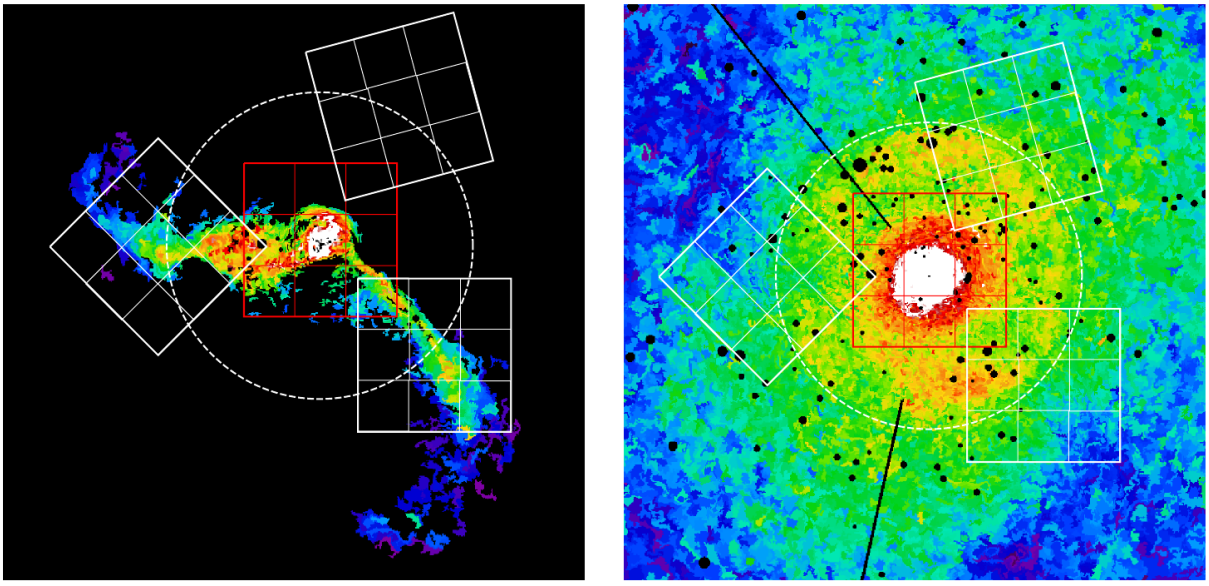

Figure B.1: *Left:* Normalization of the 1keV gas derived from a multi-temperature fit of Chandra spectra from Werner et al. (2010). *Right:* Pressure map derived from Chandra spectra from Million et al. (2010). The circle indicates the 3' spherical shock front, and the large boxes represent the 3×3 arcmin SXS field of view of the proposed observations. The small boxes are 1×1 arcmin spaxels, and could be used to measure the turbulent velocity before and after the shock front. In this figure, north is up and east is left. This figure was produced by A. Simionescu, and was used in the White Paper.

To assess how well the quantities of interest can be calculated as well as the optimal exposure times for observations, SXS spectra were simulated for the proposed E and SW arm pointings. These simulations were first performed by the Stanford group, and we performed them as a consistency check of their early results. First, Chandra spectra were extracted from the SXS 3' by 3' field of view of the proposed pointings, and of the 1' by 1' region at the centre of the SW pointing. These spectra were fit in the 0.5-7.0 keV range with

an absorbed two-temperature model in SPEX, with the metallicity of the lower temperature gas tied to twice that of the warm ambient gas, motivated by previous observations. The best fit parameters of this model were used as the spectral model to simulate the Astro-H spectra, with an added turbulent velocity component of 200km/s for the warm component, and a line of sight velocity of 300km/s for the cold component, which is roughly half of the ambient sound speed. The metallicity was set to 1 solar for the warm component and 2 solar for the cold component, motivated by the results of Simionescu et al. (2008).

Spectra were simulated for a 100ks exposure using the most current 5eV response matrix and the flat sky ancillary response file provided on the Astro-H website. These simulated spectra were fit in the 0.3-10keV range with an absorbed two-temperature model, and the errors of the best fitting parameters were calculated. Turbulent velocity and line of sight velocity were found to have statistical errors of $\sim \pm$ 15km/s, and $\sim \pm$ 20km/s respectively. The abundances of the warm gas were determined to within 10%, and the abundances of the cool gas were determined to within 30% for O, Si, S, and 15% for Fe. Our results were found to be generally consistent with the simulation results of the Stanford group, the largest discrepancy being the precision on the cold Fe abundance measurement, which they found they could determine to $5-7\%$. Additionally, we simulate spectra of the central spaxel of the SW arm for 50, 100, and 200ks. The results of our spectral simulations are shown in table B.1, and an example of a Chandra spectrum and a simulated SXS spectrum are shown in figure B.2.

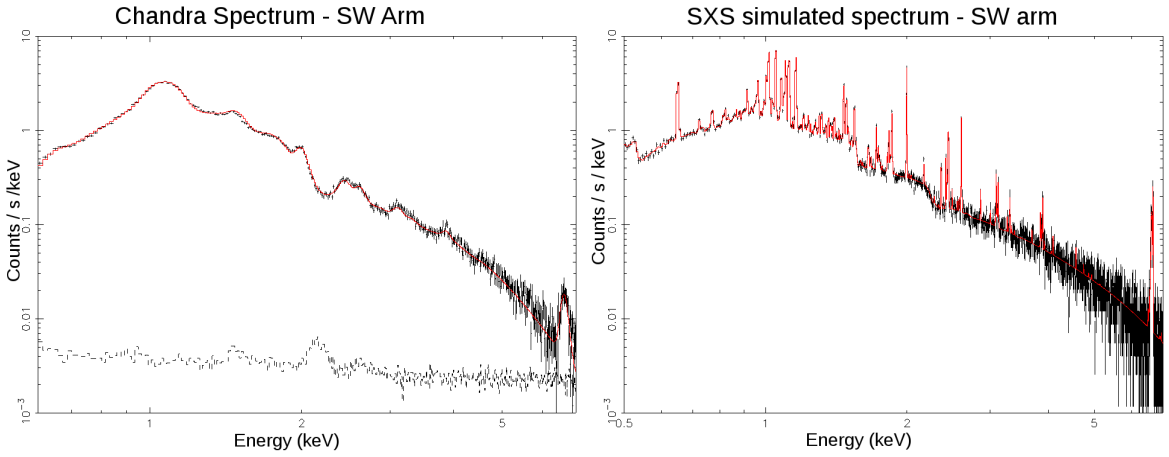

Figure B.2: *Left:* Chandra spectrum of SW arm with best fitting 2-temperature model. *Right:* Simulated SXS spectrum of SW arm with best fitting 2-temperature model

Table B.1: Best fit parameters of SXS simulated spectra

Parameter	E	SW	Spaxel 50ks	Spaxel 100ks	Spaxel 200ks
T cold (keV)	$1.14^{+0.01}_{-0.01}$	$1.06^{+0.01}_{-0.01}$	$0.98^{+0.02}_{-0.02}$	$0.93^{+0.01}_{-0.01}$	$0.95^{+0.01}_{-0.01}$
Norm cold (10^{64}cm^{-3})	$0.33^{+0.05}_{-0.05}$	$0.21^{+0.05}_{-0.04}$	$0.06^{+0.02}_{-0.02}$	$0.04^{+0.01}_{-0.01}$	$0.05^{+0.01}_{-0.01}$
T hot (keV)	$2.15^{+0.02}_{-0.02}$	$2.19^{+0.01}_{-0.01}$	$2.04^{+0.04}_{-0.04}$	$2.02^{+0.02}_{-0.02}$	$2.02^{+0.02}_{-0.02}$
Norm hot (10^{64}cm^{-3})	$4.44^{+0.06}_{-0.06}$	$5.15^{+0.05}_{-0.05}$	$0.65^{+0.02}_{-0.02}$	$0.64^{+0.01}_{-0.01}$	$0.64^{+0.01}_{-0.01}$
v_{los} cool (km/s)	279^{+17}_{-14}	296^{+22}_{-18}	221^{+35}_{-35}	294^{+27}_{-24}	293^{+17}_{-15}
v_{turb} hot (km/s)	206^{+16}_{-17}	188^{+14}_{-14}	248^{+43}_{-44}	135^{+33}_{-35}	168^{+22}_{-23}
O cool	$1.13^{+0.26}_{-0.22}$	-	-	-	$1.22^{+0.29}_{-0.24}$
Si cool	$2.04^{+0.42}_{-0.33}$	$2.29^{+0.66}_{-0.48}$	-	$2.48^{+0.82}_{-0.56}$	$1.07^{+0.31}_{-0.25}$
S cool	$2.30^{+0.62}_{-0.51}$	-	-	-	-
Fe cool	$2.01^{+0.35}_{-0.26}$	$2.12^{+0.55}_{-0.37}$	$1.50^{+0.59}_{-0.33}$	$1.77^{+0.51}_{-0.33}$	$1.81^{+0.32}_{-0.24}$
Ne hot	$0.76^{+0.04}_{-0.04}$	$0.81^{+0.04}_{-0.04}$	$0.72^{+0.12}_{-0.11}$	$0.87^{+0.08}_{-0.08}$	$0.81^{+0.05}_{-0.05}$
Mg hot	$0.58^{+0.04}_{-0.04}$	$0.61^{+0.03}_{-0.03}$	$0.50^{+0.10}_{-0.09}$	$0.60^{+0.06}_{-0.06}$	$0.60^{+0.05}_{-0.05}$
Si hot	$1.00^{+0.04}_{-0.04}$	$1.00^{+0.04}_{-0.03}$	$0.95^{+0.10}_{-0.09}$	$0.91^{+0.06}_{-0.06}$	$1.08^{+0.05}_{-0.05}$
S hot	$1.00^{+0.05}_{-0.05}$	$1.05^{+0.04}_{-0.04}$	$1.09^{+0.13}_{-0.12}$	$1.07^{+0.08}_{-0.08}$	$0.96^{+0.06}_{-0.06}$
Ar hot	$1.14^{+0.11}_{-0.11}$	$1.22^{+0.10}_{-0.10}$	-	$0.93^{+0.20}_{-0.19}$	$1.14^{+0.15}_{-0.14}$
Ca hot	$0.76^{+0.11}_{-0.11}$	$0.97^{+0.11}_{-0.10}$	-	$1.22^{+0.22}_{-0.21}$	$0.98^{+0.16}_{-0.15}$
Fe hot	$1.02^{+0.02}_{-0.02}$	$1.02^{+0.02}_{-0.02}$	$0.94^{+0.06}_{-0.05}$	$1.02^{+0.04}_{-0.04}$	$0.98^{+0.03}_{-0.03}$
Ni hot	$1.20^{+0.08}_{-0.08}$	$1.03^{+0.08}_{-0.07}$	$1.19^{+0.21}_{-0.20}$	$1.03^{+0.14}_{-0.13}$	$1.15^{+0.10}_{-0.10}$

Following the requirements of the white paper, parameters determined at less than 4σ are not included. O_{hot} is fixed to $0.6Fe_{hot}$, the measured ratio of the ambient component. E and SW arms are simulated with 100ks.

The expected point spread function (PSF) of 1.3' is a significant fraction of the size of the detector field of view (FOV) of 3' by 3'. This means that there may be significant amounts of counts scattered out if the FOV, as well as contamination from regions outside the FOV. The atmosphere in M87 is well stratified and isothermal at each radius (Simionescu et al., 2008), so the amount of radial scattering is the primary concern. To investigate this effect, images of concentric annuli of M87 were convolved with the current PSF model, and the contribution from each region in each FOV was calculated. The annuli were centered on the cluster center, and had radial ranges of 0'-1.5' (core region), 1.5'-4.5' (field of view region), and 4.5'-10'(everything beyond the field of view). We found that 18% of counts were scattered radially out of the FOV region, and $\approx$ 20% of the counts in the FOV region were from the other regions, with 13% coming from the bright core. Additionally, the 1' by 1' spaxels will lose 42% of their counts radially. These effects will be important in determining desired exposure times of observations, and will be important to include in more detailed spectral simulations in the lead up to launch.

Appendix C

Co-authored Publications

C.1 Bondi Accretion

My contribution as a co-author on Russell et al. (2013) was to use Chandra X-ray data to determine cavity dimensions for the 13 systems of the Bondi subsample in section 3.7. Cavity powers were estimated for these systems using deprojected density and temperatue profiles calculated by Helen Russell. These values were used to re-examine the relation between jet power and Bondi accretion rate.

C.2 ALMA analysis of Abell 1664 and Abell 1835

I am a co-author on the papers Russell et al. (2014) and McNamara et al. (2014), cycle-0 ALMA analyses of Abell 1664 and Abell 1835 respectively. I assisted in early analysis of the data, including making velocity maps of the CO emission, and comparing the spatial extent of the CO emission to HST and Chandra images. I provided hydrostatic mass profiles for both systems that were used in the analysis.

C.3 Chandra analysis of MS0735.6+7421

The mass profile for MS0735.6+7421 shown in appendix A is used in the analysis of Vantyghem et al. (2014). The mass profile is used to calculate the buoyancy timescale of

massive outer cavities, as well as to calculate the total energy per particle injected from the AGN. I also contributed scripts to correct spectra for the area lost to removed point sources, chip gaps and dead pixels.